

CRANFIELD UNIVERSITY

TONG CHEN

HYPERSPECTRAL IMAGING FOR THE REMOTE SENSING OF  
BLOOD OXYGENATION AND EMOTIONS

CRANFIELD DEFENCE AND SECURITY  
PhD by Research

PhD  
Academic Year: 2008 - 2012

Supervisor: Peter Yuen  
May 2012



CRANFIELD UNIVERSITY

CRANFIELD DEFENCE AND SECURITY  
PhD by Research

PhD

Academic Year 2008 - 2012

TONG CHEN

HYPERSPECTRAL IMAGING FOR THE REMOTE SENSING OF  
BLOOD OXYGENATION AND EMOTIONS

Supervisor: Peter Yuen  
May 2012

This thesis is submitted in partial fulfilment of the requirements for  
the degree of Doctor of Philosophy

© Cranfield University 2012. All rights reserved. No part of this  
publication may be reproduced without the written permission of the  
copyright owner.



## ABSTRACT

This PhD project is a basic research and it concerns with how human's physiological features, such as tissue oxygen saturation (StO<sub>2</sub>), can be captured from a stand-off distance and then to understand how this remotely acquired physiological feature can be deployed for biomedical and other applications.

This work utilises Hyperspectral Imaging (HSI) within the diffuse optical scattering framework, to assess the StO<sub>2</sub> in a contactless remote sensing manner. The assessment involves a detailed investigation about the wavelength dependence of diffuse optical scattering from the skin as well as body tissues, under various forms of optical absorption models. It is concluded that the three-chromophore extended Beer Lambert Law model is better suited for assessing the palm and facial tissue oxygenations, especially when spectral data in the wavelengths region of [516-580]nm is used for the analysis.

A first attempt of using the facial StO<sub>2</sub> to detect and to classify people's emotional state is initiated in this project. The objective of this work is to understand how strong emotions, such as distress that caused by mental or physical stimulations, can be detected using physiological feature such as StO<sub>2</sub>. Based on data collected from ~20 participants, it is found that the forehead StO<sub>2</sub> is elevated upon the onset of strong emotions that triggered by mental stimulation. The StO<sub>2</sub> pattern in the facial region upon strong emotions that are initiated by physical stimulations is quite complicated, and further work is needed for a better understanding of the interplays between bodily physique, individual's health condition and blood transfusion control mechanism. Most of this work has already been published and future research to follow up when the author returns back to China is highlighted.

Keywords:

Tissue oxygen saturation, wavelength selection, hyperspectral imaging, emotion detection, anxiety detection, affective computing



## **ACKNOWLEDGEMENTS**

I would like to thank my supervisor Dr Peter Yuen at Cranfield University, for initialling this exciting project and leading me into the hyperspectral imaging research area. His strictness and criticise have always worked as one of sources of motivation. I sincerely appreciate his invaluable guidance and advice. Dr Peter Yuen's enthusiasm towards the work and research has influenced me for the last three and half years and would definitely continuously influence my future career.

I would like to thank my wife Min Zhou and my son Luming Chen for their unconditional trust and love. Without their support, all these cannot even start. It is their patience, understanding, and encouragement that make me have the courage and determination to complete this long journey. I would like to thank my mother-in-law and my mother for their help to my family when I was not at home. They have dedicated a lot to their children and subsequently grandchildren.

I would like to thank Dr Feng Wang, Dr Weizhong Fei, and Mr Xiaodong Li for their discussion and suggestions. It is them who make the life in Cranfield much easier. I believe this friendship will continue after I finish the study.

Finally, I would like to thank UK MOD and Department of Informatics and System Engineering at Cranfield University for providing studentship.





# TABLE OF CONTENTS

ABSTRACT .....	i
ACKNOWLEDGEMENTS.....	iii
LIST OF FIGURES.....	ix
LIST OF TABLES .....	xvii
LIST OF ABBREVIATIONS.....	xxi
1 INTRODUCTION.....	1
1.1 Background.....	1
1.2 Aim of Research .....	1
1.3 Motive of Research .....	2
1.4 Contribution and Achievements .....	3
1.5 Thesis Layout .....	3
2 HYPERSPSPECTRAL IMAGING (HSI) .....	5
2.1 Introduction .....	5
2.2 Fundamental of HSI .....	5
2.3 HSI Instrumentation: An Overview .....	8
2.4 Spectrograph .....	8
2.5 HSI System @Cranfield .....	9
2.5.1 Mirror Scanning Systems Design .....	9
2.5.2 VNIR System Employed in the Project .....	13
3 TISSUE OPTICS AND TISSUE OXYGEN SATURATION .....	17
3.1 Introduction .....	17
3.2 Optical Properties .....	17
3.2.1 Refractive Index .....	17
3.2.2 Absorption .....	18
3.2.3 Scattering .....	20
3.3 Skin Tissue Optics .....	21
3.3.1 Structure of Skin and Its Chromophores .....	21
3.3.2 Absorption Properties of Skin Chromophores .....	23
3.3.3 Calibration of Spectrometer.....	24
3.4 Background of Tissue Oxygen Supplies .....	25
3.5 Tissue Blood Flow and Oxygen Content.....	27
3.6 Tissue Oxygen Saturation.....	29
3.7 Electro-optical Assessment Methods for Tissue Oxygen Saturation.....	30
3.7.1 Conventional Oxygen Saturation Assessments: Oximetry .....	30
3.7.2 Hyperspectral Imaging Method for Oxygen Assessment.....	32
3.7.3 Thermal Imaging .....	35
4 MODEL AND WAVELENGTH SELECTION FOR HYPERSPSPECTRAL IMAGING TISSUE OXYGEN SATURATION.....	39
4.1 Motive of Research .....	39
4.2 Overview of Algorithms for StO2 Assessment .....	40

4.2.1 Beer Lambert Law: Revisited .....	40
4.2.2 Modified Beer Lambert Law [56][57].....	41
4.3 Methodology for the StO <sub>2</sub> Assessment in This Research.....	42
4.3.1 Tissue Absorbance .....	42
4.3.2 StO <sub>2</sub> Assessment and Error Estimation.....	43
4.4 Experimental Conditions .....	45
4.5 Wavelength and Model Selection for StO <sub>2</sub> Assessment.....	47
4.5.1 Whole Spectra or Subset Spectra: Regression Plane.....	47
4.5.2 Wavelength Selection: Subset Spectra .....	51
4.5.3 Visible VS Near Infra-red Spectral Region .....	55
4.5.4 BL Model VS EBL Model: Reproducibility and Model Error.....	56
4.6 Conclusion .....	68
5 IMPROVE TISSUE OXYGEN SATURATION ASSESSMENT BY USING BODY REFLECTANCE .....	71
5.1 Motive of Research .....	71
5.2 Specular Reflectance and Body Reflectance [66].....	71
5.3 Specular Reflection Measurement of Human Skin .....	73
5.3.1 Polarisation and Reflection.....	73
5.3.2 Experiment Settings .....	73
5.3.3 Measuring The Specular Reflectance of Skin .....	75
5.4 StO <sub>2</sub> Measurement Using Body Reflectance.....	76
5.5 Conclusion .....	83
6 COMPARISON OF HYPERSPECTRAL IMAGING AND THERMAL IMAGING FOR ASSESSING TISSUE OXYGEN SATURATION.....	85
6.1 Introduction .....	85
6.2 Instrumentations and HSI StO <sub>2</sub> Assessment Algorithm.....	85
6.3 Consistency of HSI StO <sub>2</sub> and TI Temperature.....	86
6.4 Ambient Temperature Effect .....	88
6.5 Perspiration Effect.....	91
6.6 Conclusion .....	93
7 SURVEY OF ANXIETY DETECTION.....	95
7.1 Introduction .....	95
7.2 Hormones Detection .....	95
7.3 Direct Brain Activity Probe: Functional Magnetic Resonance Imaging (fMRI).....	99
7.4 Facial Expression.....	100
7.5 Physiological Signal Based Anxiety Detection Techniques.....	101
7.6 Thermal Imaging .....	102
7.7 Emotion and Tissue Oxygen Saturation.....	107
7.7.1 Emotion and Stressor.....	107
7.7.2 Signature of Stressor-induced Emotion: Arousal of Tissue Oxygenation .....	107

8 EMOTION DETECTION BASED ON TISSUE OXYGEN SATURATION ....	113
8.1 Introduction .....	113
8.2 MSE and PSE .....	113
8.3 Experimental Procedures and Protocols.....	114
8.4 Facial StO2 and Emotion .....	115
8.5 Conclusion .....	120
9 CONCLUSION AND FUTURE WORK .....	123
REFERENCES .....	125
APPENDICES .....	141
Appendix A VNIR_3.0@Cranfield .....	141
Appendix B List of Publications.....	149



## LIST OF FIGURES

Figure 2-1 (a) illustration of a HSI image which contains hundred to thousand of narrow wavebands forming a 3D image cube. (b) Shows the spectral response in reflectance of the palm tissue for all wavebands within 400-900nm range. This optical signature is unique specific to the chemical composition of the object (palm tissue in this case). (c) shows the 2D image in three different wavebands of the same object (palm).....	7
Figure 2-2 typical hyperspectral imaging system consists of an object lens, a spectrograph and a 2D CCD camera .....	8
Figure 2-3 (a) push-broom hyperspectral imaging system by moving the camera along the scene to built up an image cube. (b) Mirror scanner version of the HSI that has been employed in this work for building up image cube [21]. .	9
Figure 2-4 (a) outlines the positioning of the step motor within the mirror scanning system. (b) A schematic view of the T shape motor mount and the reference line defined by the entrance slit of the spectrograph and the rotating axis of the step motor. (c) A schematic view of the motor housing (black) and the motor (green).....	11
Figure 2-5 (a) the entrance slit of the spectrograph is highlighted by the edge of the ruler, and a beam of laser is firstly aligned with the slit to define the line of reference. (b) The laser beam is then switched by 90 degree to define the vertical axis of the optical path. ....	12
Figure 2-6 (a) shows the alignment of the laser beam with the motor rotating axis. (b): shows the optimum alignment when the laser beam passes through the cavity of the dummy motor without hitting the Perspex, otherwise the whole Perspex glows when the laser hits the wall of the cavity. ....	12
Figure 2-7 the normalised emission intensity of mercury lamp measured by the VNIR spectrograph (blue) and compares it with the calibrated spectrometers. ....	13
Figure 2-8 the VNIR Hyperspectral imaging system utilised in this study: (a) Picture of the HSI system which is designed and built [21] during the course of this work (b) schematic drawing of the mirror scanner assembly and the Headwall dispersive spectrograph.....	14
Figure 2-9 the operational blocks of the HSI system, image acquisition and processing that has been utilised throughout this work. ....	15
Figure 3-1 refraction of light between two media with refractive indices of $n_1$ and $n_2$ ( $n_1 < n_2$ ).....	18
Figure 3-2 attenuation of light through a non-scattering medium of thickness $l$	19
Figure 3-3 attenuation of light transmitting through non-absorption medium....	20

Figure 3-4 illustration of forward scattering event when the photon is deflected by an angle $\theta$ .....	21
Figure 3-5 a cross-section illustration of human skin and tissue structure[25].	22
Figure 3-6 molar extinction coefficients of melanin, oxy-haemoglobin (HbO <sub>2</sub> ), and deoxy-haemoglobin (Hb) [26] chromophore in human tissue. ....	23
Figure 3-7 extinction coefficients of HbO <sub>2</sub> and Hb (left) [26], and reflectance of fingers with high HbO <sub>2</sub> and Hb (right). ....	25
Figure 3-8 oxygen-haemoglobin Dissociation Curve [27]. The higher is the partial pressure of oxygen, the higher the haemoglobin oxygen saturation. The temperature, concentration of CO <sub>2</sub> , DPG, and lactic acid are inversely affecting the oxygenation saturation.....	26
Figure 3-9 arteriole, capillary bed, and venule [28]. Capillary bed connects arteriole and venule which supply oxygen to the tissue. ....	27
Figure 3-10 a simplified model of oximeter: Transmitted intensity $I$ is measured for an incident intensity $I_{in}$ using Beer-Lambert law.....	31
Figure 3-11 (a): schematic block diagram of Zuzak's HSI for assessing the oxy-haemoglobin concentration of tissue. (b): shows the absorbance of 100% pure oxy-haemoglobin and deoxy-haemoglobin used by Zuzak as reference data [6].....	33
Figure 3-12 shows the early work performed by Zuzak [6] presenting the HbO <sub>2</sub> in grey scale image of the palm: Rows 1 and 2 after the subject inhaled ambient air and NO respectively. a, Baseline condition; b, L-NMMA infused for 1.5 minutes; c, after 3.0 minutes of L-NMMA; and d, after 4.5 minutes of L-NMMA. Note that the StO <sub>2</sub> is seen to reduce (darker in grey scale) across a-d columns when the blood flow rate is reduced further by the L-NMMA. ....	34
Figure 3-13 the StO <sub>2</sub> of pig's skin presented in grey scale [41]. The brighter the colour, the higher the StO <sub>2</sub> . The baseline of the skin StO <sub>2</sub> is in first and third column, and the StO <sub>2</sub> after bleeding is in the second and fourth column. It is seen that the pig's skin baseline StO <sub>2</sub> are higher than that after the pig bleed. ....	35
Figure 3-14 (a) skin temperature of a human face. (b) the blood flow rate map deduced by the blood transfusion model [16].....	36
Figure 4-1 depicts the two experimental conditions of (a) Illumination from the top of the palm and (b) Illumination sources is directed from the front towards the palm (not shown). Standard reflectors such as the white and black spectralons are situated at the back of the scene.....	46
Figure 4-2 shows different views of the 3D scatter plot ( $A$ , $\epsilon HbO_2$ , $\epsilon Hb$ ) over the spectral regions of 450nm to 850nm range, where $A$ is the apparent absorbance of the ROIs of the palm (inset) without taking into account the	

tissue scattering and melanin absorption. The view angles for the left column are azimuth= $-95.5^\circ$ , elevation= $16^\circ$ , and right column are azimuth= $156.5^\circ$ , elevation= $22^\circ$ . Note that the data points are seen to form at least 3 different planes (not drawn in the figure) oriented at three different angles to each other. .... 48

Figure 4-3 shows the effect of using the EBL3C formulation (Equation 4-7) for the StO<sub>2</sub> analysis: (a) 3D scatter plot of the tissue absorbance  $A$  after removing the melanin and specular reflection terms, (b) the solution plane (in colour) for the EBL3C (c) the Euclidean distance of all data points to the solution plane, (d) the StO<sub>2</sub> of the palm and ischemia finger using the *Ceff* as deduced by EBL3C formulation. The model error of the ROI is very large approaching to  $\sim 22\%$ . .... 50

Figure 4-4 shows the StO<sub>2</sub> map of the ischemia finger and palm under illumination from the top. Subsets of spectral regions have been used as inputs under the EBL model (Equation 4-7): (a) 450-470nm, (b) 470-514nm, (c) 516-580nm, (d) 582-700nm, (e) 730-830nm & (f) the whole spectral range of 450-850nm for comparison. It is noted that the model error for assessing the StO<sub>2</sub> of the ROI is the largest in (f). .... 52

Figure 4-5 light penetration depth of normal human skin (Caucasian) [63]. .... 53

Figure 4-6 shows the StO<sub>2</sub> maps of the ischemia finger and palm of the same subject but under different illuminations conditions of: from the top (top panel) and from the front (bottom panel). Two subsets of spectral regions in the visible (left hand column) and near infra red (right hand column) data have been used as inputs for the StO<sub>2</sub> assessment under the EBL3C model (Equation 4-7). The StO<sub>2</sub> values are presented in false colour images. .... 55

Figure 4-7 shows StO<sub>2</sub> map produced by BL2C under top (left column) and front (right column) illumination using the subset spectral ranges of [450:470], [472:514], [516:580] as input data. .... 58

Figure 4-8 shows StO<sub>2</sub> map produced by BL2C under top (left column) and front (right column) illumination using the subset spectral ranges of [582:700], [730:830], [450:850] as input data. .... 59

Figure 4-9 shows StO<sub>2</sub> map produced by BL3C under top (left column) and front (right column) illumination using the subset spectral ranges of [450:470], [472:514], [516:580] as input data. .... 60

Figure 4-10 shows StO<sub>2</sub> map produced by BL3C under top (left column) and front (right column) illumination using the subset spectral ranges of [582:700], [730:830], [450:850] as input data. .... 61

Figure 4-11 shows StO<sub>2</sub> map produced by EBL2C under top (left column) and front (right column) illumination using the subset spectral ranges of [450:470], [472:514], [516:580] as input data. .... 62

Figure 4-12 shows StO2 map produced by EBL2C under top (left column) and front (right column) illumination using the subset spectral ranges of [582:700], [730:830], [450:850] as input data.....	63
Figure 4-13 shows StO2 map produced by EBL3C under top (left column) and front (right column) illumination using the subset spectral ranges of [450:470], [472:514], [516:580] as input data.....	64
Figure 4-14 shows StO2 map produced by EBL3C under top (left column) and front (right column) illumination using the subset spectral ranges of [582:700], [730:830], [450:850] as input data.....	65
Figure 4-15 shows the finger ROIs (black square) for assessing the model errors of StO2 accuracies as presented in Table 5. ....	67
Figure 5-1 shows the interface (specular) reflection, body reflection of skin. Incident light is partly reflected as interface reflection, partly absorbed by tissue chromophores, and partly reflected as body reflection.....	72
Figure 5-2 shows the polarisation experiment for measuring the specular reflection due to skin surface: (a) Polariser A (PLA) is put in front of halogen lamp for generating a polarised light source; (b) Polariser B (PLB) is placed in front of PLA with polarisation parallel to that of PLA; (c) PLB is crossed polarise with PLA; (d) Front view of PLB crossed polarise with PLA; (e) Side view of (d). ....	74
Figure 5-3 shows fRGB images of a palm. (a) With polariser in front of the palm. (b) Without polariser in front of the palm. The black square depicts the location of the ROI. ....	75
Figure 5-4 shows Interface (specular) reflectance of skin in wavelength range of [450-950]nm. ....	76
Figure 5-5 shows the StO2 map obtained from the EBL3C model for a palm under top illumination using $A_{\lambda, \text{body}}$ analysis (Left column) and $A_{\lambda}$ analysis (right column) for the spectral inputs of [450-470]nm, [472-514]nm, [516-580]nm. ....	78
Figure 5-6 shows the StO2 map obtained from the EBL3C model for a palm under top illumination using $A_{\lambda, \text{body}}$ analysis (Left column) and $A_{\lambda}$ analysis (right column) for the spectral inputs of [582-700]nm, [730-830]nm, [450-850]nm. ....	79
Figure 5-7 shows the StO2 map obtained from the EBL3C model for a palm under front illumination using $A_{\lambda, \text{body}}$ analysis (Left column) and $A_{\lambda}$ analysis (right column) for the spectral inputs of [450-470]nm, [472-514]nm, [516-580]nm. ....	80
Figure 5-8 shows the StO2 map obtained from the EBL3C model for a palm under front illumination using $A_{\lambda, \text{body}}$ analysis (Left column) and $A_{\lambda}$ analysis (right column) for the spectral inputs of [582-700]nm, [730-830]nm, [450-850]nm .....	81



- Figure 6-1 shows raw and averaged StO<sub>2</sub> map of a human face. (a) Raw StO<sub>2</sub> map generated with EBL3C using HSI data in [516-580]nm; (b) Averaged StO<sub>2</sub> map generated by averaging (a) with a circular average filter of radius of 1 pixel;(c) 2 pixels; (d) 3 pixels; (e) 4 pixels..... 86
- Figure 6-2 shows TI temperature, and HSI StO<sub>2</sub> maps of a palm with two fingers in ischemia state and hyperfusion state. (a) Temperature map measured by TI of a palm with two fingers in ischemia state; (b) Temperature map measured by TI of the palm with two fingers in hyperfusion state; (c) StO<sub>2</sub> map measured by HSI of the palm with two fingers in ischemia state;(d) StO<sub>2</sub> map measured by HSI of the palm with two fingers in hyperfusion state. Note that the change of the StO<sub>2</sub> and Temperature of two fingers are consistent to each other very well. .... 88
- Figure 6-3 shows TI temperature, TI blood perfusion, and HSI StO<sub>2</sub> maps of the same human face in warm and in cool situation. (a) Face temperature map in indoors environment, the Heart Beat Rate (HBR) of the subject is 90 at the moment the TI data is recorded; (b) Face temperature map immediately after returning from outdoors environment, HBR is 87; (c) Face StO<sub>2</sub> map in indoor environment, HBR is 90; (d) Face StO<sub>2</sub> map immediately after returning from outdoors environment, HBR is 87. Abrupt environment temperature changing has great effect on skin temperature, but little on StO<sub>2</sub> in this experiment setting. .... 90
- Figure 6-4 shows of TI temperature, and HIS StO<sub>2</sub> maps of the face of a healthy subject in baseline and sweating conditions.(a) Baseline face temperature map, HBR is 87; (b) face temperature map in sweat condition, HBR is 110; (c) face temperature map after 8 minutes of (b), HBR is 110; (d) baseline face StO<sub>2</sub> map, HBR is 87; (e) face StO<sub>2</sub> map in sweat condition, HBR is 110; (f) face StO<sub>2</sub> map after 8 minutes if (e), HBR is 110. .... 92
- Figure 6-5 shows RGB image of the subject after excise in warm environment. Sweat is notable around forehead..... 92
- Figure 7-1 (a) ACTH concentration Vs time. (b) Total plasma cortisol concentration Vs time. (c) Salivary free cortisol concentration Vs time. [72] ..... 97
- Figure 7-2 effect size of cortisol increase sorted by types of stressors. The combination of public speaking and cognitive task has the maximum effect size of cortisol increase. [76] ..... 98
- Figure 7-3 effect size of cortisol increase sorted by characteristics of stressors. It is the stressors with uncontrollable and social-evaluative essentials that give the strongest cortisol response. [76] ..... 98
- Figure 7-4 illustration of facial Action Units representing the facial muscular activities that code the facial expression.[85] ..... 100

- Figure 7-5 (a) thermal image of face before startle. (b) Thermal image of face after startle. According to the colour bar, the temperature around periorbital region, pointed by the arrows, increases after startle [91]. ..... 103
- Figure 7-6 thermal images of a male subject. (1) baseline before Stroop stressor (2) during Stroop stressor provocation test (3) baseline before mental arithmetic stressor provocation (4) after the mental arithmetic stress provocation. The bright pixel around forehead area shows higher temperature after the emotional stressor..... 104
- Figure 7-7 the temperature in the selected region MROI is modulated by the air in the out of the nose. The frequency of the changing of the temperature is taken as the respiration rate..... 105
- Figure 7-8 heat patterns (maximum temperature –baseline temperature) change for every AU [106] ..... 106
- Figure 7-9 (a) DEEP is the haemoglobin oxygen saturation of deep venous blood draining from the forearm muscle. IA. ADREN represents the period Intra-arterial infusion of adrenaline 0.1µg/min. The venous haemoglobin oxygen saturation has a transient increase, and then maintains a small increase compared to the baseline throughout the infusion. After 4 minutes of stopping the infusion, the oxygen saturation begins to drop. (b) DEEP is the haemoglobin oxygen saturation of deep venous blood draining from the forearm muscle. IA. ADREN represents the period Intra-arterial infusion of adrenaline 0.2µg/min. The venous haemoglobin oxygen saturation has a transient increase and then decrease to the same even lower level than the baseline. After stopping the infusion, the oxygen saturation goes up and keeps nearly constant for 8 minutes, showing that with the washout of the larger dose infusion, the small dose effect appears (increase the adrenaline) [111]. ..... 109
- Figure 7-10 shows the variations of blood pressure, coronary venous flow, and oxygen extraction ratio and oxygen consumption of a dog under controlled injections of adrenaline (2ug/kg per min at the arrowed point) in an intravenous infusion experiment [112]. It is observed that an increase of blood pressure by almost 2-fold, together with ~90% increase of oxygen content in the blood while the oxygen consumptions by tissues are seen to remain more or less constant after the adrenaline injection, resulting in an abrupt drop of overall oxygen extraction ratio to almost a half causing a net increase of blood oxygenation ~100 - 200% after the adrenaline injections. .... 111
- Figure 7-11 (a) MBF is the blood flow of masseter muscle. AD represents adrenaline infusion. The transient increase of masseter blood flow caused by adrenaline is clear both in 0.1ug/kg and 1ug/kg dose. The larger dose decreases the blood flow lower than baseline after the initial rise. (b) Electrical stimulation of SPLN nerve with 5Hz, 10Hz, and 20Hz, cause uninterrupted rise of masseter blood flow. [113]. ..... 112

Figure 8-1 shows StO2 maps of three participants under baseline, MSE, and PSE. (a)Participant A in baseline; (b) Participant A under MSE; (c) Participant A under PSE; (d)Participant B in baseline; (e) Participant B under MSE; (f) Participant B under PSE; (a)Participant O in baseline; (b) Participant O under MSE (c) Participant O under PSE; ..... 116

Figure 8-2 shows Region of Interests on forehead for generating average StO2 and standard deviation StO2 of forehead..... 117

Figure 8-3 the scatter plot of the rate of change in StO2 Vs the Increasing-Rate-of-HBR for all participants under MSE stimulation which shows no correlation between these two quantities. .... 120



## LIST OF TABLES

Table 1 thickness of epidermis and dermis of different part of human body [24] .....	54
Table 2 model errors of palm ROIs of StO <sub>2</sub> map using various wavelength regions ([450 470]nm, [472 514]nm, [516 580]nm) of data and different BL models under top illumination condition. ....	66
Table 3 model errors of palm ROIs of StO <sub>2</sub> map using various wavelength regions ([582 700]nm, [730 830]nm, [450 850]nm)of data and different BL models under top illumination condition. ....	66
Table 4 model errors of palm ROI1 of StO <sub>2</sub> map using various wavelength regions of data and different BL models under top and front illumination conditions.....	67
Table 5 model errors of finger ROI of StO <sub>2</sub> map using various wavelength regions of data and different BL models under top and front illumination conditions.....	68
Table 6 model Error of palm ROI at various wavelength ranges with BLs method using body reflectance. ....	83
Table 7 model Error of finger ROI at various wavelength ranges with BLs method using body reflectance. ....	83
Table 8 scores of AUs of high and low state anxiety based on FACS.[85] Some scores, such as fear actions, are the score of group of Aus.....	101
Table 9 tabulates the HBR, the averaged (Avg) StO <sub>2</sub> and its standard deviation (Std) of 21 participants' forehead ROI. ....	118
Table 10 gives the percentages rate of change in HBR and forehead StO <sub>2</sub> as the result of MSE and PSE stimulation. Note that the StO <sub>2</sub> due to PSE can either drop or rise with respected to the base line.....	119



**LIST OF EQUATIONS**

Equation 3-1 .....	17
Equation 3-2 .....	17
Equation 3-3 .....	18
Equation 3-4 .....	18
Equation 3-5 .....	19
Equation 3-6 .....	19
Equation 3-7 .....	19
Equation 3-8 .....	20
Equation 3-9 .....	20
Equation 3-10 .....	21
Equation 3-11 .....	21
Equation 3-12 .....	25
Equation 3-13 .....	27
Equation 3-14 .....	27
Equation 3-15 .....	28
Equation 3-16 .....	28
Equation 3-17 .....	29
Equation 3-18 .....	31
Equation 3-19 .....	31
Equation 3-20 .....	31
Equation 3-21 .....	32
Equation 3-22 .....	32
Equation 3-23 .....	32
Equation 3-24 .....	32
Equation 3-25 .....	36
Equation 3-26 .....	37

Equation 3-27 .....	37
Equation 3-28 .....	37
Equation 4-1 .....	40
Equation 4-2 .....	40
Equation 4-3 .....	41
Equation 4-4 .....	41
Equation 4-5 .....	41
Equation 4-6 .....	42
Equation 4-7 .....	42
Equation 4-8 .....	42
Equation 4-9 .....	43
Equation 4-10 .....	43
Equation 4-11 .....	43
Equation 4-12 .....	43
Equation 4-13 .....	43
Equation 4-14 .....	44
Equation 4-15 .....	44
Equation 4-16 .....	44
Equation 4-17 .....	44
Equation 4-18 .....	45
Equation 4-19 .....	45
Equation 5-1 .....	76



## LIST OF ABBREVIATIONS

BL	Beer-Lambert Law
BL2C	Two-chromophore Beer-Lambert Law
BL3C	Three-chromophore Beer-Lambert Law
COTS	Commercial-Off-The-Shell
CO <sub>2</sub>	carbon dioxide
CU	Cranfield University
DPG	Diphosphoglycerate
EA	Emotional Anxiety
EBL	Extended Beer-Lambert Law
EBL2C	Two-chromophore Extended Beer-Lambert Law
EBL3C	Three-chromophore Extended Beer-Lambert Law
ELM	Empirical Line Method
fMRI	Functional Magnetic Resonance Imaging
Hb	Deoxy-Haemoglobin
HbO <sub>2</sub>	Oxy-haemoglobin
HSI	Hyperspectral Imaging
MOD	Ministry of Defence
NIR	Near Infra-Red
PA	Physical Anxiety
PLA	Polariser A
PLB	Polariser B
PO <sub>2</sub>	Partial pressure of Oxygen
ROI	Region of Interest
SDK	Software Development Kit
StO <sub>2</sub>	Tissue Oxygen Saturation
SWIR	Short Wave Infra-Red
TI	Thermal Imaging
VIS	Visible
VNIR	Visible Near Infra-Red
2D	Two-Dimension
3D	Three-Dimension



# **1 INTRODUCTION**

## **1.1 Background**

The tissue oxygen saturation (StO<sub>2</sub>) has been an important physiological feature for the evaluation of blood perfusion in the concerned tissue. The assessment of StO<sub>2</sub> is widely needed in many clinical applications, such as for the detection of central hypovolemia and hypovolemic shocks [1], diagnosing necrotizing fasciitis [2], and also for the detection of breast cancer etc.[3]. The conventional way [4] for measuring StO<sub>2</sub> requires direct contact to the probed tissue. Since the early of 21<sup>st</sup> century, Hyperspectral Imaging (HSI) [5] has been employed in assessing StO<sub>2</sub> through diffusive spectroscopy models [6] in a contactless and remote manner. The study of optical diffuse scattering mechanisms particularly for human body tissue, is still in its infancy stage. For example, a comprehensive understanding of the wavelength dependence scattering mechanism is desperately needed.

## **1.2 Aim of Research**

This PhD project formulates part of the research programme towards the understanding of how human's physiological features can be captured from a stand-off distance. This is a basic research and the ultimate objective of the overall research programme is to understand how these remotely acquired physiological features can be deployed for biomedical and other applications. The project was funded by the UK MOD. Subsequently, any publication related to this work needs the consents from UK MOD.

This PhD project focuses on the remote sensing of a specific physiological feature, namely the tissue oxygen saturation (StO<sub>2</sub>) using spectral sensing technique. The research involves three main parts: (a) instrumentation design and experimental set up, (b) properties of StO<sub>2</sub> acquired by remote sensing technique and (c) how this physiological StO<sub>2</sub> feature can be used for the detection of emotions, such as anxiety, due to emotional or physical stimulations (stressors).

### **1.3 Motive of Research**

The motive behind this research has been driven mainly by the scientific interest of diffuse optical scattering phenomenon from body tissue, as well as its implication for biomedical and other applications. Perhaps it is the latter motive which makes this project strongly supported by both the government and the industry in the past few years.

Diffuse scattering of light by body tissue has been studied for over a century [7], however, almost all previous work has been performed using close proximity of light sources to the body tissue and the sensors are very often enclosed in a light tight enclosure, like that commonly deployed in finger probes. Study of optical diffuse scattering in body tissue at stand-off distance has been in its infancy [8][9][10], and furthermore the understanding of the wavelength dependence scattering phenomenon in body tissue is severely lacking [7]. One motive in this aspect of research is hoping to establish an initial data base of diffusive optical scattering from skin, epidermis and dermis layers, over a range of wavelengths. This kind of research is greatly needed and it is fundamentally important for the understanding of how physiological features, such as StO<sub>2</sub>, can be assessed remotely. This is the first initiative of the research programme and therefore only one skin type (Chinese ethnics) is presented to illustrate the optical scattering phenomena in this thesis. A more comprehensive database involving different skin types will be presented in the forthcoming publications.

The research for the detection of human's emotional states from standoff distances without direct contact with the object, has been one of the greatest demands in biomedical, man-machine interfacing, and affective computing sectors. Conventional methods have largely been using facial expressions [11][12] for the remote sensing of people's emotional state, however, the facial expressions can be suppressed by will, which makes this technique not robust enough. Involuntary physiological responses under the command of the sympathetic nervous system such as body sweat, heart rate, breath rate, body temperature, blood perfusion and oxygenations, have been proposed [13][14] as a tool to monitor the emotional states of people [15][16].

One novelty in this work is the use of tissue oxygen saturation (StO<sub>2</sub>) for the detection, and subsequently classification, of human's emotional state from a stand-off distance using Electro-optical imaging technique for the very first time [13][14]. The basis of the present work is based on the fact that elevated level of adrenaline is secreted into the blood stream when a person is experiencing extreme emotional or physical conditions causing anxiety or excitement, which in turn triggers an elevated heart beat and breathing rate resulting in an increased level of StO<sub>2</sub> in the body. This work serves as the first study in the field, to allow other researchers in the community to continue the approach for a deeper understanding of how physiological features can be used for the classification of human's emotional states.

## **1.4 Contribution and Achievements**

The main contributions of this research have been two folds:

- i) Provision of a detailed investigation about the wavelength dependence of diffuse optical scattering from body tissue under various forms of models for the remote assessment of tissue oxygen saturation (StO<sub>2</sub>).
- ii) The use of StO<sub>2</sub> for the detection and classification of human's emotion for the first time.

## **1.5 Thesis Layout**

The layout of this thesis is arranged in the following manner: the motives and the objectives of the project are highlighted in chapter 1, which is then followed by a description of the experimental set up deployed in this study in chapter 2. The principles and theories of optical diffuse scattering are described in chapter 3. The descriptions of data collected using with and without polarisers to eliminate specular reflection from skins for StO<sub>2</sub> assessments are presented in chapters 4 & 5 respectively. Chapter 6 highlights the advantages and disadvantages of using Hyperspectral imaging and to compare it with the thermal imaging for assessing physiological features such as blood transfusion and StO<sub>2</sub>. Chapter 7 gives a critical review of emotion assessments using

conventional methods, such as facial expressions, as well as nonconventional techniques using various physiological features. Chapter 8 presents an ab-initio investigation of how the emotions of ~20 subjects can be detected and classified using physiological feature of StO<sub>2</sub>, when they are exposed to various emotional and physical stimulations. Chapter 9 concludes the present work, and various critical topics that emerge from this research have been suggested as the future work to be carried out in the South West University when the author is returned to China.

## **2 HYPERSENSPECTRAL IMAGING (HSI)**

### **2.1 Introduction**

Hyperspectral imaging (HSI) is an emerging technique capable to discriminate different species of materials effortlessly, and it has been exclusively employed in this research for the assessment of StO<sub>2</sub> remotely. In this chapter it introduces how the construction and calibration of the HSI system that has been utilised for this PhD research. The HSI system involved Commercial-Off-The-Shelf (COTS) components, such as spectrograph, camera, and a home-made optical scanner system. The development of both the hardware and software of the HSI system has been one of main parts of the research work in this PhD study. This chapter illustrates the fundamental background of hyperspectral imaging technique, the design of the hardware and software development for the HSI system, and the parameters and calibrations of the visible to near-IR (VNIR) HSI system which has been exclusively used for the experiments in this research.

### **2.2 Fundamental of HSI**

Hyperspectral imaging (HSI) has the ability to image the scene in hundreds of contiguous narrow wavebands, with bandwidth  $\sim 10\text{nm}$  or less, in the visible and infrared regions of electro-magnetic spectrum forming image cubes with both spatial and spectral dimensions [5][17] as it is shown in Figure 2-1 (a). Every pixel within the image cube associates with three coordinates, i.e. two spatial ones,  $(x,y)$ , representing location of pixel in 2D space; and one spectral one,  $\lambda$ , representing the wavelength.

Every pixel in the image cube represents the extents of light reflected by the object in the scene within narrow slice of wavebands across the whole spectrum up to limits of the sensitivity of the camera. If the intensity of the reflected light is normalised by the incident light intensity for each image pixel then a reflectance characteristic spectrum of the object in the scene can be obtained (see Figure 2-1 (b)). This is very different from that of the conventional photography which probes three broad colour channels (R,G,B) in the orders of  $\sim 100\text{nm}$  waveband.

The integration of spectral characteristics over broad wavebands tends to reduce the colour discrimination ability in the conventional photography technique, and this is exactly why HSI which uses narrow bandwidth for spectral sensing, has been one of the fastest growing technology in Electro-optics within the 20<sup>th</sup> century [18]. The classification of objects in the scene can be made using the textural features (shape, orientation, intensity variation, and etc.) from a slice of the spectral image, as shown in Figure 2-1 (c), or in combination of features selected from a subset of spectral images across different wavebands.

It is the power of materials discrimination in HSI [19] which makes it to be the primarily technique to be used in this research. One requirement of this work is to sense the blood chromophore and to distinguish it from the body tissue, and then the amount of oxygenation within the blood is quantified through various optical absorption models.



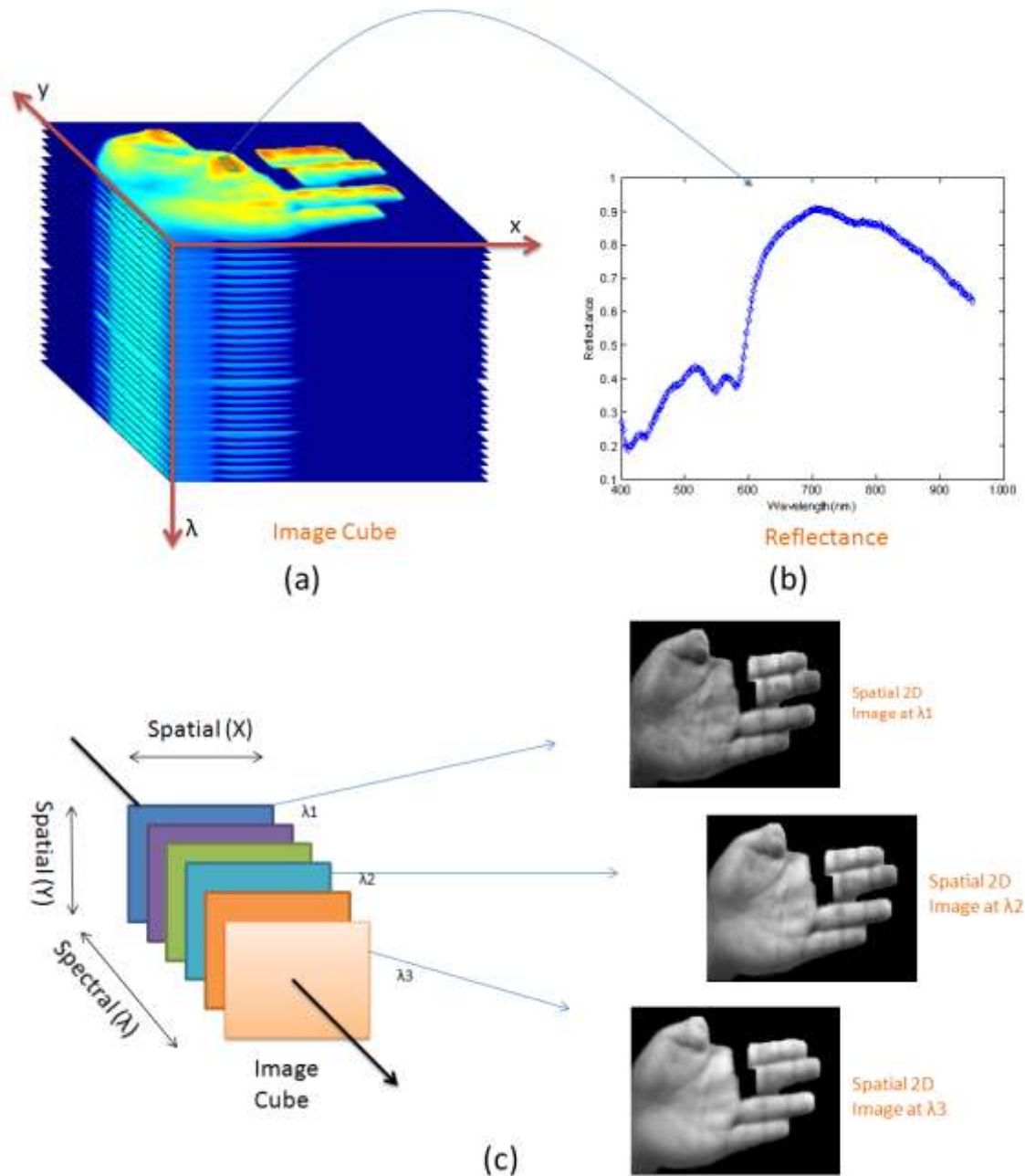
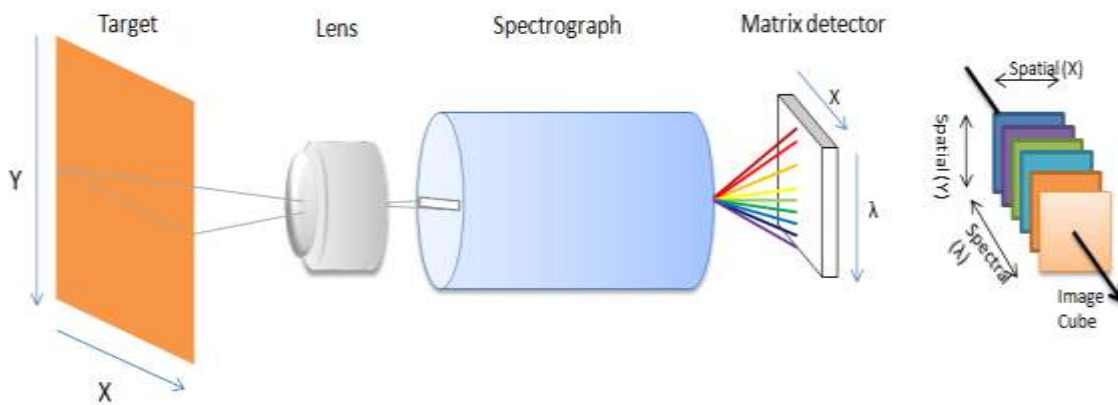


Figure 2-1 (a) illustration of a HSI image which contains hundred to thousand of narrow wavebands forming a 3D image cube. (b) Shows the spectral response in reflectance of the palm tissue for all wavebands within 400-900nm range. This optical signature is unique specific to the chemical composition of the object (palm tissue in this case). (c) shows the 2D image in three different wavebands of the same object (palm).

## 2.3 HSI Instrumentation: An Overview

A typical hyperspectral camera consists of an object lens, a spectrograph, and a camera such as conventional 2D CCD as shown in Figure 2-2. In this configuration only the light reflections from a narrow strip of the scene can pass through the entrance slit and it is then dispersed into a 2D spectrum and subsequently captured by the CCD sensor. One axis of the camera sensor senses the spatial information and the other senses the spectral content, resulting in a 2D spatial-by-spectral information of the 1D strip of the scene (see Figure 2-2). There are two common ways for building a hyperspectral image cube of a scene: one is to move the camera to scan the object, i.e. move the camera in Figure 2-2 along  $Y$  direction of target. An example of this method is to mount a hyperspectral imager on an aircraft which travels at a constant velocity in a push broom motion to build up an image cube of the scene (Figure 2-3(a)). Another method is to scan the scene through a mirror scanner which steers light from different parts of the scene into the camera sensor (Figure 2-3(b)). This latter mirror scanning mode has been adopted for the HSI instrumentation in this study.



**Figure 2-2 typical hyperspectral imaging system consists of an object lens, a spectrograph and a 2D CCD camera**

## 2.4 Spectrograph

In the heart of the HSI instrumentation is the spectral dispersion mechanism which is known as spectrograph, and it exists in various different forms of which

the most common three categories have been the dispersive spectrometer, the Fourier transform interferometer and the narrow band tuneable filter. Details of these spectrographs can be found in the literature by Vagni [20] and the principles of the most commonly employed dispersive and tuneable filter spectrographs for HSI instrumentation have been reviewed by Yuen et al [17].

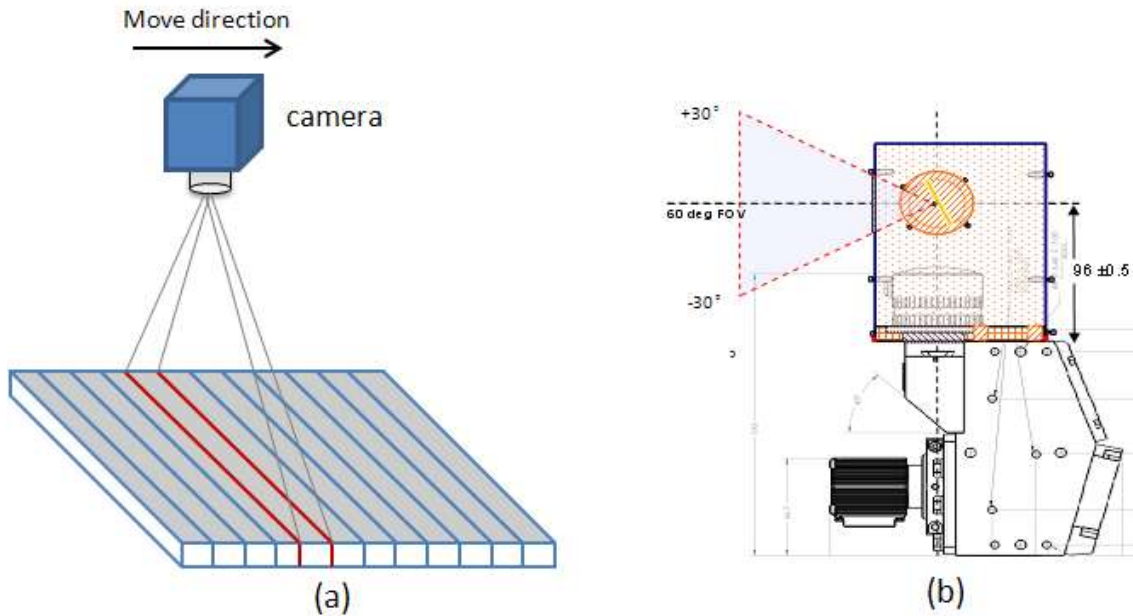


**Figure 2-3 (a) push-broom hyperspectral imaging system by moving the camera along the scene to built up an image cube. (b) Mirror scanner version of the HSI that has been employed in this work for building up image cube [21].**

## 2.5 HSI System @Cranfield

### 2.5.1 Mirror Scanning Systems Design

Commercially available hyperspectral imaging systems are extremely expensive to acquire and in many cases the performances of these off-the-shelf products are very limited. To tailor make for a fit-to-purpose instrumentation we opted to develop our own HSI systems by assembling Commercial-Off-The-Shelf (COTS) components together such as spectrographs, cameras, mirror scanners and device drivers. The whole assembly of HSI system is designed by Dr Peter Yuen, the software for controlling the systems are developed by the author and Mr Kan Hong using C++ (VNIR\_1.0 & SWIR\_1.0 are developed by Kan Hong, VNIR\_2.0, VNIR\_3.0, SWIR\_2.0, and SWIR\_3.0 are developed by the author)

based on the Software Development Kit (SDK) of the hardware, and all the work relating to mirror scanner alignment is finished by the author. There are two hyperspectral imaging systems employed in our lab, Visible Near Infra-red (VNIR) imaging system and Short Wave Infra-red (SWIR) imaging system. The working range of the VNIR one is 400nm-1000nm, and the SWIR one is 900nm-2500nm.

The mirror scanner systems [21] consist of a motor and a mirror, which scans the scene through a step motor. The camera captures one frame of spectral information for every motor step position and it is then stored in the memory of the computer. After a sequence of mirror rotation the spectral information of various parts of the scene are then stacked together to form a hyperspectral image cube. A servo driver board and a dual-axis controller board with independent power supply have been used for driving the motors. The driver electronics and controller boards are housed in a custom-made cooled housing.

The step motor is designed to locate just above the objective lens of the camera through a T-shape aluminium frame as shown in Figure 2-4 (a), which is then in turn fixed onto the body of the spectrograph. Eight adjustable scrub screws have been used for the alignment between the motor axis with respect to the optical path in the camera. Four screws which are labelled as 'F-screw' and 'B-screw' in the figure, have been employed for the adjustment of the front and back end of the motor axis respectively. Ideally this motor axis should be perpendicular to the optical axis (Figure 2-4 (b)). The alignment is achieved using a dummy motor made by perspex which consists of a centred hollow cavity to allow a laser beam to pass through (Figure 2-4 (c)). The 'F' and 'B' screws are adjusted until a parallel laser beam passes through the dummy perspex without hitting the walls of the dummy motor. Subsequently the real motor is then put in place of the Perspex. The steps for aligning the axis of the step motor with respected to the optical path of the camera are as follows:

- A. A line of reference defined by entrance slit of the spectrograph is firstly located (Figure 2-5 (a)), this line is then switched by 90 degree through a prism build-in to the laser system. The F-screws are adjusted such that the

front end of the Perspex cavity lies close to this perpendicular reference line.  
(Figure 2-5 (b)).

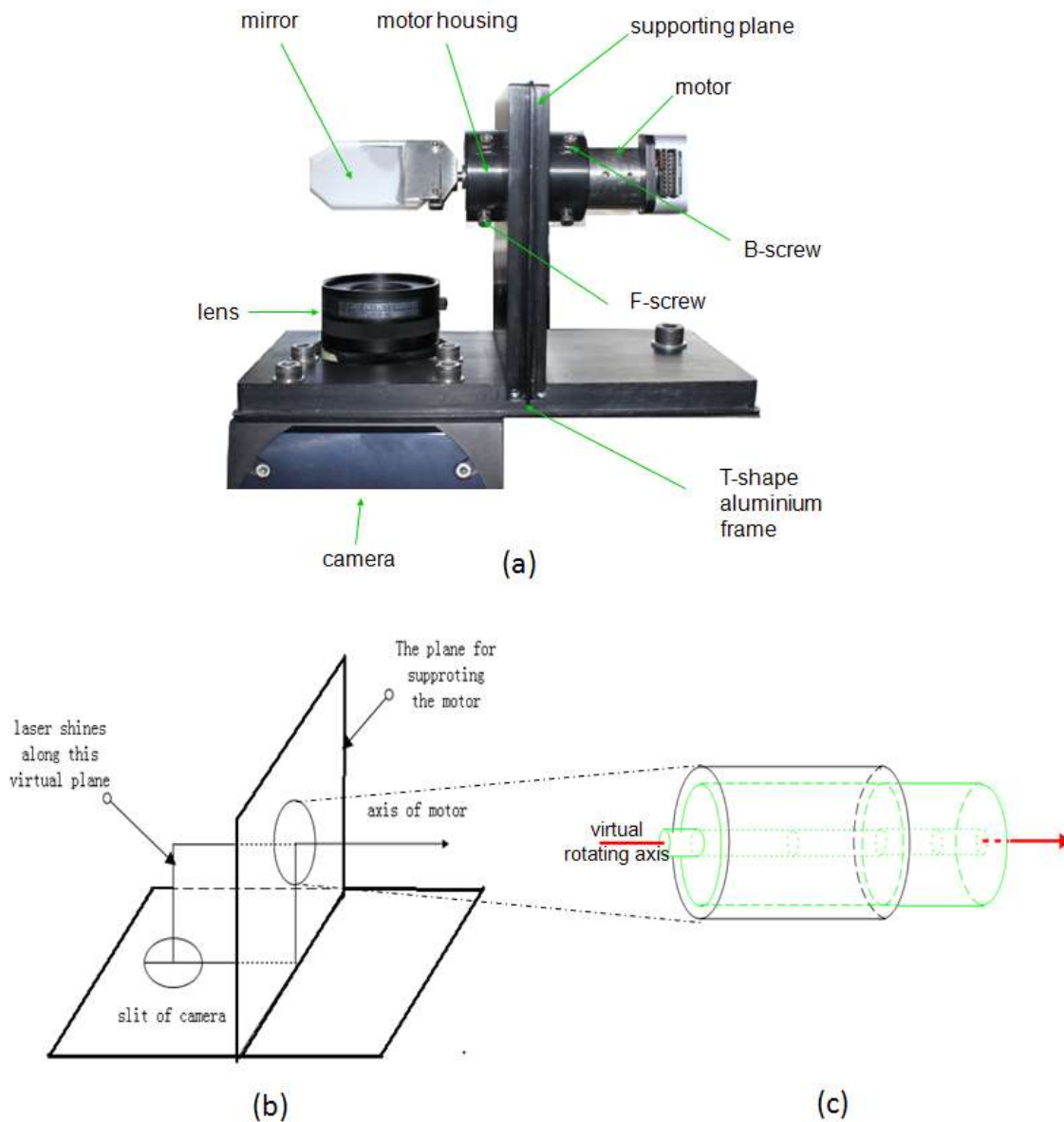


**Figure 2-4 (a) outlines the positioning of the step motor within the mirror scanning system. (b) A schematic view of the T shape motor mount and the reference line defined by the entrance slit of the spectrograph and the rotating axis of the step motor. (c) A schematic view of the motor housing (black) and the motor (green).**

- B. The laser beam is then switched parallel to the entrance slit through the build-in prism such that the laser is directed towards the front end of the cavity of the dummy motor.
- C. Adjust the B-screws at the back end of the dummy motor so that the laser beam passes through the cavity without hitting the wall of the cavity (see Figure 2-6). Note that the F-screws are not touched during this adjustment.

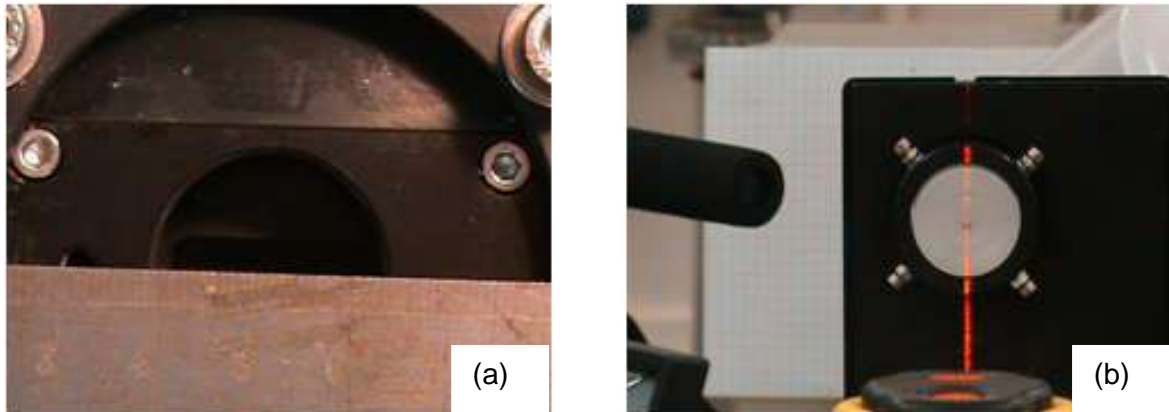


**Figure 2-5 (a) the entrance slit of the spectrograph is highlighted by the edge of the ruler, and a beam of laser is firstly aligned with the slit to define the line of reference. (b) The laser beam is then switched by 90 degree to define the vertical axis of the optical path.**

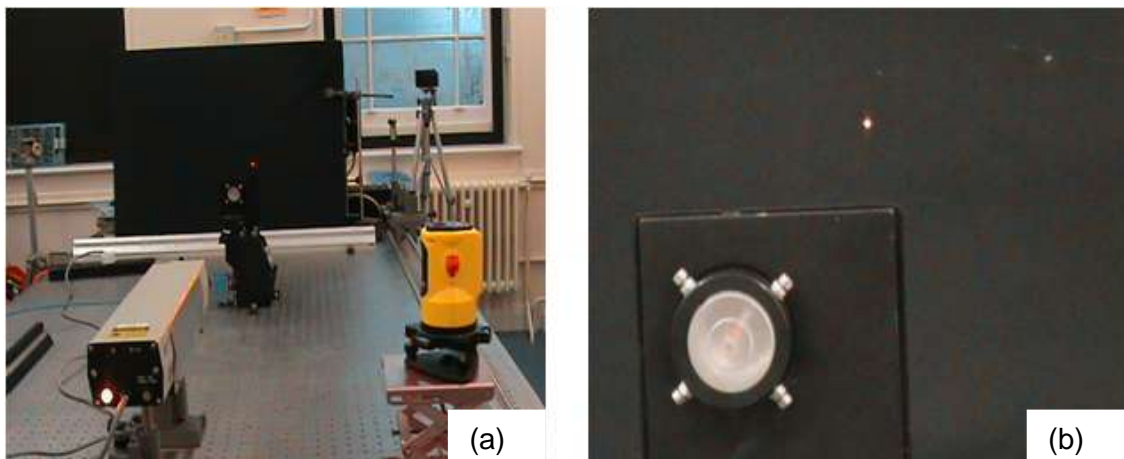


**Figure 2-6 (a) shows the alignment of the laser beam with the motor rotating axis. (b): shows the optimum alignment when the laser beam passes through the cavity of the dummy motor without hitting the Perspex, otherwise the whole Perspex glows when the laser hits the wall of the cavity.**



### 2.5.2 VNIR System Employed in the Project

The dominant chromophores in skin tissue which absorbs appreciable electromagnetic spectrum in the VNIR region (400nm-1000nm) have been Hb, HbO<sub>2</sub> and melanin. Particularly, the Hb and HbO<sub>2</sub> exhibit distinctive absorption features within the visible spectral region. In the short wave IR (SWIR) region between 1-2.5μm, optical absorption is dominated by water in the tissue which makes StO<sub>2</sub> assessment difficult using electro-optic methods. To assess StO<sub>2</sub> (percentage of HbO<sub>2</sub>), VNIR system therefore are employed in this project. The HSI system utilised in this project [21] consists of a Headwall VNIR spectrograph together with a PCO PixelFly camera and with a home-designed mirror scanning system as depicted in Figure 2-8. The slit of the spectrograph is 30μm width giving a maximum spectral resolution of ~5nm. The limit of the spectral sensitivity of the PCO camera ranges from 400nm to 1000nm with a maximum quantum efficiency yield of ~65% at 650nm. The VNIR spectrograph is calibrated by using the well defined emission wavelengths of a mercury lamp. As it is shown in Figure 2-7, the emission peaks of 5 different wavelengths as sensed by the VNIR spectrograph are compared to that of the calibrated spectrometer (Ocean 2000) and a calibration curve is then made.

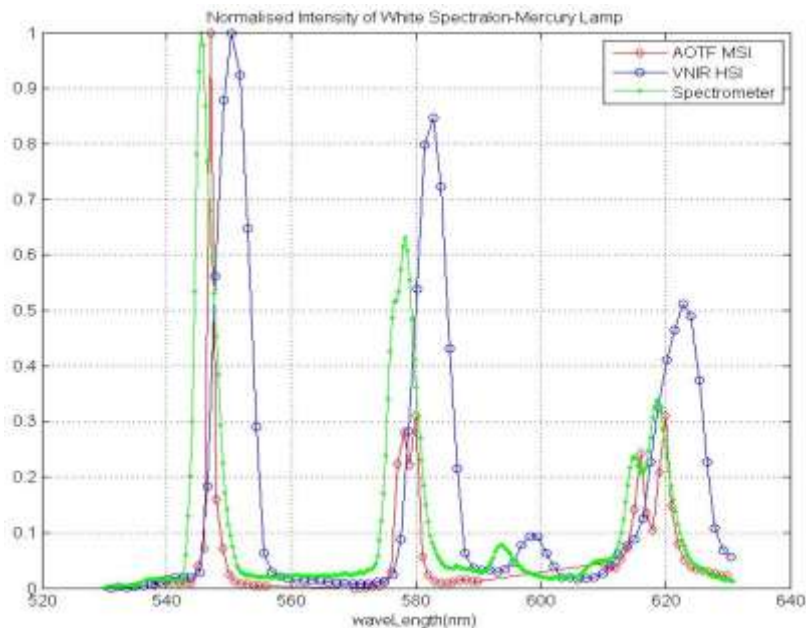


**Figure 2-7 the normalised emission intensity of mercury lamp measured by the VNIR spectrograph (blue) and compares it with the calibrated spectrometers.**

The working scheme of the HSI system is schematically illustrated in Figure 2-9. The control circuit for the motor scanner is housed in a customer designed box. Two PCI boards are included in a PC for controlling the VNIR HSI system. The software VNIR\_3.0 for controlling HSI system is developed by the author using C++ (see appendix). VNIR\_3.0 synchronizes the scanning system and spectrometer to form image cube, which can be transferred into StO<sub>2</sub> map using various forms of diffuse scattering models disused in chapter 4. Depending on the integration time, it takes typically 20 to 30 seconds to capture one image cube of 1300x500 pixels spatial resolutions at 50ms of integration time. The processing of a set of data typically consisting of 100 images will take ~ an hour to convert them into StO<sub>2</sub> maps. The VNIR HSI system functions faultlessly during the course of this work. The captured images, especially when they are presented in a pseudo-RGB format, have been compared favourably with respected to the broad band RGB image.

Comparing with VNIR\_1.0, distinctive features of VNIR\_3.0 include easy-to-use style GUI design, more input voltage options, enhanced display functionality, and new functionality for aiding focusing. A more detailed description of VNIR\_3.0 is in appendix.

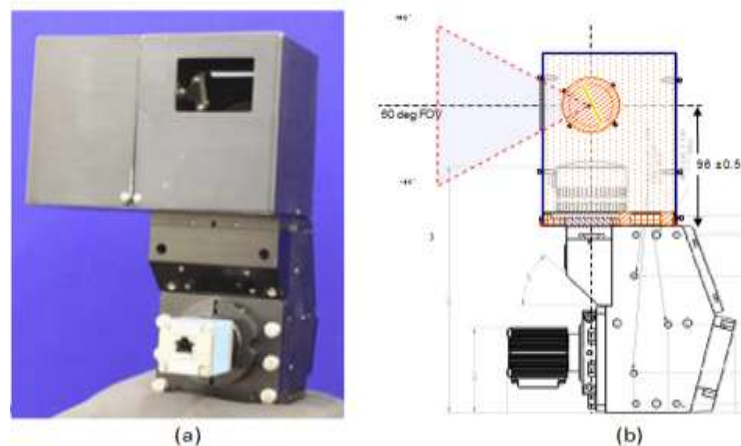


**Figure 2-8 the VNIR Hyperspectral imaging system utilised in this study: (a) Picture of the HSI system which is designed and built [21] during the course of this work (b) schematic drawing of the mirror scanner assembly and the Headwall dispersive spectrograph.**



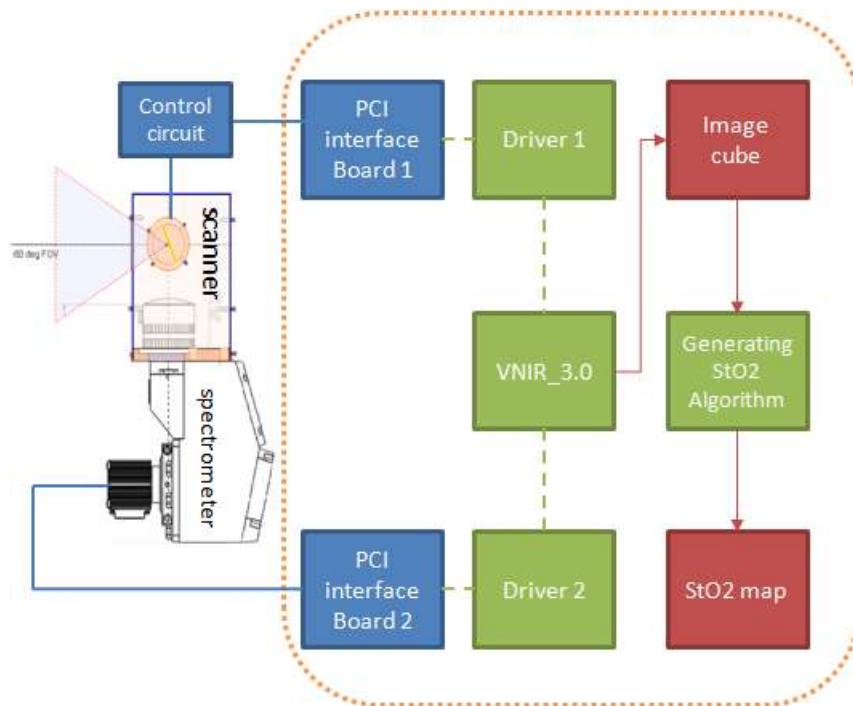


**Figure 2-9 the operational blocks of the HSI system, image acquisition and processing that has been utilised throughout this work.**



## 3 TISSUE OPTICS AND TISSUE OXYGEN SATURATION

### 3.1 Introduction

The haemoglobin oxygen saturation in tissues (StO<sub>2</sub>), as opposed to that of the artery oxygen content which can be measured by pulse technique, has been a difficult subject in biomedical research. This chapter presents the fundamental theory and background knowledge in StO<sub>2</sub> assessment. The basic optical properties such as the absorption and scattering of light are introduced first, and it is then followed by an overview of the physical and optical properties of skin tissue and the underlying chromophores. A brief description of oxygen supplies to the human body tissue with emphasis on the relationship between the tissue blood flow and StO<sub>2</sub> is given here. And lastly, a comprehensive review of previous electro-optical assessment methods for StO<sub>2</sub> is summarised in this chapter.

### 3.2 Optical Properties

#### 3.2.1 Refractive Index

The refractive index of tissue is a dimensionless number determining the speed of light propagating within the tissue. It is defined as

$$n = c / v \quad \text{Equation 3-1}$$

where  $c$  is the speed of light in vacuum and  $v$  is the speed of light in the tissue. At the interface between two media with different refractive index (Figure 3-1), refraction occurs and is described by Snell's law as

$$n_1 \sin \theta_1 = n_2 \sin \theta_2 \quad \text{Equation 3-2}$$

where  $\theta_1$  is angle of incidence, and  $\theta_2$  is angle of refraction. The refractive index for human skin is a function of wavelengths and it takes the form of in the wavelength range of 1000-2200nm [22]

$$n_{skin}(\lambda) = 0.7 \times (1.58 - 8.45 \times 10^{-4} \lambda + 1.1 \times 10^{-6} \lambda^2 - 7.19 \times 10^{-10} \lambda^3 + 2.32 \times 10^{-13} \lambda^4 - 2.98 \times 10^{-17} \lambda^5) + 0.3 \times 1.5$$

**Equation 3-3**

where  $\lambda$  is the wavelength in nanometer. However, the skin refractive index as a whole is normally taken as 1.4[23], which is larger than that of air (refractive index=1).

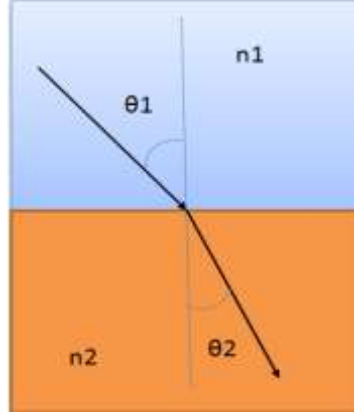


**Figure 3-1 refraction of light between two media with refractive indices of  $n_1$  and  $n_2$  ( $n_1 < n_2$ ).**

### 3.2.2 Absorption

The charge separations of molecules inside a medium can be modulated in a quantized fashion when they are perturbed by photons travelling through the medium. Part of the photon energy is absorbed, causing the intensity of the transmitted light attenuated. As shown in Figure 3-2, for a homogeneous and non-scattering medium with thickness of  $l$ , the transmitted intensity  $I$  is dependent on the incident intensity  $I_0$ , the light travelling path  $l$  and the absorption coefficient  $\mu_a$  of the medium in an exponential manner:

$$I = I_0 e^{-\mu_a l}$$

**Equation 3-4**

where  $\mu_a$  is in the unit of  $\text{cm}^{-1}$  representing the probability of a photon's energy being absorbed by the molecules per unit length.

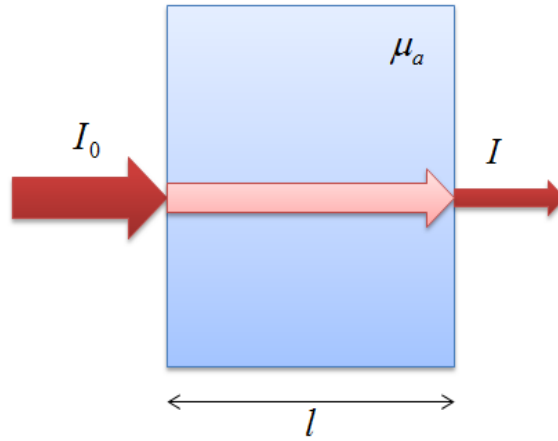


**Figure 3-2 attenuation of light through a non-scattering medium of thickness  $l$**

The parameters measured for probing human tissue in transmission spectroscopy usually are transmittance or absorbance. The transmittance  $T$  is the ratio of transmitted intensity to the incident intensity, being written as

$$T = I / I_0 \quad \text{Equation 3-5}$$

The absorbance  $A$  is related to the transmittance in the form of

$$A = \ln(1/T) \quad \text{Equation 3-6}$$

From Equation 3-4 to Equation 3-6, the relation between absorbance  $A$  and absorption coefficient  $\mu_a$  can be derived. It is known as Beer's Law stating that

$$A = \mu_a l = \varepsilon_a c l \quad \text{Equation 3-7}$$

where  $\varepsilon_a$  is the molar extinction coefficient in the unit of  $\text{cm}^{-1}(\text{mol/L})^{-1}$  (or  $\text{cm}^{-1}\text{M}^{-1}$ ), and  $c$  is the concentration of the absorber or chromophore inside the medium in the unit of  $\text{mol/L}$  (or  $\text{M}$ ). If the absorbance  $A$ , molar extinction coefficient  $\varepsilon_a$ , and travelling length  $l$  are known, the concentration of chromophore inside the medium can be obtained. Beer's law is a fundamental theory for the measurement of chromophore concentration within the medium, such as haemoglobin contained in human tissue.

### 3.2.3 Scattering

Light scattering is characterised by the light deviating from the original propagation direction. The scattering of light inside the medium, such as human tissue, is caused by the fluctuation of refractive index inside the tissue. This fluctuation can be due to the discrete particles with different refractive indexes to the surrounding tissues, or due to the continuous change of the refractive index of tissue. For non-absorption medium, through which light transmits, as shown in Figure 3-3, the incident intensity  $I_0$  is attenuated in the original direction, and the transmitted intensity  $I$  is given by

$$I = I_0 e^{-\mu_s l} \quad \text{Equation 3-8}$$

where  $l$  is light travelling length,  $\mu_s$  is the scattering coefficient, in the unit of  $\text{cm}^{-1}$ , representing the probability of a photon being scattered per unit length.

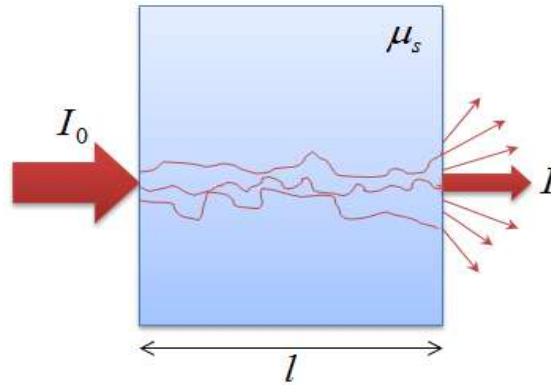


**Figure 3-3 attenuation of light transmitting through non-absorption medium**

When a photon is experiencing scattering event as shown in Figure 3-4, the trajectory of the photon will be deflected by an angle  $\theta$ . The distribution of the deflection angle  $p(\theta)$  is called scattering function and it represents the probability of the deviated photon being scattered into the direction by an angle  $\theta$  with respect to the initial trajectory. An isotropic medium scatters photons in a constant distribution of angle  $\theta$ . Anisotropy  $g$  is the expected value of the cosine of the deflected angles, written as

$$g = \int_{-1}^1 p(\cos \theta) \cos \theta d(\cos \theta) \quad \text{Equation 3-9}$$

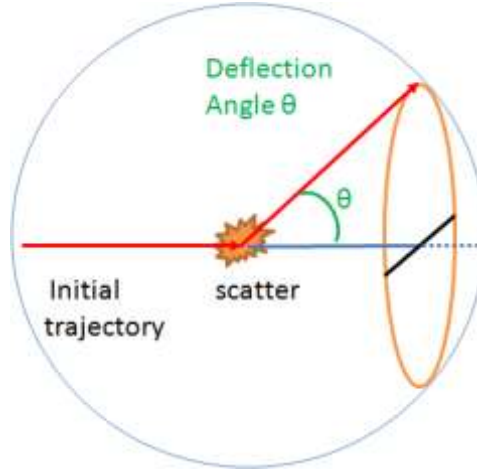


**Figure 3-4 illustration of forward scattering event when the photon is deflected by an angle  $\theta$ .**

A medium with  $g$  equal to 1 is a completely forward scattering medium.  $g$  equal to 0 indicates an isotropic medium, and  $g$  equalling -1 indicates an extremely backward scattering medium. The dermis of human skin, containing blood vessels, is highly forward scattering medium with  $0.74 \leq g \leq 0.85$  [7] in the wavelengths range of 415nm to 800nm. Apart from scattering coefficient describing the scattering properties of a medium, there are two more coefficients, which are transport scattering coefficient and transport attenuation coefficient. The transport (reduced) scattering coefficient  $\mu'_s$  is defined as

$$\mu'_s = \mu_s(1 - g) \quad \text{Equation 3-10}$$

And the transport attenuation coefficient is defined as

$$\mu_t = \mu'_s + \mu_a \quad \text{Equation 3-11}$$

### 3.3 Skin Tissue Optics

#### 3.3.1 Structure of Skin and Its Chromophores

Human body is protected by a layer of waterproof skin (except for nails), called epidermis (see the cross-section illustration of skin in Figure 3-5 ). It is the outermost layer of skin which varies in thickness depending on the exact physical locations of the body [24]. The melanin contained in the epidermis is

the main chromophore in this layer of skin. It absorbs more light in the ultra-violet region than the longer wavelengths regions and protects the human skin from burning by sunlight. The amount of melanin inside the epidermis also determines the skin colour, i.e. the higher the melanin concentration, the darker is the skin colour. There is no blood vessel in the epidermis. The cells in the deepest layer of epidermis are nourished by the diffusion from the blood vessels in dermis, which is a layer right beneath the epidermis. The dermis consists of connective tissue responsible for cushioning the body from physical stress and strain, and it is much thicker than the epidermis. The main chromophore inside the dermis is haemoglobin (oxygenated or deoxygenated) which are the main substances in the blood. Haemoglobin is an oxygen-transport metalloprotein in the red blood cells. Each haemoglobin molecule has the capability to bind to four oxygen molecules. The compound of haemoglobin and oxygen is called oxygenated haemoglobin (oxy-haemoglobin) and it appears in red, which is responsible for the redness of skin colour, such as the flushing face. After the oxygen is consumed, the oxy-haemoglobin turns into deoxygenated haemoglobin (deoxy-haemoglobin), which is in purple blue colour. Beneath the dermis is hypodermis (subcutaneous layer). It is not part of skin anymore and it servers as a layer attaching the skin to the bone and muscles.

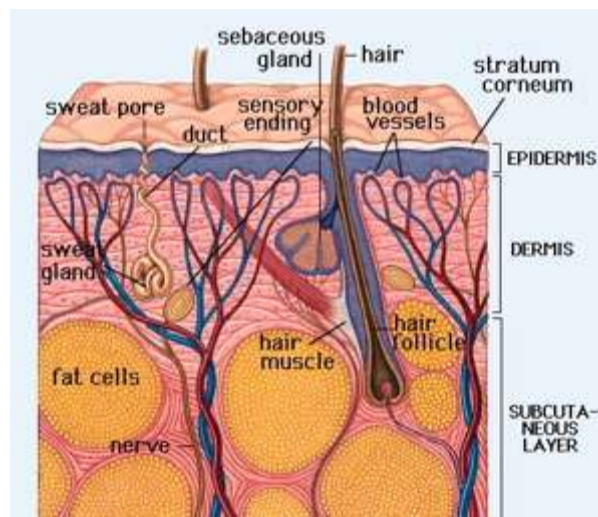


**Figure 3-5 a cross-section illustration of human skin and tissue structure[25].**



### 3.3.2 Absorption Properties of Skin Chromophores

The main chromophores within skin tissue are melanin, oxy-haemoglobin (HbO<sub>2</sub>), and deoxy-haemoglobin (Hb). The molar extinction coefficients of these three chromophores, in the unit of  $\text{cm}^{-1}\text{M}^{-1}$ , as function of wavelengths are shown in Figure 3-6 [26]. It is seen that melanin absorbs more photons in the shorter wavelengths region than that in the longer wavelength region, the extinction coefficient of the melanin drops dramatically as wavelengths increases from 200nm to 800nm. It is nearly 40 times larger in the ultra-violet than that in the near Infrared region. The absorption properties of HbO<sub>2</sub> and Hb are quite distinctive to each other. In the region of 500nm to 600nm, Hb has one prominent absorption peak at about 556nm, while HbO<sub>2</sub> has two absorption peaks at around 542nm and 576nm. In the region of 610nm to 900nm, an absorption dip is observed at around 686nm for HbO<sub>2</sub>, while one peak is seen at around 756nm for Hb. Both Hb and HbO<sub>2</sub> show the strongest absorption

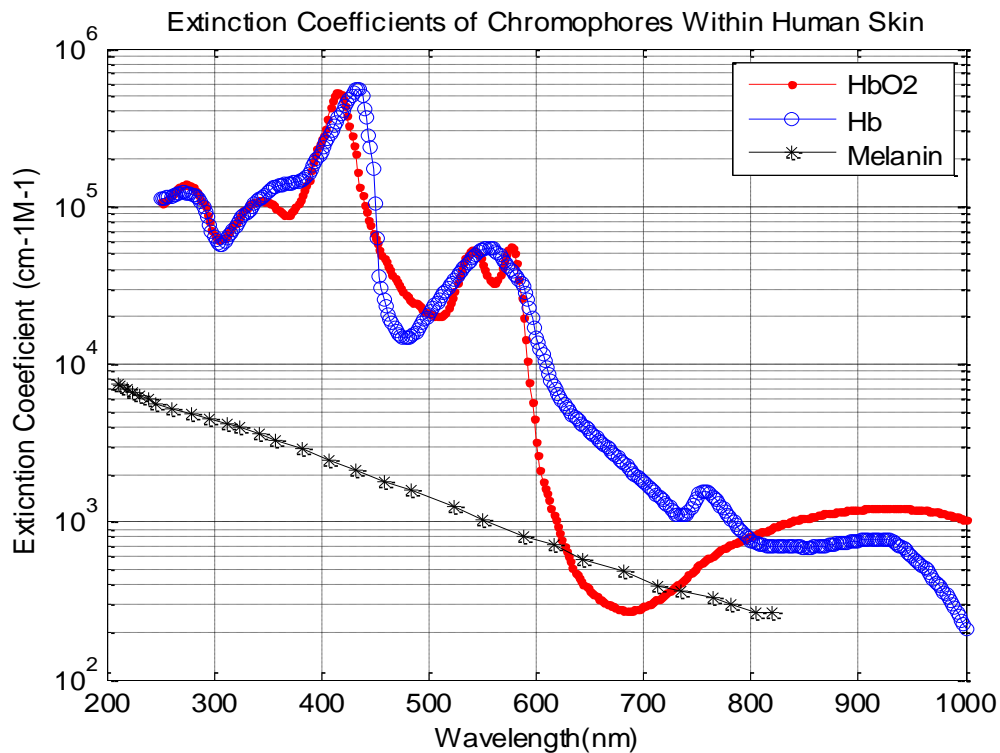
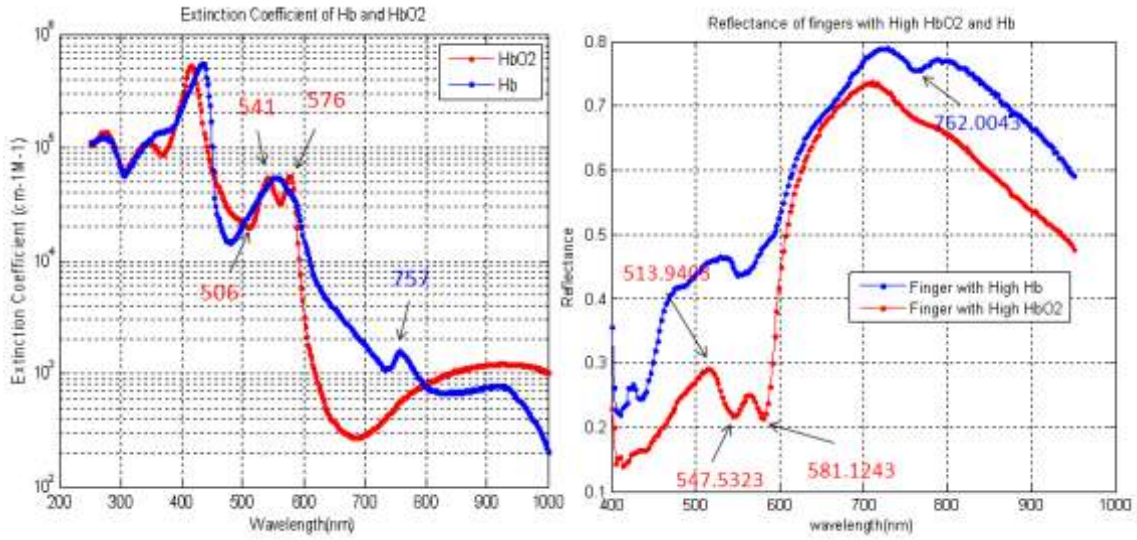


Figure 3-6 molar extinction coefficients of melanin, oxy-haemoglobin (HbO<sub>2</sub>), and deoxy-haemoglobin (Hb) [26] chromophore in human tissue.

properties in the region of 400nm to 450nm with peaks found in 412nm and 434nm for HbO<sub>2</sub> and Hb respectively. The Hb and HbO<sub>2</sub> has the same extinction coefficient at the wavelengths (isosbestic point) of 390nm, 442nm, 452nm, 550nm, 530nm, 545nm, 570nm, 584nm, and 797nm. The very different absorption characteristics of Hb and HbO<sub>2</sub> are highly important for discriminating these two chromophores, and thus deducing the StO<sub>2</sub>.

### **3.3.3 Calibration of Spectrometer**

The extinction coefficients of skin chromophores are vital to the assessment of the StO<sub>2</sub>, and they are adopted from previous publication [26], where the measurement of the coefficients was performed with standard method. However, the spectrometer employed in the measurement may not be the same type as the one that we use in the project. To calibrate the VNIR spectrometer in our project to the one employed in [26]. The ELM reflectance (see section 4.3.1) of a finger having been in ischemia state for 5 minutes and the same finger in hypoxia state has been measured using VNIR spectrometer (see section 2.5.2). It is assumed that the ischemia finger has higher concentration of Hb, whose reflectance thus demonstrates more features of Hb, and the hypoxia finger has more HbO<sub>2</sub>, therefore the reflectance of which resembles that of HbO<sub>2</sub> more. This assumption has been supported by the results shown in Figure 3-7, which illustrates the published extinction coefficients [26] and the reflectance of HbO<sub>2</sub>&Hb respectively. It is seen that in the region of 500nm to 600nm, the two absorption peaks and two absorption dips of the HbO<sub>2</sub> (left panel of Figure 3-7) correspond to the two reflection dips and two reflection peaks of hypoxia finger (right panel of Figure 3-7) very well. It is also obvious that the absorption peak of Hb (left panel of Figure 3-7) in the region of [500 600]nm correlates well to the reflection dip (right panel of Figure 3-7) of the ischemia finger in the same region.



**Figure 3-7** extinction coefficients of HbO2 and Hb (left) [26], and reflectance of fingers with high HbO2 and Hb (right).

Four distinctive wavelengths shown in the left panel of Figure 3-7, 506nm, 541nm, 576nm, and 757nm, are selected for the purpose of calibration. They are absorption peaks/dips of HbO2 or Hb. The corresponding reflection dips/peaks are 513nm, 547nm, 581nm, and 762nm, as shown in the right panel of Figure 3-7. It is assumed that the test wavelength (used in the project) and the standard wavelength (used in [26]) has the relationship

$$T_{\lambda} = aS_{\lambda} + b \quad \text{Equation 3-12}$$

where  $T_{\lambda}$  and  $S_{\lambda}$  represent test wavelength and standard wavelength,  $a$  and  $b$  are constants. By performing linear regression using data points  $(T_{\lambda}, S_{\lambda})$  ((506,513), (541,547), (576,581), (757,762)), the constant  $a$  and  $b$  are found to be 0.9908 and 11.6502 respectively.

### 3.4 Background of Tissue Oxygen Supplies

When air is inhaled into the lung the oxygen is bound to the haemoglobin forming oxy-haemoglobin which is an unstable and reversible bond. The oxy-haemoglobins appear in bright red colour and they are transported to every part of body through arterial blood vessels and capillaries. After the oxygen is consumed by cells of tissues, oxy-haemoglobins are decomposed into deoxy-

haemoglobins which exhibit purple-blue colour, they are then returned back to the heart through the venous blood vessels and subsequently back to the lung, where the next cycle of deoxy-haemoglobin binding to oxygen to form new oxy-haemoglobin happens again.

Each haemoglobin molecule is capable of binding to four oxygen molecules. If all four binding sites of every haemoglobin molecule are occupied by oxygen molecules, the oxygen saturation of the haemoglobin will be 100%. However, the blood leaving from the lung normally has haemoglobin oxygen saturation in the range of 90-100% depending on persons and situations. The factors that affect the oxygen saturation depend on partial pressure of oxygen ( $PO_2$ ), concentration of carbon dioxide ( $CO_2$ ), concentration of the metabolite 2,3 diphosphoglycerate (2,3-DPG), temperature, and the concentration of lactic acid (pH). As shown in Figure 3-8, the oxygen-haemoglobin dissociation curve [27]

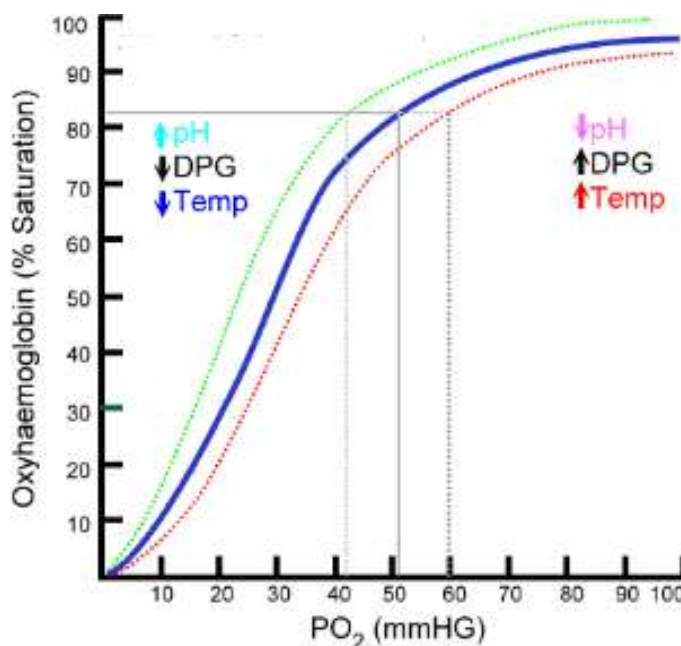


**Figure 3-8 oxygen-haemoglobin Dissociation Curve [27].** The higher is the partial pressure of oxygen, the higher the haemoglobin oxygen saturation. The temperature, concentration of  $CO_2$ , DPG, and lactic acid are inversely affecting the oxygenation saturation.

quantifies the oxygen saturation of haemoglobin in the vertical axis dependent on the partial pressure of oxygen in the horizontal axis. The higher the partial

pressure of oxygen will promote higher haemoglobin oxygen saturation. The temperature, concentration of CO<sub>2</sub>, DPG, and lactic acid are inversely proportional to the saturation, i.e. the higher the temperature, the lower the saturation. Inside the lung, high oxygen concentration (high partial oxygen pressure) makes a high saturation rate.

### 3.5 Tissue Blood Flow and Oxygen Content

The survival and functioning of tissue rely on blood supply through the capillary bed of network. In the front end of the capillary bed is arteriole branching from the artery, which provides blood supplies of high concentration of oxy-haemoglobin. At the back end of the capillary bed is the venule capillary which joins to the vein, from which it collects the blood with slightly depleted oxygenations as shown in Figure 3-9.

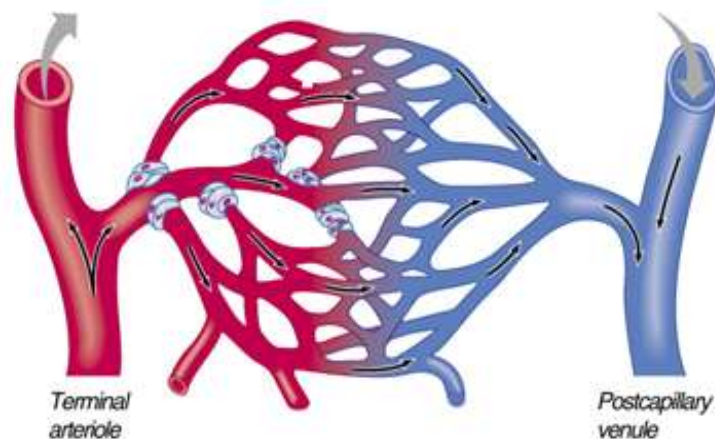


**Figure 3-9 arteriole, capillary bed, and venule [28]. Capillary bed connects arteriole and venule which supply oxygen to the tissue.**

The arteriole and venule oxygen content in the tissue is a function of haemoglobin level and the oxygen saturation:

$$C_a = HL \times K \times SaO_2 \quad \text{Equation 3-13}$$

$$C_v = HL \times K \times SvO_2 \quad \text{Equation 3-14}$$

$$BF_a = BF_v = BF_c$$

**Equation 3-15**

$$C_v = C_a - VO_2 / BF_c$$

**Equation 3-16**

where  $K$  is constant, 1.34 ml oxygen/g haemoglobin represents the oxygen content of 100% oxygen saturated haemoglobin.  $BF_a$  (ml blood/min) is the arteriole blood flow,  $SaO_2$ (%) is the arteriole haemoglobin oxygen saturation,  $C_a$  (ml oxygen/ml blood) is the arteriole oxygen content,  $HL$  (g haemoglobin/ml blood) is the total haemoglobin level in the blood,  $BF_v$  (ml blood/min) is the venule blood flow,  $SvO_2$  (%) is the venule haemoglobin oxygen saturation,  $C_v$  (ml oxygen/ml blood) is the venule oxygen content,  $VO_2$  (ml oxygen/min) is the oxygen consumption of tissue, and blood flow of the capillary bed is  $BF_c$  (ml blood/min).

The tissue oxygen content, i.e. the oxygen content in the capillary bed  $C_c$ , is a value between arteriole oxygen content  $C_a$  and venule oxygen content  $C_v$  at any period of time ( $C_a > C_c > C_v$ ). According to the Equation 3-13 and Equation 3-14,  $SaO_2$  and  $SvO_2$  are positively proportional to  $C_a$  and  $C_v$  respectively, and therefore the tissue (capillary bed) haemoglobin oxygen saturation  $ScO_2$  is also in the range of  $SvO_2$  to  $SaO_2$  ( $SaO_2 > ScO_2 > SvO_2$ ). Thus, a higher  $SvO_2$  or  $C_v$  indicates a higher  $ScO_2$  or  $C_c$ .

The increase of blood flow can raise the venous oxygen content as long as the tissue oxygen consumption  $VO_2$  keeps constant, according to the Equation 3-16 under the assumption that arterial oxygen content is constant or higher. The oxygen consumption is related to the tissue metabolic rate, which is shown to be hardly affected by the variation of the blood flow [29][30][31] in the not highly-activate tissue, or by adrenaline infusion which increases the blood flow [32]. Therefore, an increase of blood flow in many cases may increase the venous oxygen content  $C_v$  and also the tissue oxygen content  $C_c$ .

It is one of the objectives in this research for the detection of the increase of oxygenation in the tissue and in the blood from a stand-off distance when the subject is excited by various stimulations and emotions.

### 3.6 Tissue Oxygen Saturation

The haemoglobin oxygen saturation ( $SO_2$ ) is defined as the ratio of the amount of oxy-haemoglobin to the total amount of haemoglobin:

$$SO_2 = HbO_2 / (HbO_2 + Hb) \quad \text{Equation 3-17}$$

The arterial blood exhibits relatively strong heart rate pulsation and its haemoglobin oxygen saturation is called Arterial Oxygen Saturation ( $SaO_2$ ) and is most often measured by pulse oxymetry technique [33]. The  $SaO_2$  is fairly constant varying between 90-99% for healthy persons. Tissue Oxygen Saturation ( $StO_2$ ) is the  $SO_2$  of the microcirculation in the tissue, which can be any levels between ~60% of the venous  $SO_2$  to ~98% of the  $SaO_2$  [34][35]. Organs and tissues  $StO_2$  in many cases cannot be assessed using pulse oxymetry method due to the lack of the pulsation in these blood streams. For example, in wound healing after surgical operation [36], intra-capillary  $StO_2$  such as organ ischemia after surgical transplant [37], cerebral brain  $StO_2$  for neonate monitor [34] etc, alternative techniques such as spectroscopy based absorption method [38] using local probes such as in spectrophotometry [36], or large area imaging based Hyperspectral imaging techniques [38], have been the principal ways for the non-invasive assessment of non-arterial blood oxygenation.

$StO_2$  is an indicator of oxygen delivery and consumptions by the organ tissue and it is widely utilised in many clinical applications. In [1], Bezemer et al monitored the forearm and thenar  $StO_2$  of nine healthy volunteers when they were in supine and upright positions. The heart beat was found to increase significantly ( $P < 0.001$ ) if the posture was changed from supine to upright, which indicated a hemodynamic changes. The forearm  $StO_2$  response to these hemodynamic changes very well, i.e. significantly lower ( $P < 0.001$ )  $StO_2$  on forearm was observed in the upright position compared to supine, which supported that the forearm  $StO_2$  could be a sensitive parameter for detecting central hypovolemia and hypovolemic shock in trauma patients. Wang et al [2] used  $StO_2$  as an indicator to discriminate 19 necrotizing fasciitis from 215 soft

tissue infection, it was found that the StO<sub>2</sub> of the limbs that were infected by necrotizing fasciitis was significantly lower than that of normal limbs or limbs with simple infection, and that the receiver operation characteristics (ROC) curve of StO<sub>2</sub> at 70% for discriminating necrotizing fasciitis gave an AUC of 0.883, which suggested that low StO<sub>2</sub> in the lower extremities of the body might associate with high risks of necrotizing fasciitis. Cheng et al [3] employed total haemoglobin concentration (HbT) and StO<sub>2</sub> for the diagnosis of breast cancer based on the hypothesis that cancers might cause greater vascularisation and consume more oxygen than normal tissues. The threshold of contrast-normalized standard deviation of HbT/StO<sub>2</sub> and the threshold of relative HbT/StO<sub>2</sub> average were set as 0.3 and 1 respectively, ductal carcinoma were detected from mammogram positive lesion if the related thresholds were crossed. Under these criteria, the detection has reached 92% sensitivity and 67% specificity. Yudovsky et al [39] measured the maximum differences of Hb and HbO<sub>2</sub> concentrations between suspected and surrounding areas to produce ulceration prediction index. His result was based on an image processing algorithm for predicting the ulceration risk. The prediction sensitivity and specificity had been reported as 95% and 80% respectively. In [13], it was found from our laboratory that emotions, such as anxiety, triggered re-distribution of blood supplies in the human facial regions. Thus the blood oxygenation in the face (or face StO<sub>2</sub>) can be employed as a physiological feature for the detection and possibly classification of emotions (see chapter 8 for more information).

### **3.7 Electro-optical Assessment Methods for Tissue Oxygen Saturation**

#### **3.7.1 Conventional Oxygen Saturation Assessments: Oximetry**

Based on Beer-Lambert law, oximetry measures the haemoglobin oxygen saturation of the pulsation blood within the probe volume of tissues upon illumination. The method measures the intensity of the transmitted light through the tissue, such as fingertips or earlobes. Under the assumption that deoxy-haemoglobin and oxy-haemoglobin are the only two substances absorbing the



light in the blood, the transmitted intensity through the illuminated tissue, as shown in a simplified model in Figure 3-10, can be determined by incident intensity as:

$$I = I_{in} 10^{-(\alpha_o C_o + \alpha_D C_D)l} \quad \text{Equation 3-18}$$

where  $\alpha_o$  and  $\alpha_D$  are specific extinction coefficients of oxy-haemoglobin and deoxy-haemoglobin respectively.  $C_o$  and  $C_D$  are concentration of oxy-haemoglobin and deoxy-haemoglobin in the arterial blood respectively. And  $l$  is the path length of the light in the arterial blood vessels.

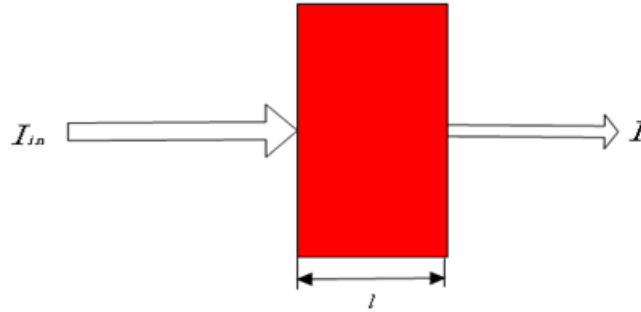


**Figure 3-10 a simplified model of oximeter: Transmitted intensity  $I$  is measured for an incident intensity  $I_{in}$  using Beer-Lambert law.**

For two different wavelengths  $\lambda_1$  and  $\lambda_2$  which exhibit appreciable absorption then Equation 3-18 becomes

$$I_1 = I_{in1} 10^{-(\alpha_{o1} C_o + \alpha_{D1} C_D)l} \quad \text{Equation 3-19}$$

and

$$I_2 = I_{in2} 10^{-(\alpha_{o2} C_o + \alpha_{D2} C_D)l} \quad \text{Equation 3-20}$$

where  $\alpha_{o1}$  and  $\alpha_{o2}$  are specific extinction coefficients of oxy-haemoglobin at wavelength at  $\lambda_1$  and  $\lambda_2$  respectively.  $\alpha_{D1}$  and  $\alpha_{D2}$  are specific extinction coefficients of deoxy-haemoglobin at wavelengths  $\lambda_1$  and  $\lambda_2$ .

If a ratio  $R$  is defined as the absorbance of the blood at  $\lambda_1$  to the absorbance at  $\lambda_2$

$$R = \frac{\log_{10}(I_1 / I_{in1})}{\log_{10}(I_2 / I_{in2})} = \frac{\alpha_{O1}C_O + \alpha_{D1}C_D}{\alpha_{O2}C_O + \alpha_{D2}C_D} = \frac{Absorbance_1}{Absorbance_2} . \quad \text{Equation 3-21}$$

Then we have,

$$R(\alpha_{O2}C_O + \alpha_{D2}C_D) = \alpha_{O1}C_O + \alpha_{D1}C_D \quad \text{Equation 3-22}$$

and

$$(R\alpha_{O2} - \alpha_{O1})C_O = (\alpha_{D1} - R\alpha_{D2})C_D . \quad \text{Equation 3-23}$$

Thus the tissue oxygen saturation of pulsation blood is

$$StO_2 = \frac{C_O}{C_O + C_D} = \frac{\alpha_{D1} - R\alpha_{D2}}{R(\alpha_{O2} - \alpha_{D2}) + \alpha_{D1} - \alpha_{O1}} . \quad \text{Equation 3-24}$$

At selected wavelengths  $\lambda_1$  and  $\lambda_2$ , the  $\alpha_{O1}$ ,  $\alpha_{O2}$ ,  $\alpha_{D1}$ , and  $\alpha_{D2}$  are constants and therefore the  $StO_2$  can be determined solely from the measurement of  $R$  by the oximeter.

### 3.7.2 Hyperspectral Imaging Method for Oxygen Assessment

Hyperspectral imaging technique collects reflected lights from the tissue including the skin surface as well as the epidermis layer. In 2003 Zuzak et al [6][9] reported a multispectral imaging (MSI) system for assessing the tissue haemoglobin oxygen saturation of palm and the schematic of his multispectral imaging system is shown in Figure 3-11 (a). Their method involved a pre-calibration procedure using 100% pure deoxy-haemoglobin (Hb) and oxy-haemoglobin (HbO<sub>2</sub>) samples [40] and they were then used for all other data analysis. The absorbance (520nm-640nm) of these standard samples, as shown in Figure 3-11 (b), was employed for the deconvolution of the measured absorbance in a least square manner to deduce the concentration of oxy-haemoglobin in the test tissue. The effectiveness of this method for the assessment of  $StO_2$  is qualitatively validated using various degrees of infusion by Nitric Oxide (NO) or L-NG-monomethyl Arginine (L-NMMA) for varying the perfusion of blood flow rate to the palm. Inhalation of NO can increase the blood

flow rate, while L-NMMA is an inhibitor of NO. The results as shown in Figure 3-12 exhibited a consistent trend of increasing StO<sub>2</sub> of the palm when NO was inhaled, and a gradual reduction of StO<sub>2</sub> when the L-NMMA was applied. Cancio et al [41] also employed apparent absorbance of oxy-haemoglobin, deoxy-haemoglobin, and skin between 500nm to 600nm at 5nm steps to assess tissue oxygen saturation. The oxy-haemoglobin (HbO<sub>2</sub>) and deoxy-haemoglobin (Hb) concentrations were regarded as fit coefficients under multi-linear regression. The tissue oxygen saturation (StO<sub>2</sub>) of the pig's skin deduced by HSI showed a lower value of StO<sub>2</sub> after bleeding in comparison to the base line (Figure 3-13).

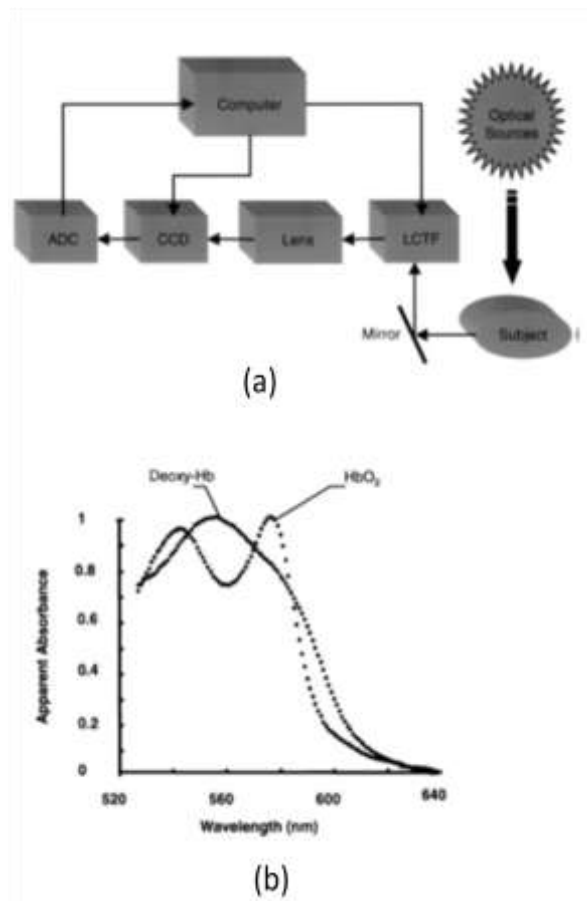


**Figure 3-11 (a): schematic block diagram of Zuzak's HSI for assessing the oxy-haemoglobin concentration of tissue. (b): shows the absorbance of 100% pure oxy-haemoglobin and deoxy-haemoglobin used by Zuzak as reference data [6]**

Yudovsky et al [39] considered the melanin in the skin as the third absorbers, and they also applied a geometry-dependent constant to take account of the

specular reflection by skin in their StO<sub>2</sub> assessments. They adopted similar un-mixing technique as that of Zuzak's work for fitting the HSI data collected between 500nm to 660nm [39]. Unlike Zuzak's work, Yudovsky et al adopted the molar extinction coefficients of Hb, HbO<sub>2</sub> and melanin from the literature [7][42][43][44] as the reference data. Based on this methodology it was reported that the ulceration of the foot in diabetes patients had been predicted with sensitivity and specificity of 95% and 80% respectively [39].

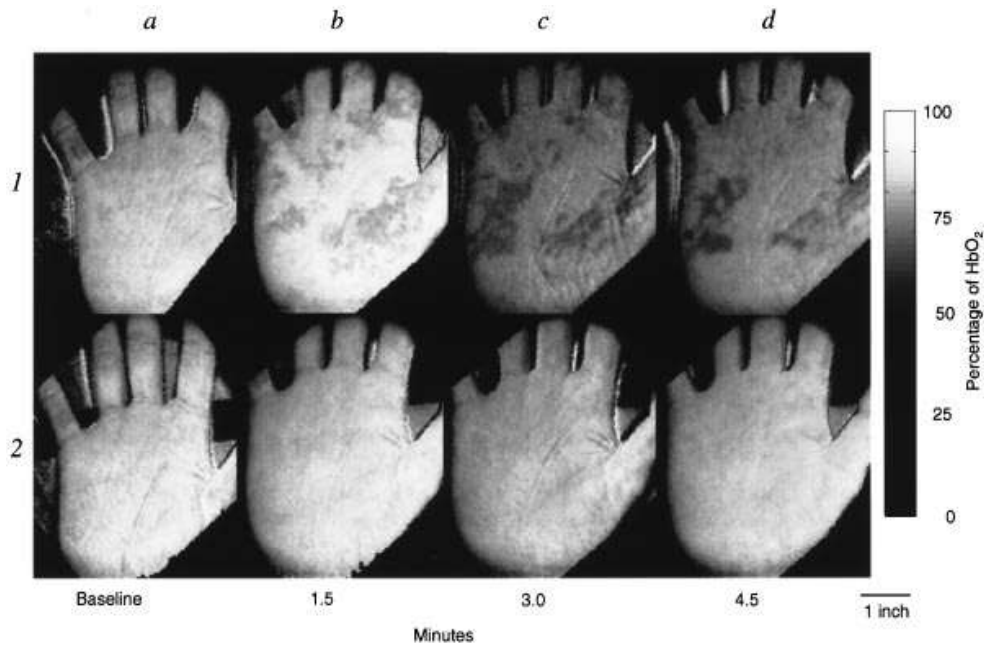


**Figure 3-12 shows the early work performed by Zuzak [6] presenting the HbO<sub>2</sub> in grey scale image of the palm: Rows 1 and 2 after the subject inhaled ambient air and NO respectively. a, Baseline condition; b, L-NMMA infused for 1.5 minutes; c, after 3.0 minutes of L-NMMA; and d, after 4.5 minutes of L-NMMA. Note that the StO<sub>2</sub> is seen to reduce (darker in grey scale) across a-d columns when the blood flow rate is reduced further by the L-NMMA.**

The StO<sub>2</sub> assessment using hyperspectral imaging techniques can give 2D information of StO<sub>2</sub> distribution. The multilinear regression is normally employed to deduce the concentration of Hb and HbO<sub>2</sub> from equation set developed based on the Beer Lambert Law. Either two chromophores (Hb and HbO<sub>2</sub>) [9][6][8] or three chromophores (Hb, HbO<sub>2</sub>, and melanin) are considered [45][39] in the equation set. The scattering effect has been taken into account in very recent publication [39]. The research of StO<sub>2</sub> assessment based on HSI

techniques is still in its infancy. Among all the publications available, different people use different Beer Lambert models. And the region of wavelengths employed for generating StO<sub>2</sub> is varying very much as well.

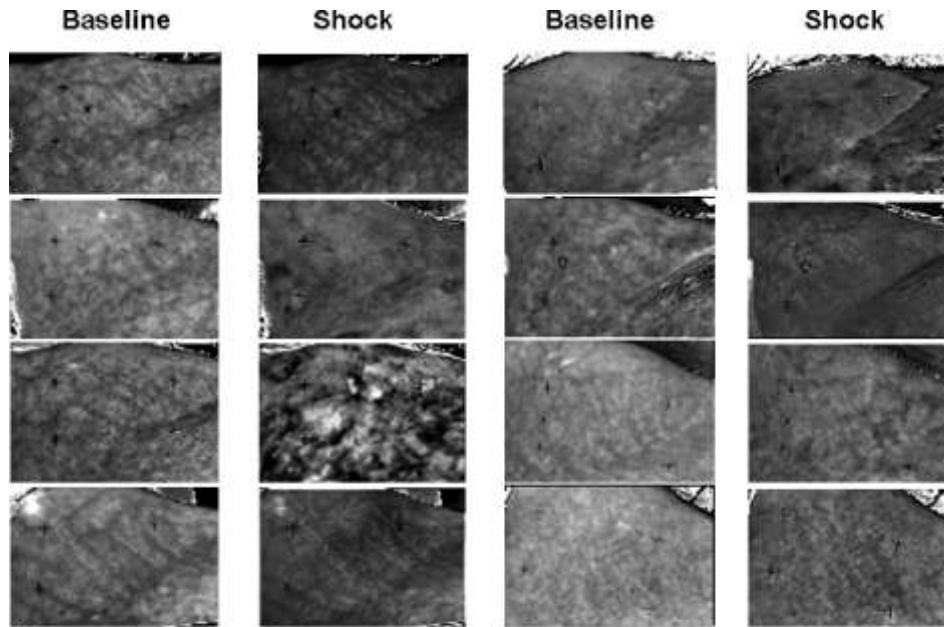


**Figure 3-13 the StO<sub>2</sub> of pig's skin presented in grey scale [41]. The brighter the colour, the higher the StO<sub>2</sub>. The baseline of the skin StO<sub>2</sub> is in first and third column, and the StO<sub>2</sub> after bleeding is in the second and fourth column. It is seen that the pig's skin baseline StO<sub>2</sub> are higher than that after the pig bleed.**

### 3.7.3 Thermal Imaging

The temperature of human skin can be measured by thermal imaging system from a stand-off distance. The blood flow under the skin can roughly be estimated using blood perfusion models [46][16][47] on the skin temperature. As mentioned in section 3.5, the blood flow in the tissue may be proportional to the StO<sub>2</sub> particularly when the oxygen consumption in tissue is kept constant. In most cases the oxygen consumption by the not highly-activate tissues has been found quite constant [29][30][31] [32].

Pavlidis [16] presented a blood perfusion model for transferring skin temperature into blood flow based on heat transfer model. It was shown that the blood flow is inversely proportional to the square of the difference of the skin

temperature to the core temperature of human body. The relation between blood flow rate and skin temperature proposed in [16] has the form of:

$$\frac{dV_s}{dt} = \frac{T_B(C_s + \frac{K_c}{3D}) - CdT_s}{(T_B - T_s)^2} \frac{dT_s}{dt} \quad \text{Equation 3-25}$$

where  $V_s$  is the skin blood flow rate,  $T_B$  is core body temperature equal to 310K,  $C_s$  is heat capacity of skin,  $K_c$  is thermal conductivity of skin (0.168kcal/m/h/K),  $D$  is the distance from the core temperature point to the skin surface,  $C$  is a constant, and  $T_s$  is the skin temperature. As the term  $T_B(C_s + \frac{K_c}{3D}) - CdT_s$  is a constant, the  $(\frac{dV_s}{dt})$  is proportional to the temperature change rate of the skin  $(\frac{dT_s}{dt})$ . Based on this blood perfusion model, the skin temperature map of a human as shown in Figure 3-14 (a) can be translated into blood flow rate as shown in Figure 3-14 (b).

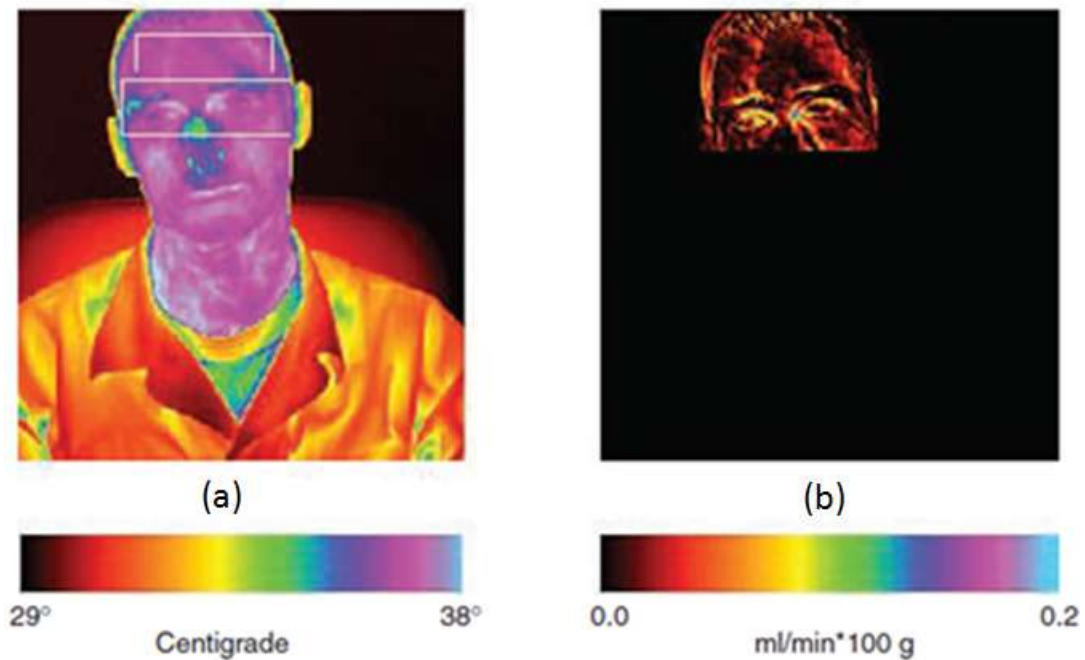


**Figure 3-14 (a) skin temperature of a human face. (b) the blood flow rate map deduced by the blood transfusion model [16]**

Two more blood perfusion models have been developed in [47][48]. The skin blood flow rate is modelled by Fujimasha[47] as

$$V_s = [K_r \varepsilon (T_s^4 - T_w^4) + 0.58 \times 10^{-2} \times D^{-0.25} (T_s - T_a)^{1.25} + 1.85 \times 10^{-2} - \frac{K_c (T_c - T_s)}{3d} - M_o \times S \times 2^{(T_s - T_m)/10}] / \alpha \rho S (T_b - T_s) \quad \text{Equation 3-26}$$

where  $K_r = 4.88 \times 10^{-3} (\frac{kcal}{m^2 h K})$ ,  $T_s$  is skin temperature,  $\varepsilon$  is skin emissivity (0.98),  $T_w$  is wall temperature,  $D$  is diameter of a model,  $T_a$  is room temperature,  $K_c = 0.168 (\frac{kcal}{m^2 h K})$ ,  $T_c$  is deep body temperature,  $d$  is the distance from core temperature point to the skin surface,  $M_o = 1.44 \times 10^{-2}$ ,  $S$  is the thickness of skin,  $T_m$  is normal tissue temperature ( $=309K$ ),  $\alpha$  is a parameter for countering heat exchange ratio in a warm condition ( $=0.8$ ),  $\rho$  is heat capacity of blood ( $=0.92cal/ml/K$ ), and  $T_b$  is blood temperature in the core.

Xie[48] presented a simplified blood perfusion model by taking into account of the skin and environment temperatures in the form of :

$$WR = \frac{(4T^3 T_\alpha - 3T^4 - T_e^4)T}{(T_\alpha - T)^2 (T^4 - T_e^4)} \quad \text{Equation 3-27}$$

where  $WR$  is blood perfusion,  $T$  is skin temperature,  $T_\alpha = 312.15K$ ,  $T_e$  is environment temperature. In normal conditions, where  $T \geq 300K$ , Equation 3-27 can be simplified into:

$$WR = \frac{T}{(T_\alpha - T)^2} \quad \text{Equation 3-28}$$





## **4 MODEL AND WAVELENGTH SELECTION FOR HYPERSPSCTRAL IMAGING TISSUE OXYGEN SATURATION**

### **4.1 Motive of Research**

Hyperspectral imaging (HSI) has been one of the emerging techniques for the remote sensing of tissue oxygen saturation (StO<sub>2</sub>) in-vitro and the result can be presented in a form of a spatial 2D StO<sub>2</sub> map. Rather than using monochromatic LED light sources [34] or optical fibre probe [4], which can only be used for probing average StO<sub>2</sub> of local regions of body tissue, HSI has the capability to visualise the distribution of oxygen saturation across the whole tissue in a non-contact way. All previous work reported in the field [49][50][39][51][52][53][9][45][41][54][55][10][38][37][36] has commonly adopted a few, or, a range of specific wavelengths, within the visible region (VIS) of 550-600nm [55][54][41][39][45][37] or in the near infra-red (NIR) of 600-1050nm wavelengths [38][36][53] using various forms of Beer-Lambert (BL) formulations for the StO<sub>2</sub> assessment. However, none of the reported work ever attempted to elucidate why these wavelengths were chosen in their work, nor is there any information whatsoever to explain what the effects on selecting the wavelengths other than their chosen ones are. Apart from the wavelength, different authors use different BL formulations all over the literatures in the public domain. It is not clear whether the basic BL formulation or the extended version would be more appropriate for the data collected from the spectral regions of VIS or NIR for a better measurement of the tissue StO<sub>2</sub>. In this project, we aim to address these issues and find the most suitable wavelengths and BL model for a reproducible and accurate StO<sub>2</sub> assessment via controlled experiment.

## 4.2 Overview of Algorithms for StO2 Assessment

### 4.2.1 Beer Lambert Law: Revisited

A great deal of work in the field of StO2 assessment has been based upon the Beer-Lambert Law (BL) which relates the absorption of light to the properties of the material through which the light is travelling:

$$A = \epsilon c l = \alpha l \quad \text{Equation 4-1}$$

where  $A$  is the absorbance,  $\epsilon$  is the molar extinction coefficient ( $\text{cm}^{-1}(\text{mol/L})^{-1}$ ) (or molar absorptivity) of the material,  $c$  is the molar concentration ( $\text{mol/L}$ ) of the absorber,  $l$  is the distance ( $\text{cm}$ ) where the light travels through the material,  $\alpha$  is the absorption coefficient ( $\text{cm}^{-1}$ ) of the chromophores. Equation 4-1 implies that the absorbance is linear with the concentration of chromophores. If the path length  $l$  and the molar absorptivity  $\epsilon$  are known and the absorbance  $A$  is measured, the concentration  $c$  of the substance can be deduced.

However, in HSI reflectance model, the path length  $l$  can hardly be measured. The product  $lc$  in Equation 4-1 is thus reduced to  $C_{eff}$ , named as effective concentration ( $10^{-3}\text{mol/cm}^2$ ), which represents molar concentration of absorbers per unit area.

If only HbO2 and Hb are taken as two main chromophores for the HSI data recorded in the range of visible to near infrared region, which is similar to the cases performed previously [8][6], the BL formulation can be written as

$$A = \epsilon_{HbO2} C_{effHbO2} + \epsilon_{Hb} C_{effHb} \quad \text{Equation 4-2}$$

where  $\epsilon_{HbO2}$ ,  $\epsilon_{Hb}$  and  $C_{effHbO2}$ ,  $C_{effHb}$  are the molar absorptivity and the effective concentrations of HbO2 and Hb respectively. And the Equation 4-2 is named as two-chromophore Beer Lambert Law (BL2C) formulation in this thesis.

If HbO2, Hb, and melanin are taken as the main chromophores for the StO2 assessment, then the basic BL model will be in the form of:

$$A = \varepsilon_{HbO_2} C_{effHbO_2} + \varepsilon_{Hb} C_{effHb} + \varepsilon_{melanin} C_{effmelanin} \quad \text{Equation 4-3}$$

where  $\varepsilon_{melanin}$  and  $C_{effmelanin}$  are the molar absorptivity and the effective concentration of the melanin in the skin. And Equation 4-3 is acronym as three-chromophore Beer Lambert Law (BL3C) formulation.

#### 4.2.2 Modified Beer Lambert Law [56][57]

In the basic BL model it is assumed that the photon passes through the material without being scattered. In practise photons are scattered into different paths inside inhomogeneous turbid material like the body tissue, and some of them are simply lost after multiple scattering leaving only a small fraction of photons following the pathways and they are then collected by the detector. The path lengths of these photons travelled is much longer than the inter-optical distance  $l$  of the detector probes, and it is typically 4-6 times of  $l$  in live body tissue [56]. Thus the basic BL law in Equation 4-1 is commonly modified into [56][57]:

$$A = \varepsilon c \times DPF + G \quad \text{Equation 4-4}$$

where  $DPF$  is the ‘differential path length factor’ to reflect the effective optical path length,  $G$  is the portion of photons that is lost due to the scatters. Equation 4-4 is commonly known as the modified Beer Lambert (MBL) law. Note that the  $DPF$  is not a constant and it exhibits wavelength dependence behaviour [58].

In many cases the effective photon mean free path  $l \times DPF$  is unknown and many authors in the field [39][45][49][41][54][55][10][38][37][36] have approximated the  $DPF$  as a wavelength independent constant and to replace the  $l \times DPF \times c$  with effective concentration  $C_{eff}$  turning Equation 4-4 into:

$$A = \varepsilon C_{eff} + G \quad \text{Equation 4-5}$$

Equation 4-5 is commonly known as the extended Beer Lambert (EBL) formulation. And for two chromophores of Hb and HbO<sub>2</sub> which are the main absorbers in dermis tissue within the visible to near infrared (NIR) region [8][54], then Equation 4-5 becomes:

$$A = \varepsilon_{HbO2} C_{effHbO2} + \varepsilon_{Hb} C_{effHb} + G \quad \text{Equation 4-6}$$

where  $\varepsilon_{HbO2}$ ,  $\varepsilon_{Hb}$  and  $C_{effHbO2}$ ,  $C_{effHb}$  are the molar absorptivity and the effective concentrations of HbO2 and Hb respectively. Equation 4-6 is named as the two-chromophore extended Beer Lambert (EBL2C) formulation and the parameter  $G$  has been treated as the collection of photons that have been scattered out of the angle of view of the sensors [39], as well as those specularly reflected by the epidermis [10] and the regression offset residues [55] [41].

Due to the wavelength-dependent nature of the reflection from the melanin within the epidermis [59], the  $G$  term in Equation 4-6 is often further split into two components [39][49][60]:

$$A = \varepsilon_{HbO2} C_{effHbO2} + \varepsilon_{Hb} C_{effHb} + \varepsilon_{melanin} C_{effmelanin} + G' \quad \text{Equation 4-7}$$

where  $\varepsilon_{melanin}$  and  $C_{effmelanin}$  are the molar absorptivity and the effective concentration of the melanin in the skin, and the term  $G'$  represents all other factors not related to the tissue absorption such as specular reflection of the skin and the regression errors. Equation 4-7 is named as three-chromophore extended Beer Lambert (EBL3C) formulation.

### 4.3 Methodology for the StO2 Assessment in This Research

#### 4.3.1 Tissue Absorbance

The absorbance in this work is deduced from the diffuse reflections of the body tissue via:

$$A_{\lambda} = \ln\left(\frac{1}{R_{\lambda}}\right) \quad \text{Equation 4-8}$$

where  $A_{\lambda}$  and  $R_{\lambda}$  are the absorbance and reflectance of the target, in this case, the body tissue. The wavelength-dependent  $R_{\lambda}$  is obtained through the empirical line method (ELM) as follows:

$$R(x, y, \lambda) = a_{\lambda} I(x, y, \lambda) + b_{\lambda} \quad \text{Equation 4-9}$$

where  $I(x, y, \lambda)$  is the intensity of pixel  $(x, y)$  at wavelength  $\lambda$ , and  $a_{\lambda}$  and  $b_{\lambda}$  are calibration coefficients extracted from standard reflection material (spectralon):

$$R_{white\_ \lambda} = a_{\lambda} I_{white\_ \lambda} + b_{\lambda} \quad \text{Equation 4-10}$$

$$R_{black\_ \lambda} = a_{\lambda} I_{black\_ \lambda} + b_{\lambda} \quad \text{Equation 4-11}$$

where  $I_{white\_ \lambda}$  and  $I_{black\_ \lambda}$  are mean pixel intensities of the white and black spectralons at wavelength  $\lambda$ ,  $R_{white\_ \lambda}$  and  $R_{black\_ \lambda}$  are reflectance of white and black spectralons, which are 0.98 and 0.02 respectively over spectral region of 250nm-2500nm range in this project.

#### 4.3.2 StO2 Assessment and Error Estimation

In all cases the molar absorptivity or the extinction coefficient of pure oxy-haemoglobin  $\varepsilon_{HbO_2}$  and the pure deoxy-haemoglobin  $\varepsilon_{Hb}$  have been adopted from literature [26] as illustrated in Figure 3-6. The  $\varepsilon_{melanin}$  is adopted from [61], fitted by equation

$$\varepsilon_{melanin} = \frac{10^6 \times \lambda^{-1.5} + 1.5 \times 10^{13} \times \lambda^{-4}}{0.3745 - 2.7957 \times 10^{-4} \times \lambda} \quad \text{Equation 4-12}$$

where  $\lambda$  is the wavelength in the unit of  $nm$ .

The effective concentrations  $C_{eff}$  is extracted through the deconvolution of the BL equation, which can be written in matrix form as:

$$A = EC_{eff} \quad \text{Equation 4-13}$$

For BL2C formulation, the matrix form is

$$\begin{bmatrix} A_{(x,y,\lambda 1)} \\ A_{(x,y,\lambda 2)} \\ \vdots \\ A_{(x,y,\lambda n)} \end{bmatrix} = \begin{bmatrix} \varepsilon_{HbO2\lambda 1} & \varepsilon_{Hb\lambda 1} \\ \varepsilon_{HbO2\lambda 2} & \varepsilon_{Hb\lambda 2} \\ \vdots & \vdots \\ \varepsilon_{HbO2\lambda n} & \varepsilon_{Hb\lambda n} \end{bmatrix} \begin{bmatrix} C_{effHbO2}(x, y) \\ C_{effHb}(x, y) \end{bmatrix} \quad \text{Equation 4-14}$$

For EBL2C formulation, the matrix form is

$$\begin{bmatrix} A_{(x,y,\lambda 1)} \\ A_{(x,y,\lambda 2)} \\ \vdots \\ A_{(x,y,\lambda n)} \end{bmatrix} = \begin{bmatrix} \varepsilon_{HbO2\lambda 1} & \varepsilon_{Hb\lambda 1} & 1 \\ \varepsilon_{HbO2\lambda 2} & \varepsilon_{Hb\lambda 2} & 1 \\ \vdots & \vdots & \vdots \\ \varepsilon_{HbO2\lambda n} & \varepsilon_{Hb\lambda n} & 1 \end{bmatrix} \begin{bmatrix} C_{effHbO2}(x, y) \\ C_{effHb}(x, y) \\ G(x, y) \end{bmatrix} \quad \text{Equation 4-15}$$

For BL3C formulation, the matrix form is

$$\begin{bmatrix} A_{(x,y,\lambda 1)} \\ A_{(x,y,\lambda 2)} \\ \vdots \\ A_{(x,y,\lambda n)} \end{bmatrix} = \begin{bmatrix} \varepsilon_{HbO2\lambda 1} & \varepsilon_{Hb\lambda 1} & \varepsilon_{Melanin\lambda 1} \\ \varepsilon_{HbO2\lambda 2} & \varepsilon_{Hb\lambda 2} & \varepsilon_{Melanin\lambda 2} \\ \vdots & \vdots & \vdots \\ \varepsilon_{HbO2\lambda n} & \varepsilon_{Hb\lambda n} & \varepsilon_{Melanin\lambda n} \end{bmatrix} \begin{bmatrix} C_{effHbO2}(x, y) \\ C_{effHb}(x, y) \\ C_{effmelanin}(x, y) \end{bmatrix} \quad \text{Equation 4-16}$$

And for EBL3C formulation, the matrix form is

$$\begin{bmatrix} A_{(x,y,\lambda 1)} \\ A_{(x,y,\lambda 2)} \\ \vdots \\ A_{(x,y,\lambda n)} \end{bmatrix} = \begin{bmatrix} \varepsilon_{HbO2\lambda 1} & \varepsilon_{Hb\lambda 1} & \varepsilon_{Melanin\lambda 1} & 1 \\ \varepsilon_{HbO2\lambda 2} & \varepsilon_{Hb\lambda 2} & \varepsilon_{Melanin\lambda 2} & 1 \\ \vdots & \vdots & \vdots & \vdots \\ \varepsilon_{HbO2\lambda n} & \varepsilon_{Hb\lambda n} & \varepsilon_{Melanin\lambda n} & 1 \end{bmatrix} \begin{bmatrix} C_{effHbO2}(x, y) \\ C_{effHb}(x, y) \\ C_{effmelanin}(x, y) \\ G(x, y) \end{bmatrix} \quad \text{Equation 4-17}$$

where  $A_{(x,y,\lambda n)}$  is absorbance at pixel location  $(x, y)$  in the scene at wavelength  $\lambda n$ .  $\varepsilon_{HbO2\lambda n}$ ,  $\varepsilon_{Hb\lambda n}$ , and  $\varepsilon_{melanin\lambda n}$  are molar extinction coefficient of HbO<sub>2</sub>, Hb, and melanin at wavelength  $\lambda n$ .  $C_{eff}(x, y)$  and  $G(x, y)$  are effective concentration and scattering compensation constant at location  $(x, y)$  respectively. The modelled effective concentration matrix  $C_{mod}$  can be obtained:

$$C_{\text{mod}} = (E' E)^{-1} E' A \quad \text{Equation 4-18}$$

The error of the model per wavelength can be obtained through the root mean square of the  $C_{\text{mod}}$  with respect to the measured absorbance:

$$\text{Error} = \| (A - EC_{\text{mod}}) \| / (N \| A \|) \quad \text{Equation 4-19}$$

where  $N$  is the number of the wavelength utilised in the model for the StO<sub>2</sub> assessment.

The spectral region spanning from 450nm to 850nm at incremental steps of 2nm, 5nm, 10nm, 15nm, and 20nm, have been utilised in this experiment. It is found that a minimum model error has been obtained when incremental step of 2nm is used. For example, in the spectral subset region of 516nm to 580nm, the model errors for the StO<sub>2</sub> assessment using the extended Beer Lambert law model without specular reflection factor (EBL3C model and see section 4.5.4 for more information) are found to be 1.27%, 1.57%, 1.98%, 2.68%, and 3.1% when incremental steps of 2nm, 5nm, 10nm, 15nm, and 20nm are used respectively. Thus a step increment of 2nm has been used throughout this work.

#### 4.4 Experimental Conditions

This work uses human's palm as the target to illustrate the effects of various factors that may interfere with the assessment of StO<sub>2</sub> correctly.

The halogen lamps with light diffuser have been utilised for the illumination sources in all experiments. Two different illumination conditions have been performed in this work, firstly, the light is illuminated from the top as shown in Figure 4-1(a), such that the top part of the palm receives more of the thermal irradiance from the halogen lamp. Secondly the illumination source is directed from the front so that the front part of the target, in this case the palm, receives more of the irradiance (Figure 4-1 (b)). For most of the non-robust diffuse scattering models, the StO<sub>2</sub> results are seen to be very different under these two extreme illumination conditions. Other illumination angles, such as +60° to -

60° with respect to the normal, have exhibited smaller changes of StO<sub>2</sub> of the same target (palm). Hence the StO<sub>2</sub> results of the target palm under the extreme conditions of top and front illuminations are selected to present in this chapter.

In order to establish high and low StO<sub>2</sub> of the same target within one single image, the blood flow of two fingers is temporary restricted by a rubber band inducing a short term ischemia condition. The StO<sub>2</sub> of the ischemia fingers together with the undisturbed fingers and palm is probed by HSI in every minute interval. It is found that the StO<sub>2</sub> of the ischemia fingers stays quite stable (change of StO<sub>2</sub> less than ~1%) after 2 minutes of ischemia state. Hence all data presented in this chapter was obtained after 3 minutes of ischemia state to ensure reproducible results.

Standard white and black spectralons with reflectance of 0.98 and 0.02 respectively over wavelength range of 250nm to 2500nm, have been deployed in all cases to obtain reflectance through the Empirical Line Method (ELM) [62]. The position of spectralons is fixed which is used as spectral and position reference. The target palm is positioned in front of the spectralons in all experiments to maintain the same sampling geometry.



**Figure 4-1 depicts the two experimental conditions of (a) Illumination from the top of the palm and (b) Illumination sources is directed from the front towards the palm (not shown). Standard reflectors such as the white and black spectralons are situated at the back of the scene.**



## 4.5 Wavelength and Model Selection for StO2 Assessment

### 4.5.1 Whole Spectra or Subset Spectra: Regression Plane

#### 4.5.1.1 BL2C Model

It is seen from section 4.2.1 that the relationship between the absorbance  $A$  and the effective concentrations  $C_{eff}$  is in the form of  $A = \varepsilon_{HbO2}C_{effHbO2} + \varepsilon_{Hb}C_{effHb}$ , if  $A$  conforms to the BL2C formulation. In this case, the data points of  $(A, \varepsilon_{HbO2}, \varepsilon_{Hb})$  at all wavelengths should lay along a plane determined by  $C_{effHbO2}$  and  $C_{effHb}$ , which are constants to be deduced and independent of wavelengths. In this research,  $A$  has been taken as the mean absorbance of a Region of Interest (ROI) of the target palm mentioned in section 4.4 over a spectral range of 450nm to 850nm. Three ROIs located at the top (ROI1), middle (ROI2), and bottom (ROI3) part of the palm have been randomly selected, producing mean absorbance of  $A1$ ,  $A2$ , and  $A3$  respectively. The ROIs are shown in the inset of Figure 4-2 (a), Figure 4-2 (c), Figure 4-2 (e), and each of which contains around 200 pixels. The scatter plots of  $(A1, \varepsilon_{HbO2}, \varepsilon_{HbO2})$ ,  $(A2, \varepsilon_{HbO2}, \varepsilon_{HbO2})$ , and  $(A3, \varepsilon_{HbO2}, \varepsilon_{HbO2})$  are shown in the top, middle, and bottom row of Figure 4-2 respectively. Two different view angles of the same data from each ROI have been presented in Figure 4-2 to check if the data points  $(A, \varepsilon_{HbO2}, \varepsilon_{Hb})$  really conform to a flat plane structure. The left column of Figure 4-2 shows the scatter plot using view angle of azimuth=-95.5°, elevation=16°, and right column gives the same plot using view angle of azimuth=156.5°, elevation=22°. To produce diversified levels of StO2 within the same image, the forefinger and middle finger of the palm are put in ischemia condition for about 3 minutes.

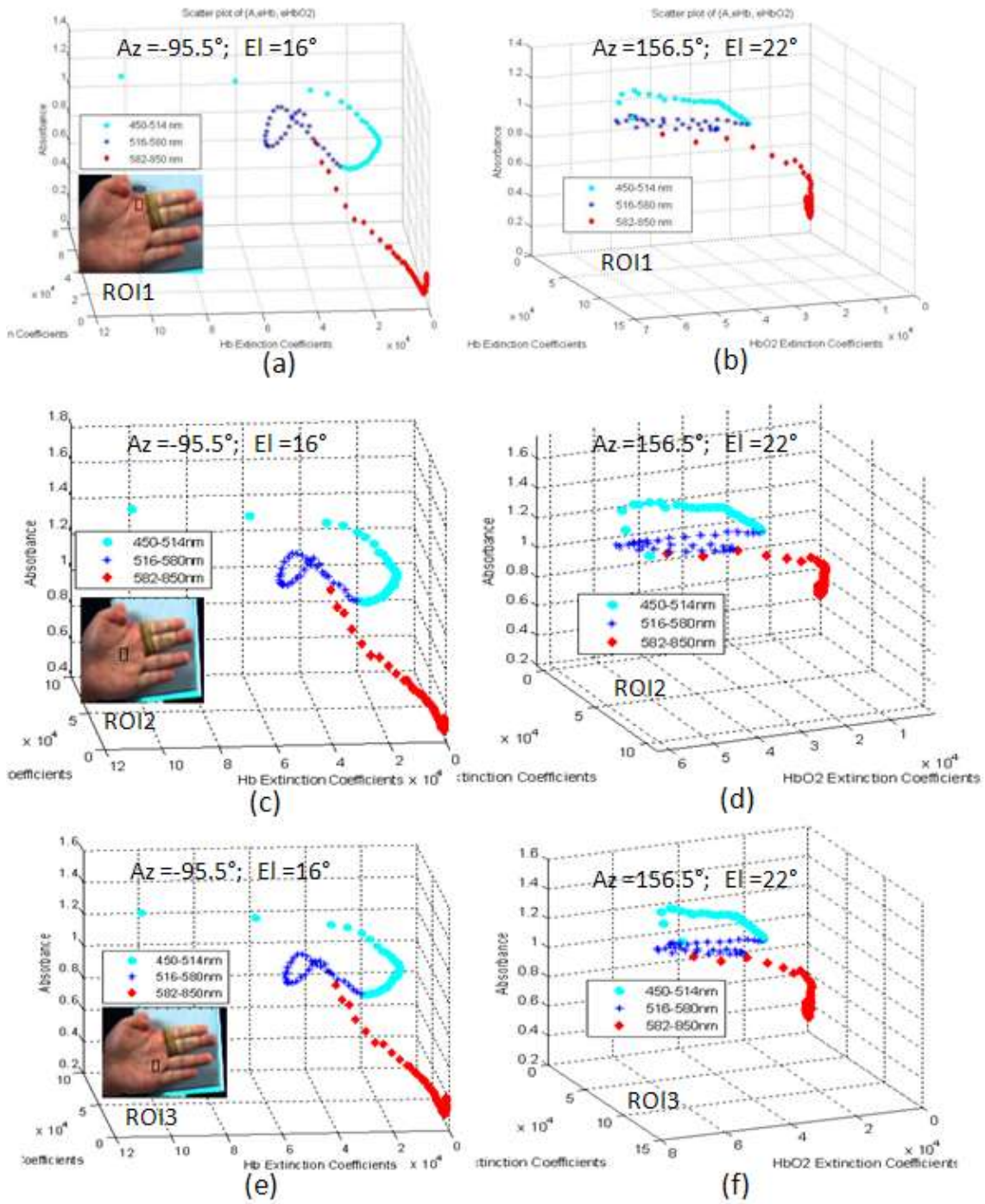


Figure 4-2 shows different views of the 3D scatter plot ( $A, \epsilon_{HbO_2}, \epsilon_{Hb}$ ) over the spectral regions of 450nm to 850nm range, where  $A$  is the apparent absorbance of the ROIs of the palm (inset) without taking into account the tissue scattering and melanin absorption. The view angles for the left column are azimuth=-95.5°, elevation=16°, and right column are azimuth=156.5°, elevation=22°. Note that the data points are seen to form at least 3 different planes (not drawn in the figure) oriented at three different angles to each other.

It is seen that the scatter plots viewed at the same angle resemble each other, though the  $A$  used in each plot is the mean absorbance of different ROIs. It is also observed from the figure that there are at least 3 different planes that can be formulated by the data points within 3 subsets of wavelength regions, i.e. 450 to 514nm, 516 to 580nm, and 582 to 850nm. These 3 regions of data points have been marked in three different colours of cyan, blue, and red as shown in the figure, and the planes have been missed out in the figure deliberately for better clarity. However, it is still obvious that the three planes formed by the three subsets of spectra, are seen to orient at different angles to each others, which indicates that there are at least 3 completely different sets of  $C_{eff}$  can be deduced from the data points over the whole data range from 450nm to 850nm under the BL2C Model.

The scatter plots in Figure 4-2 are produced under assumption that the tissue absorbance  $A$  conforms to the basic BL2C model (Equation 4-2) which does not take into account the effect of tissue scattering, specular reflection due to skin and optical absorption by melanin. It is immediately obvious from Figure 4-2 that the diffuse reflections from body tissue over the whole spectra from 450nm to 850nm do not conform to the basic BL model, because of the existence of at least 3 different solutions given by the 3 different planes as seen in Figure 4-2. Other factors such as skin scattering and melanin absorption may need to be considered.

#### 4.5.1.2 EBL3C Model

Figure 4-3 plots the same data as that presented in Figure 4-2. As the results that presented in section 4.5.1.1 have indicated similar scatter plots over three different ROIs, the data of only one ROI, such as ROI1, is selected for a representative presentation of the StO<sub>2</sub> assessment in this chapter (see Figure 4-3). The tissue absorbance here is obtained by excluding the specular reflections due to the skin through the  $G'$  term according to Equation 4-7, and epidermis absorptions by melanin ( $\epsilon_{melanin}C_{effmelanin}$ ) according to the EBL3C model (see Equation 4-7). Note that the  $G'$  term is a constant, and the melanin term is a slow varying function of wavelength. Both effects are comparative

small particularly in the long wavelength region, and the tissue absorbance after removing these terms is shown in Figure 4-3 (a) which is in close resemblance to that of the uncorrected one as depicted in Figure 4-2. The model solution of the EBL3C for fitting all data points within 450nm to 850nm wavelengths is depicted in a coloured plane as shown in Figure 4-3 (b). It is seen that the EBL3C solution plane cuts the data points predominately in the region between 520nm and 620nm and a few points at about 470nm and 770nm, as it is revealed in Figure 4-3 (c). The StO<sub>2</sub> image given by the solution of the EBL3C model exhibits very large error of ~22.4% showing large part of the palm having StO<sub>2</sub> of only ~60% (Figure 4-3 (d)), which in fact is ought to be at ~95% oxygenation (see section 4.5.2).

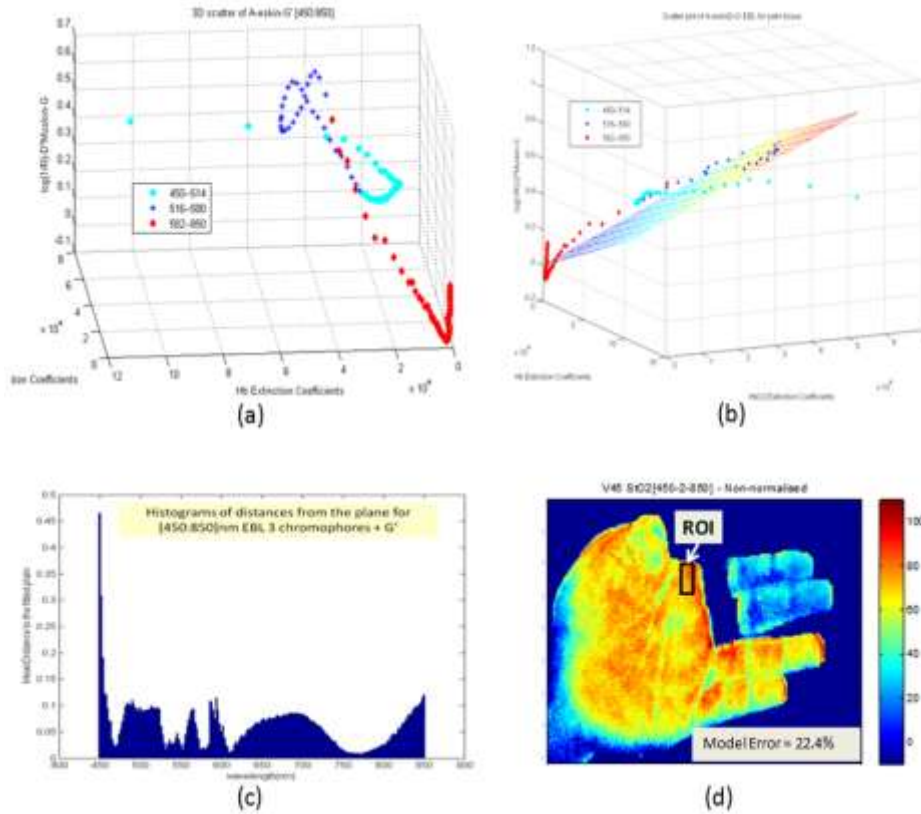


Figure 4-3 shows the effect of using the EBL3C formulation (Equation 4-7) for the StO<sub>2</sub> analysis: (a) 3D scatter plot of the tissue absorbance A after removing the melanin and specular reflection terms, (b) the solution plane (in colour) for the EBL3C (c) the Euclidean distance of all data points to the solution plane, (d) the StO<sub>2</sub> of the palm and ischemia finger using the  $C_{eff}$  as deduced by EBL3C formulation. The model error of the ROI is very large approaching to ~22%.

The result in Figure 4-3 thus suggests that it is not possible to deduce the  $C_{eff}$  of haemoglobin in a sensible way if the diffuse reflectance data of the whole spectra spanning from 450nm to 850nm wavelengths is used for the analysis. This result combined with more data to be presented in section 4.5.2 , thus explains why some authors, notably the work performed by Zuzak et al [55] and Cancio et al[41], who utilised only small subsets of wavelength regions typically 520nm to 645nm for their StO2 analysis.

#### **4.5.2 Wavelength Selection: Subset Spectra**

Based upon the observations from Figure 4-2 & Figure 4-3, it is intuitive to carry out the StO2 assessment using subsets of the spectra rather than to employ all wavelengths in the pixel vector. The StO2 results of the ischemia finger target (see inset of Figure 4-2) under illumination from the top is shown in Figure 4-4. The oxygenation is obtained using different subsets of spectral region as input data and the  $C_{eff}$  is deduced using the EBL3C model (Equation 4-7). The StO2 value of every pixel is presented in colour code, and the spectral region, where the data is used for the analysis, is labelled at the top of each panel in Figure 4-4. The model error (see Equation 4-19) of the ROI1, which is depicted as black rectangle in each panel, is highlighted at the bottom right corner in each case.

It is seen that the model error is the largest when the complete range of the wavelength is used as the input for the StO2 assessment, and it is observed from Figure 4-4(a) & (b) that wavelengths shorter than 510nm as input for the EBL3C model produce erratic result regardless of having reasonable model fitting errors.



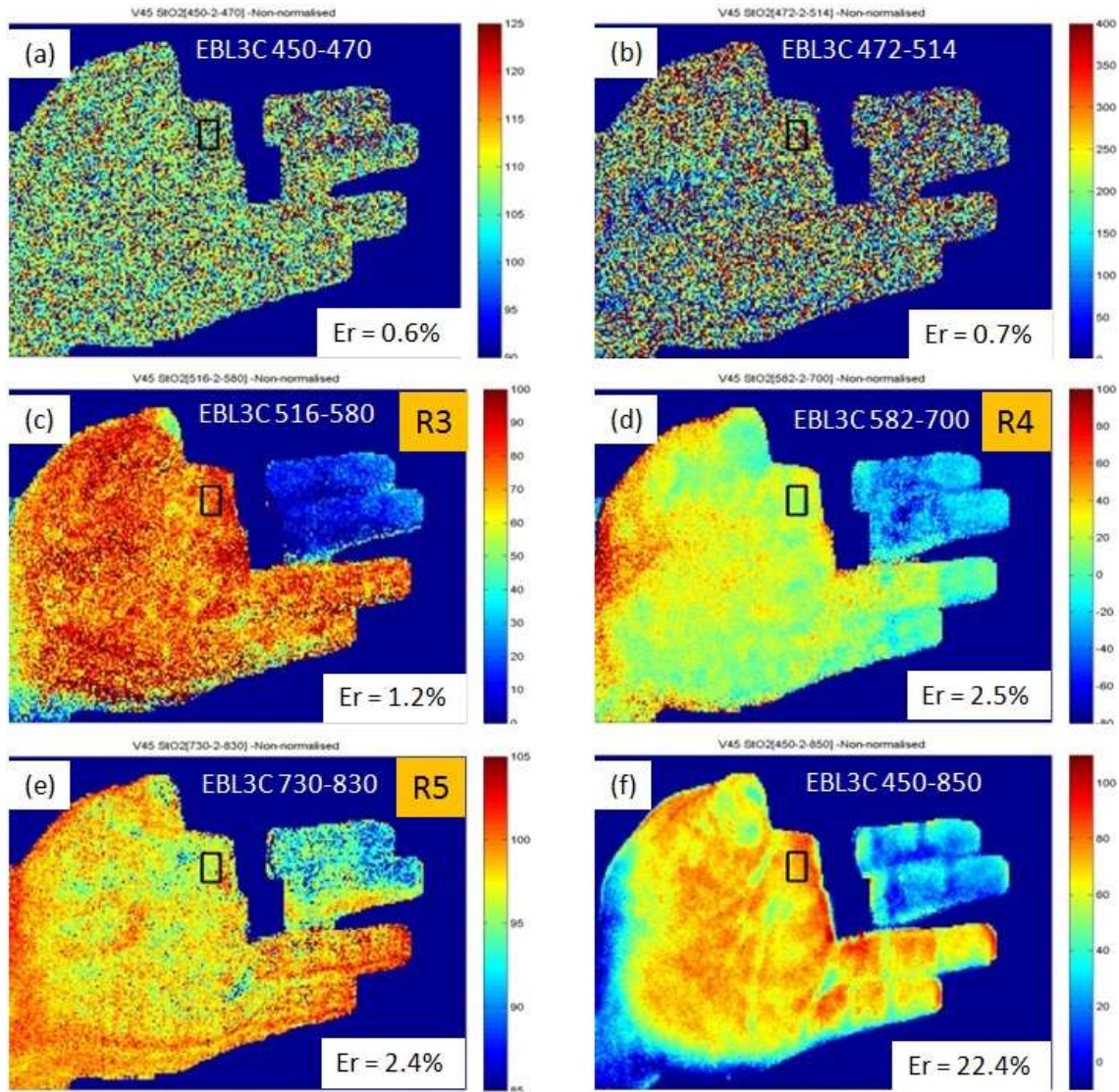
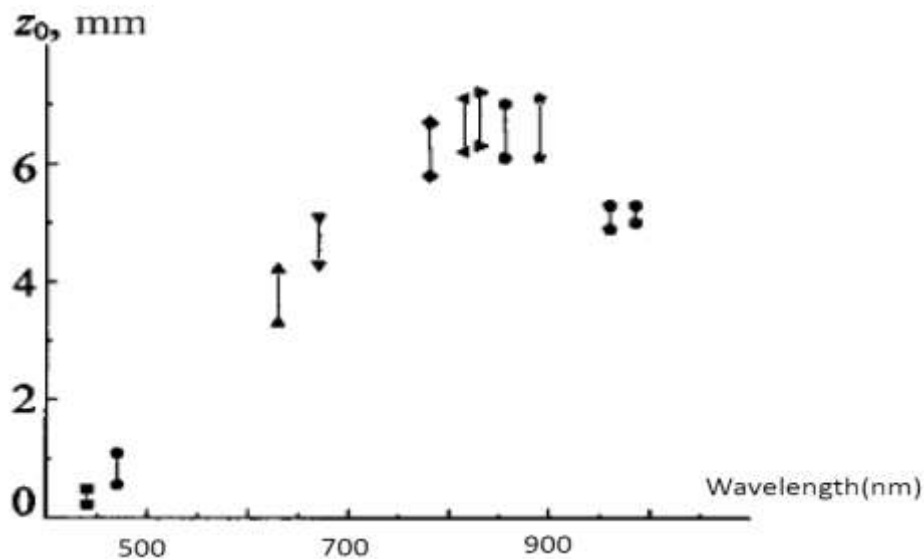


Figure 4-4 shows the StO<sub>2</sub> map of the ischemia finger and palm under illumination from the top. Subsets of spectral regions have been used as inputs under the EBL model(Equation 4-7): (a) 450-470nm, (b) 470-514nm, (c) 516-580nm, (d) 582-700nm, (e) 730-830nm & (f) the whole spectral range of 450-850nm for comparison. It is noted that the model error for assessing the StO<sub>2</sub> of the ROI is the largest in (f).

One possible explanation to this may be due to the limited penetration depth of the wavelengths below 470nm into the body tissue. The light penetration depth of skin as function of wavelength [63] and the typical thicknesses of the epidermis in human body [24] is shown in Figure 4-5 & Table 1 respectively. It is reported that penetration depths of  $\sim 0.3\text{mm}$  to  $\sim 0.9\text{mm}$  has been found for wavelengths at around 450nm and 470nm, while the average thickness of the epidermis in the sole and palm in human is  $\sim 0.6\text{mm}$  [24]. The epidermis layer contains no blood vessels, and only the dermis which lies right beneath the epidermis, consists of connective tissue and capillary network of blood vessels. The relatively shallow penetration depth of the wavelength below 470nm may not be deep enough to reach the dermis layer.



**Figure 4-5 light penetration depth of normal human skin (Caucasian) [63].**

It is noted that the three StO<sub>2</sub> maps obtained from using the three subsets of spectral regions within [516-580]nm, [582-700]nm, and [730-830]nm as input data, are seen to be very different. These three spectral subsets have been labelled respectively as R3, R4 and R5 in Figure 4-4. Although the model errors of these 3 results are relatively small (<3%) comparing with that using all wavelengths (c.f. Figure 4-4(f)), unrealistic oxygenations at the centre part of the palm and also in the ischemia fingers are seen from the StO<sub>2</sub> maps of R4 & R5. For example, the StO<sub>2</sub> at the centre part of the palm given by R4 is about 40% which is ought to be at  $\sim 95\%$ , whilst the oxygenation of the ischemia finger

given by R5 reads ~80% which should be around ~20-30%. Furthermore, it is found that the offset  $G'$  term becomes enormous when the spectral subset of [582-700]nm (i.e.R4) is used for the analysis. The large offset  $G'$  forces the  $\varepsilon C_{eff}$  term becomes non-physically negative, as is depicted in the colour bar of Figure 4-4 (d). One origin of this artefact may stem from the accuracy of the molar absorptivity  $\varepsilon$ : it is seen from Figure 3-6 that the blood absorptions for both Hb and HbO<sub>2</sub> are seen to drop rapidly by ~ a factor of 100 over narrow regions (~30nm) between 580-610nm, any uncertainty in the molar absorptivity within this narrow spectral region will induce significant errors in the StO<sub>2</sub>.

**Table 1 thickness of epidermis and dermis of different part of human body [24]**

Region	Specimens (n)	Epidermis ( $\mu\text{m}$ )	Dermis ( $\mu\text{m}$ )	E + D ( $\mu\text{m}$ )	E/(E + D) (%)
Forehead	14	93.6 $\pm$ 22.3	788.2 $\pm$ 145.6	865.9 $\pm$ 136.8	10.6
Eyelid	28	54.4 $\pm$ 9.6	469.2 $\pm$ 119.7	521.2 $\pm$ 115.8	7.5
Cheek	28	98.2 $\pm$ 26.7	1,076.6 $\pm$ 225.0	1,141.1 $\pm$ 292.3	8.3
Chin	15	84.0 $\pm$ 23.3	763.9 $\pm$ 317.1	857.1 $\pm$ 247.8	9.9
Postauricular r.	18	67.9 $\pm$ 15.1	645.1 $\pm$ 215.3	712.9 $\pm$ 213.1	9.5
Neck (anterior)	14	91.1 $\pm$ 21.8	1,318.2 $\pm$ 364.2	1,408.0 $\pm$ 362.1	6.4
Supraclavicular r.	6	62.9 $\pm$ 16.1	706.8 $\pm$ 211.7	770.0 $\pm$ 220.5	8.1
Axilla	12	70.6 $\pm$ 24.7	940.3 $\pm$ 176.2	1,011.1 $\pm$ 178.1	6.9
Chest	18	98.5 $\pm$ 37.2	1,337.9 $\pm$ 332.3	1,438.5 $\pm$ 319.7	6.8
Abdomen	29	79.4 $\pm$ 33.9	1,248.4 $\pm$ 262.5	1,331.6 $\pm$ 254.2	6.0
Back	23	76.8 $\pm$ 25.9	1,941.6 $\pm$ 321.1	1,976.9 $\pm$ 395.1	3.7
Inguinal r.	19	77.8 $\pm$ 33.5	548.0 $\pm$ 266.2	625.9 $\pm$ 273.4	12.4
Buttock	14	137.7 $\pm$ 54.5	1,585.5 $\pm$ 536.3	1,721.4 $\pm$ 555.1	7.9
Penis	11	31.2 $\pm$ 5.7	514.8 $\pm$ 145.0	546.0 $\pm$ 141.9	5.7
Front of arm	11	69.2 $\pm$ 21.9	943.4 $\pm$ 235.6	1,012.6 $\pm$ 233.3	6.8
Back of arm	14	83.5 $\pm$ 36.2	1,030.4 $\pm$ 327.8	1,171.8 $\pm$ 379.3	7.4
Front of forearm	17	74.1 $\pm$ 25.4	1,020.4 $\pm$ 208.5	1,133.1 $\pm$ 214.7	6.7
Back of forearm	8	102.1 $\pm$ 34.0	1,077.4 $\pm$ 161.5	1,182.0 $\pm$ 165.0	8.7
Dorsum of hand	12	189.2 $\pm$ 63.1	932.9 $\pm$ 121.9	1,065.0 $\pm$ 130.4	16.8
Palm	11	600.9 $\pm$ 96.8	745.6 $\pm$ 163.5	1,349.4 $\pm$ 189.5	44.6
Front of thigh	17	87.4 $\pm$ 27.7	1,058.1 $\pm$ 147.6	1,144.0 $\pm$ 156.2	8.2
Lateral thigh	18	94.8 $\pm$ 23.6	1,217.6 $\pm$ 318.3	1,331.9 $\pm$ 333.5	7.2
Back of thigh	14	102.3 $\pm$ 48.6	1,006.5 $\pm$ 219.7	1,118.5 $\pm$ 178.1	9.2
Anterior leg	20	91.2 $\pm$ 25.8	921.5 $\pm$ 194.3	1,016.0 $\pm$ 219.8	9.0
Lateral leg	22	109.2 $\pm$ 18.3	1,013.4 $\pm$ 307.2	1,122.8 $\pm$ 208.4	9.7
Back of leg	15	129.6 $\pm$ 44.1	981.6 $\pm$ 148.2	1,052.4 $\pm$ 261.3	11.6
Dorsum of foot	13	163.1 $\pm$ 18.6	1,001.1 $\pm$ 259.2	1,164.4 $\pm$ 280.9	14.0
Sole	11	637.1 $\pm$ 186.0	931.9 $\pm$ 411.2	1,569.0 $\pm$ 582.7	40.6



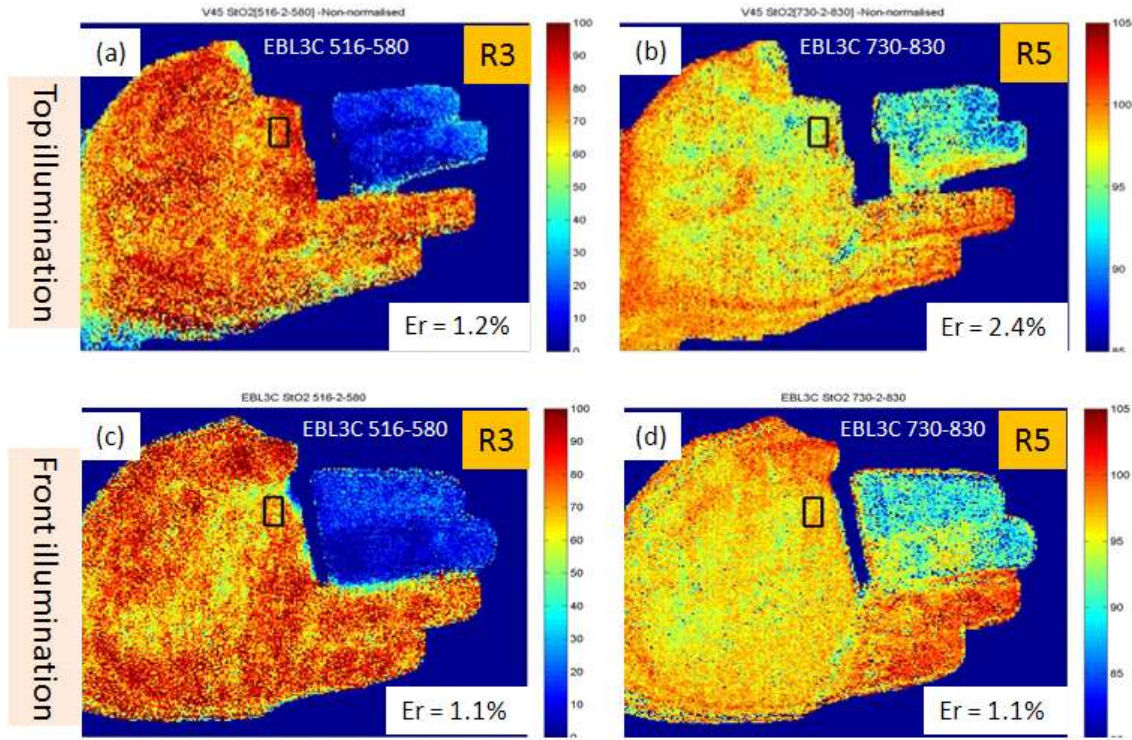


Figure 4-6 shows the StO<sub>2</sub> maps of the ischemia finger and palm of the same subject but under different illuminations conditions of: from the top (top panel) and from the front (bottom panel). Two subsets of spectral regions in the visible (left hand column) and near infra red (right hand column) data have been used as inputs for the StO<sub>2</sub> assessment under the EBL3C model (Equation 4-7). The StO<sub>2</sub> values are presented in false colour images.

#### 4.5.3 Visible VS Near Infra-red Spectral Region

One motive of this work is to study the methodology to improve the robustness of StO<sub>2</sub> assessment through the selection of spectral subsets from the visible (VIS) and near infrared (NIR) regions. According to the results in Figure 4-4, it is suggested that the two spectral regions of [516-580]nm (i.e. the visible region R3) and [730-830]nm (i.e. the NIR region R5 in Figure 4-4), may be promising candidates which can improve the robustness of StO<sub>2</sub> assessment.

The StO<sub>2</sub> images of the ischemia finger and the palm of the same subject but under two different illumination conditions of (a) from the top and (b) from the front of the palm, are shown in Figure 4-6. The results are obtained by using two subsets of R3 ([516-580]nm) and R5 ([730-830]nm) spectral data as inputs

under the EBL3C model (Equation 4-7). The model errors in all cases are small (<3%), and it is seen that the StO<sub>2</sub> (see Figure 4-6(a)&(c)) for using the R3 subset of spectral data produces a much more realistic and reproducible StO<sub>2</sub> values over the palm and fingers independent of illumination conditions, than that of the oxygenation map obtained from the NIR region R5 (Figure 4-6(b) & (d)). The StO<sub>2</sub> of the ischemia fingers in the NIR data (Figure 4-6(b) & (d)) exhibits unrealistic values of around 85-90%, in great contrast to that using R3 subset of data which consistently gives 20-30% of oxygenation (see Figure 4-6(a) & (c)).

While there is a great advantage for using NIR wavelength of light to probe greater depths of the dermis layer, the molar absorptivity of blood in this region is about 100 times weaker than that in the visible region (see Figure 3-6). The greater of the penetration depth implies a larger degree of tissue scattering, and simple models like that of the EBL will not be sufficient enough to account for the very small ratio of the blood absorptivity/tissue scattering ( $\epsilon_{blood}/\epsilon_{scattering}$ ) [7][64] and more sophisticated models, such as the diffusion theory based [49] and Monte Carlo [45] method will be needed.

#### **4.5.4 BL Model VS EBL Model: Reproducibility and Model Error**

The objective of this section is to testify the accuracies of the BL2C, BL3C, EBL2C and the EBL3C models for the assessment of StO<sub>2</sub> particularly when data is collected by using image based non-contact method like that in the HSI remote sensing. The StO<sub>2</sub> maps that are produced by these four models using data collected under two illumination conditions are compared here. The model errors of two ROIs selected from the high & low StO<sub>2</sub> regions from the palm and ischemia finger regions have been chosen respectively. The fitness of each model for these data sets is presented together with the error assessment in this section.

The left and right columns in Figure 4-7 and Figure 4-8 are StO<sub>2</sub> maps for the top and front illuminated data respectively, and they are produced by BL2C using various subsets of spectral ranges. The StO<sub>2</sub> maps using input data of

[450-470]nm, [472-514]nm, [516-580]nm ranges are shown in Figure 4-7, and the StO<sub>2</sub> maps using data from [582-700]nm, [730-830]nm, [450-850]nm ranges are shown in Figure 4-8. Figure 4-9 and Figure 4-10 are the StO<sub>2</sub> maps produced by BL3C, while Figure 4-11 and Figure 4-12 are the results of EBL2C, and Figure 4-13, Figure 4-14 are the results of EBL3C. It is seen from Figure 4-7, Figure 4-8, Figure 4-9, Figure 4-10, Figure 4-11, and Figure 4-12 that reproducible StO<sub>2</sub> maps cannot be obtained under the BL2C, BL3C, or EBL2C models, e.g. BL2C model (Figure 4-7, Figure 4-8), the StO<sub>2</sub> on the top part of fingers are generally higher than the bottom part, particularly in longer wavelength, under top illumination conditions. However, this top-bottom uneven StO<sub>2</sub> distribution is not seen in the front illumination condition.

It is also seen that the StO<sub>2</sub> maps for all models using the wavelength range of [516-580]nm range produce the best consistent results between the two data sets of top and front illumination (see Figure 4-7, Figure 4-9, Figure 4-11, Figure 4-13 (e) & (f)). However, it is seen that the StO<sub>2</sub> scaling is different for the results obtained under BL2C, BL3C, and EBL2C, e.g. in the BL3C the minimum and maximum StO<sub>2</sub> values are seen in the range of [0 80] for the top illumination data (Figure 4-9 (e)), and it becomes [0 70] in the front illumination data set for the same target (Figure 4-9 (f)).

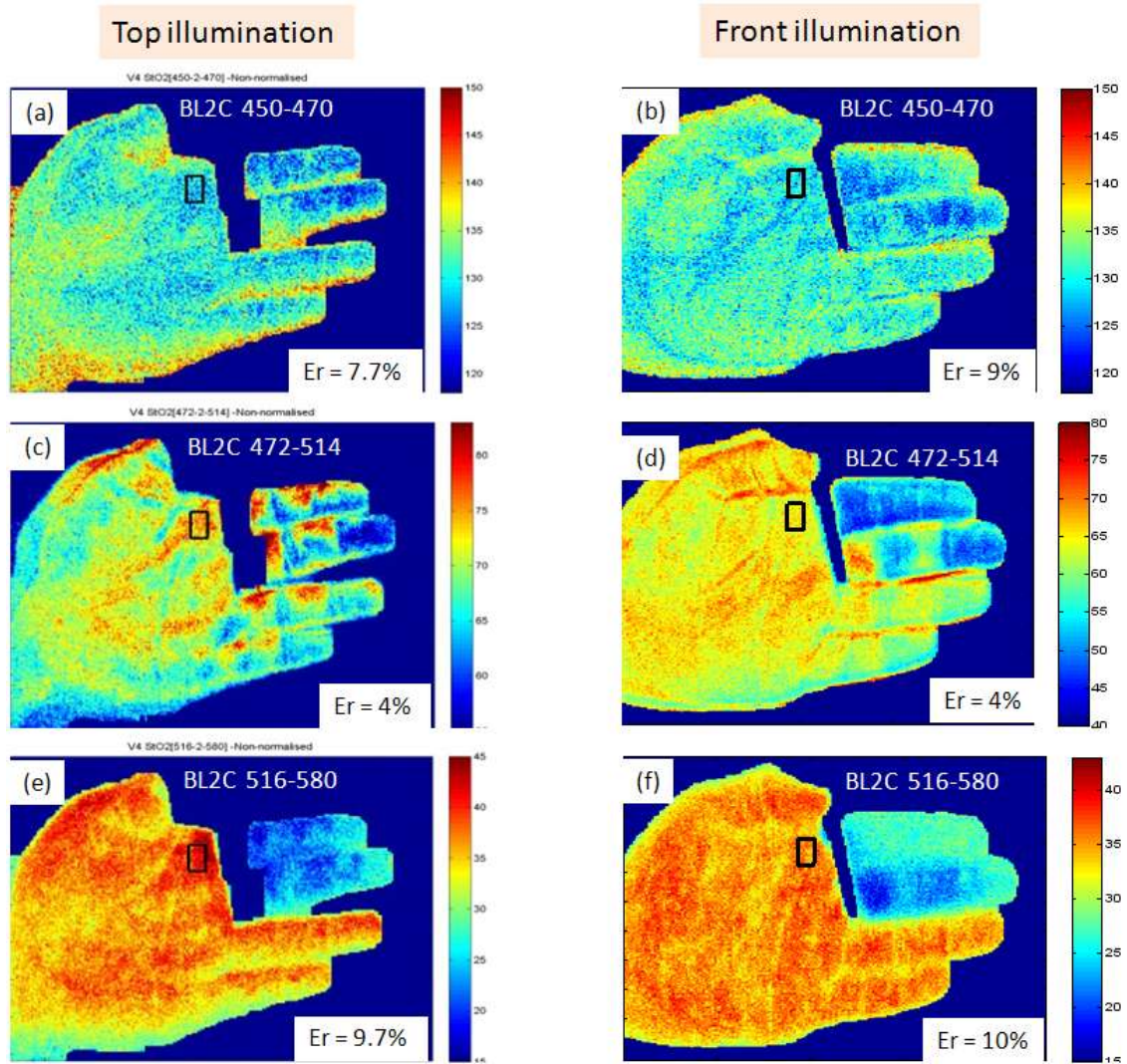


Figure 4-7 shows StO2 map produced by BL2C under top (left column) and front (right column) illumination using the subset spectral ranges of [450:470], [472:514], [516:580] as input data.



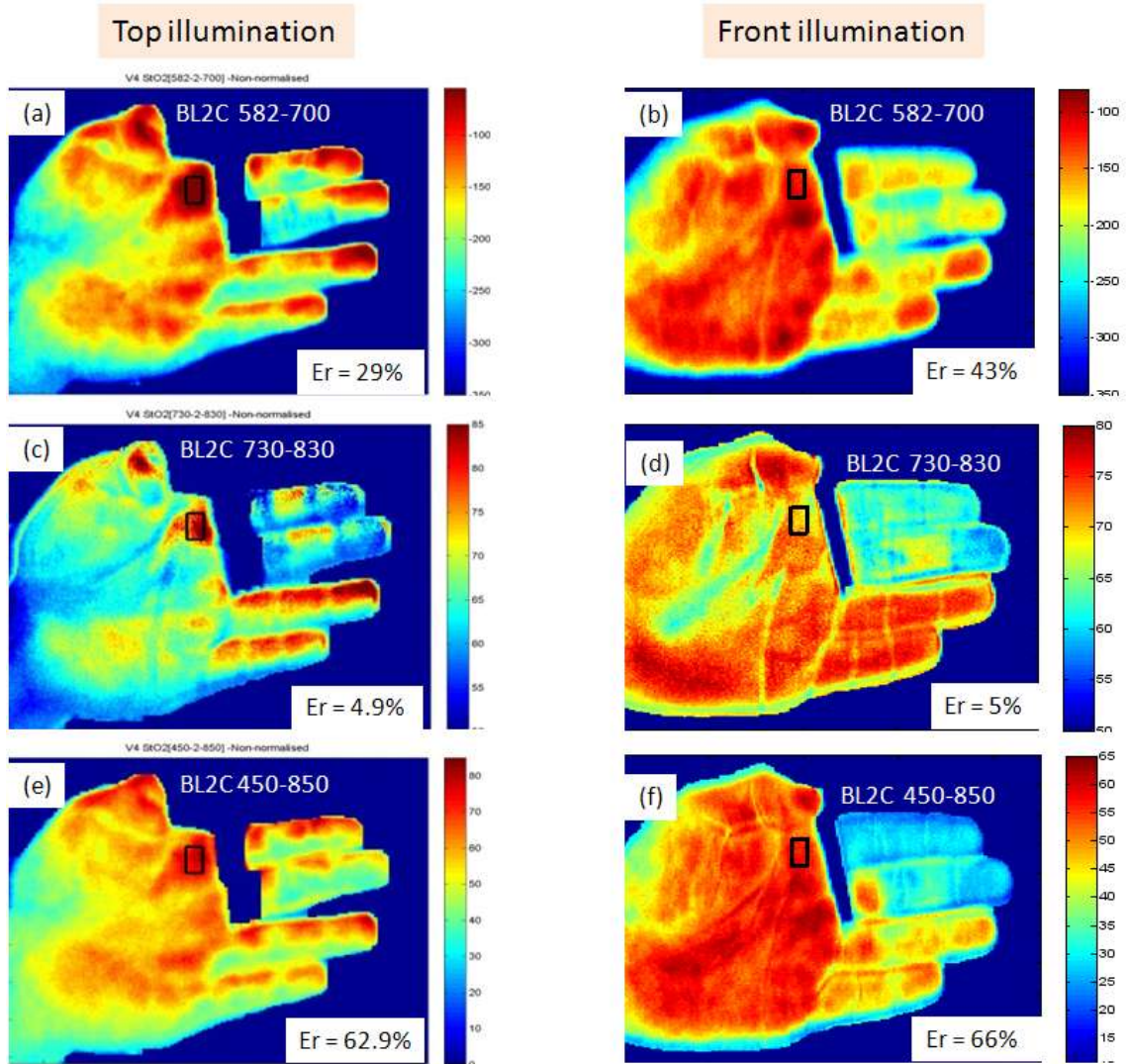


Figure 4-8 shows StO2 map produced by BL2C under top (left column) and front (right column) illumination using the subset spectral ranges of [582:700], [730:830], [450:850] as input data.

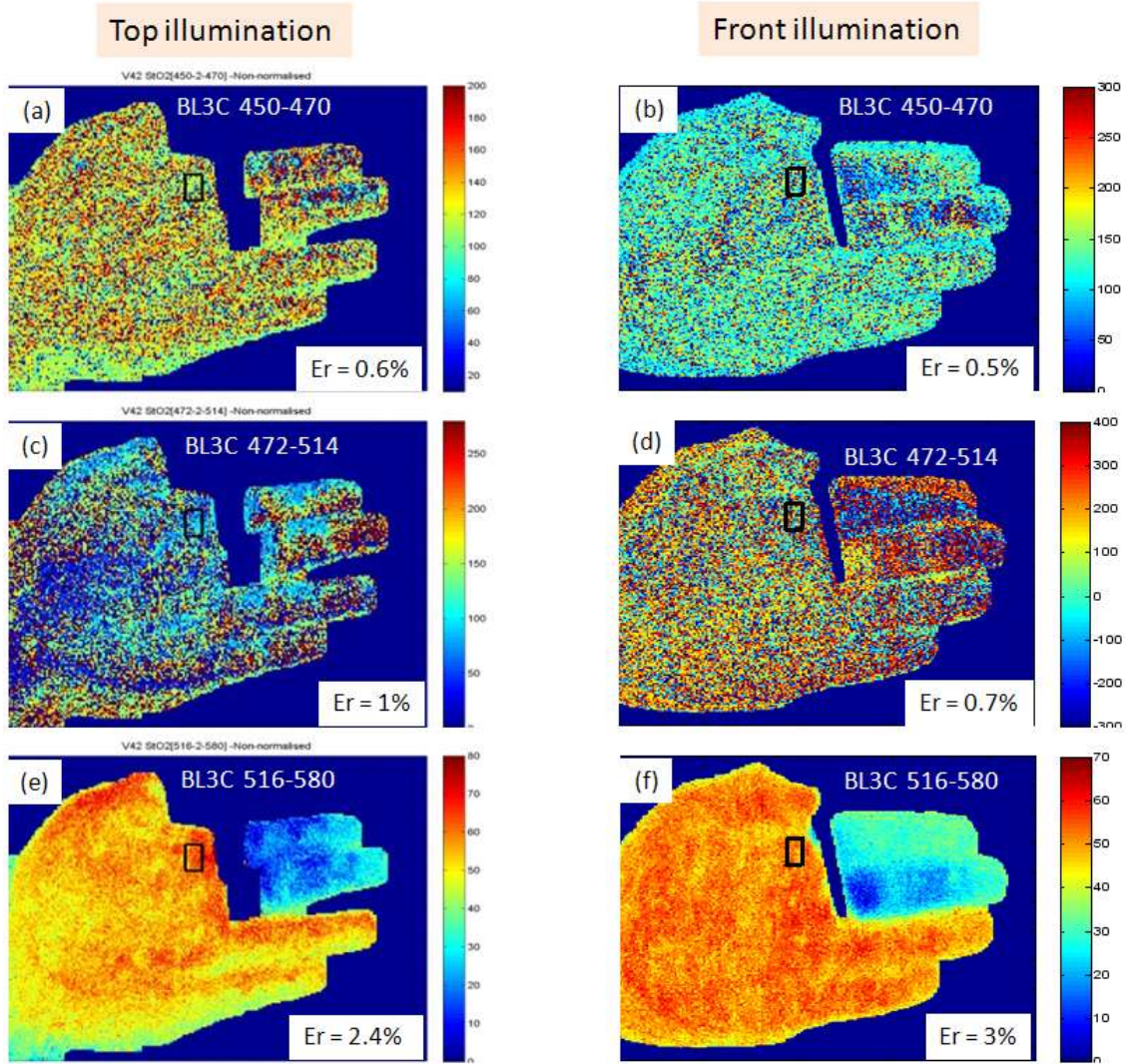


Figure 4-9 shows StO<sub>2</sub> map produced by BL3C under top (left column) and front (right column) illumination using the subset spectral ranges of [450:470], [472:514], [516:580] as input data.



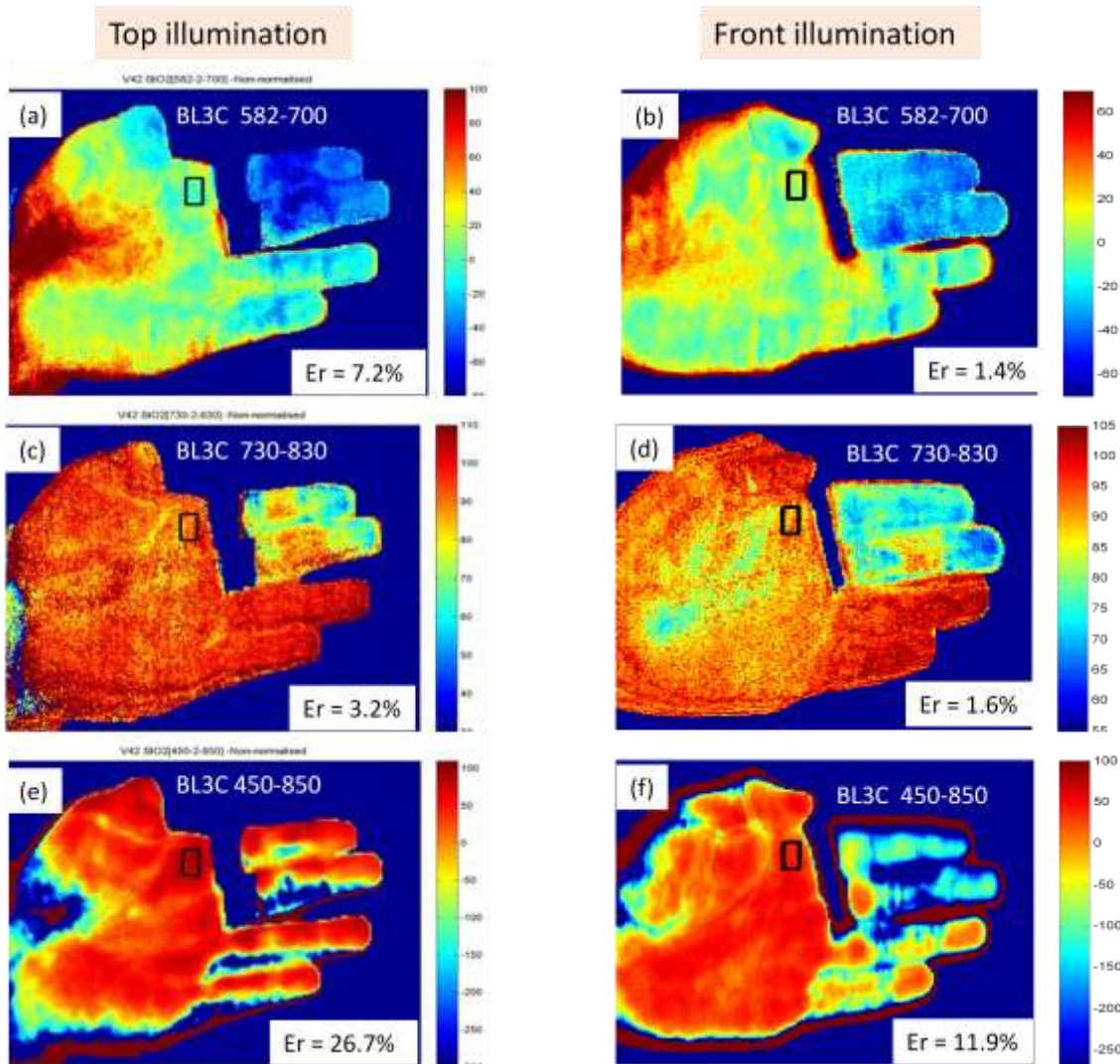


Figure 4-10 shows StO2 map produced by BL3C under top (left column) and front (right column) illumination using the subset spectral ranges of [582:700], [730:830], [450:850] as input data.

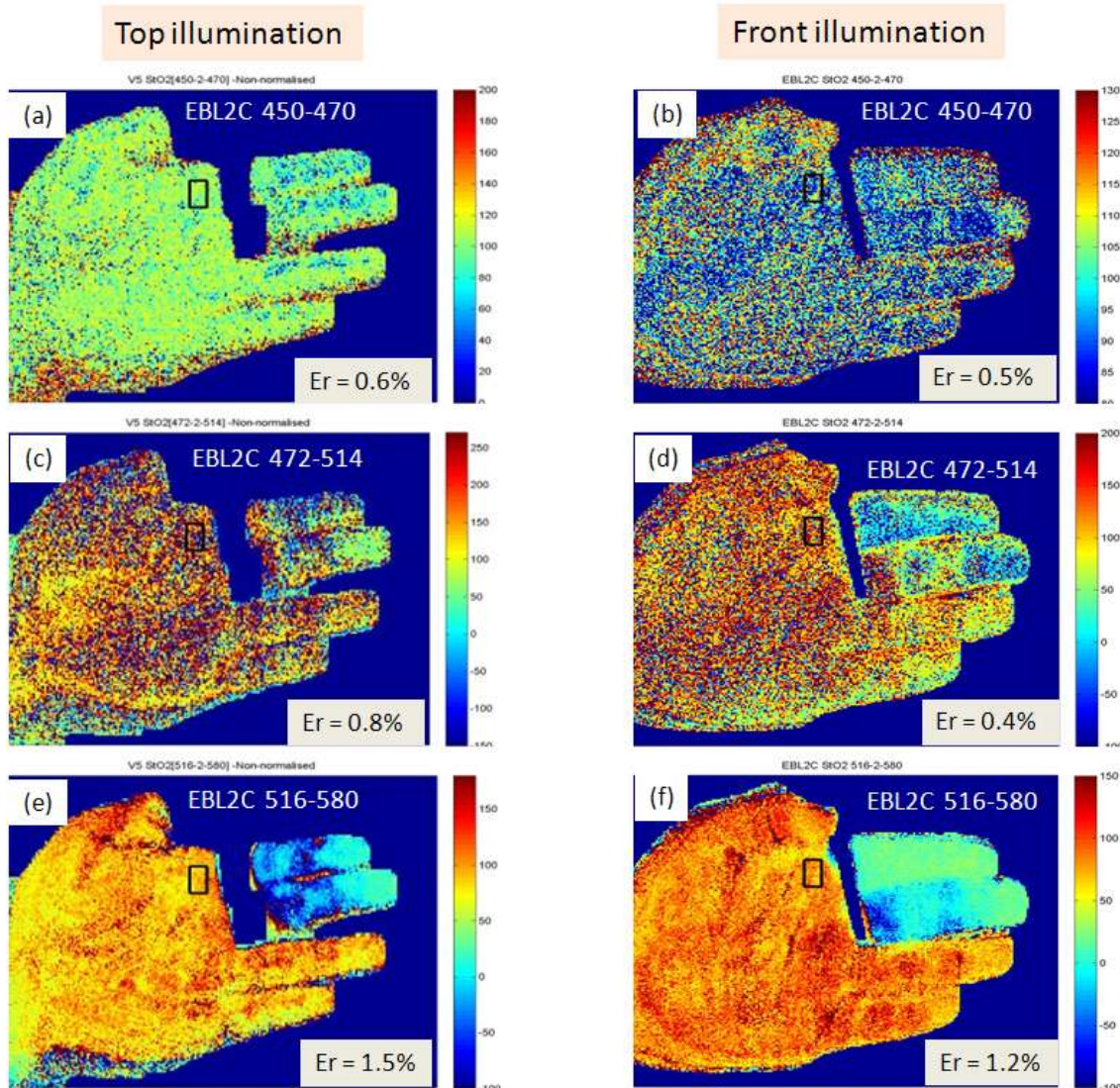


Figure 4-11 shows StO2 map produced by EBL2C under top (left column) and front (right column) illumination using the subset spectral ranges of [450:470], [472:514], [516:580] as input data.



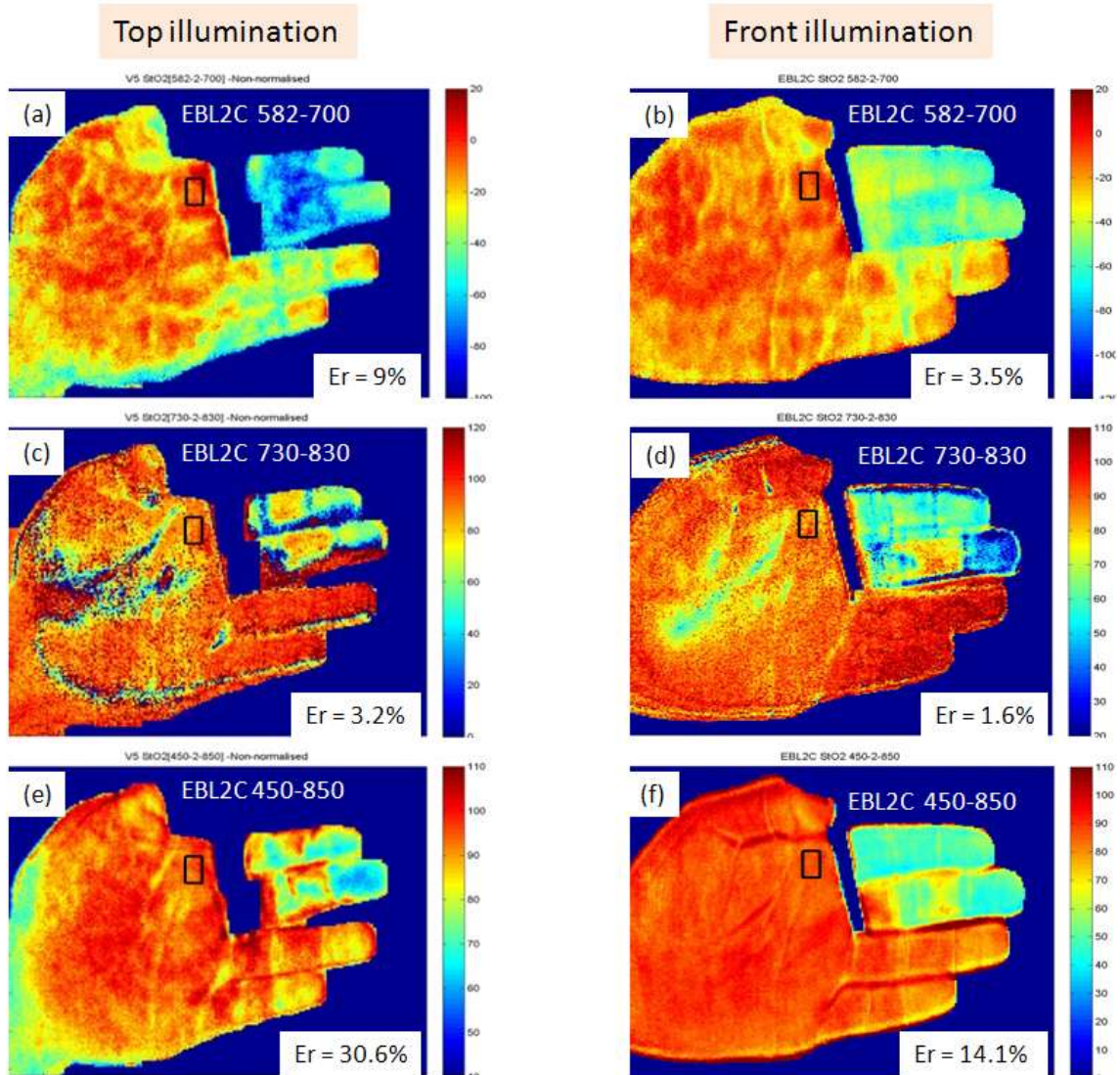


Figure 4-12 shows StO<sub>2</sub> map produced by EBL2C under top (left column) and front (right column) illumination using the subset spectral ranges of [582:700], [730:830], [450:850] as input data.

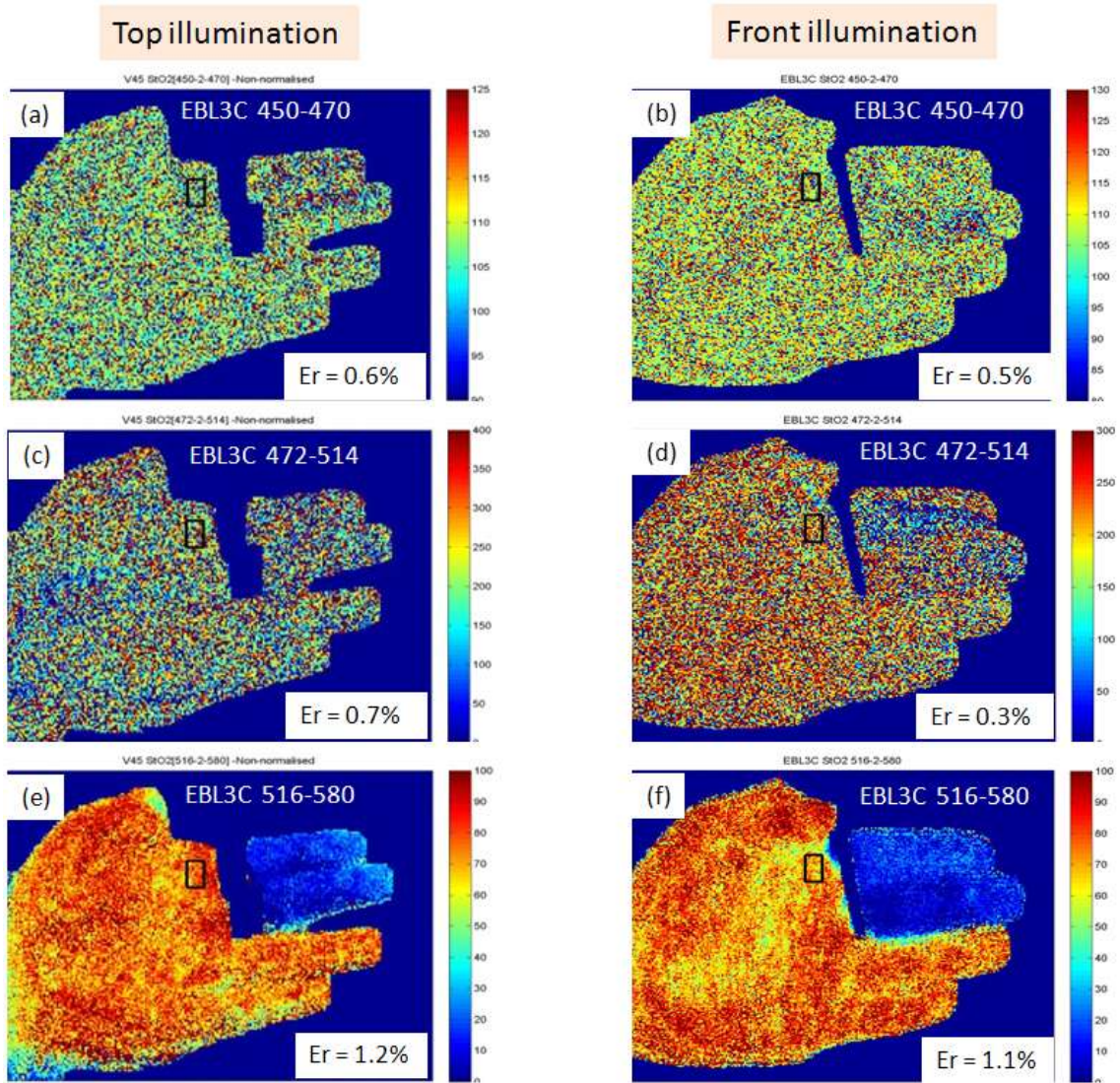
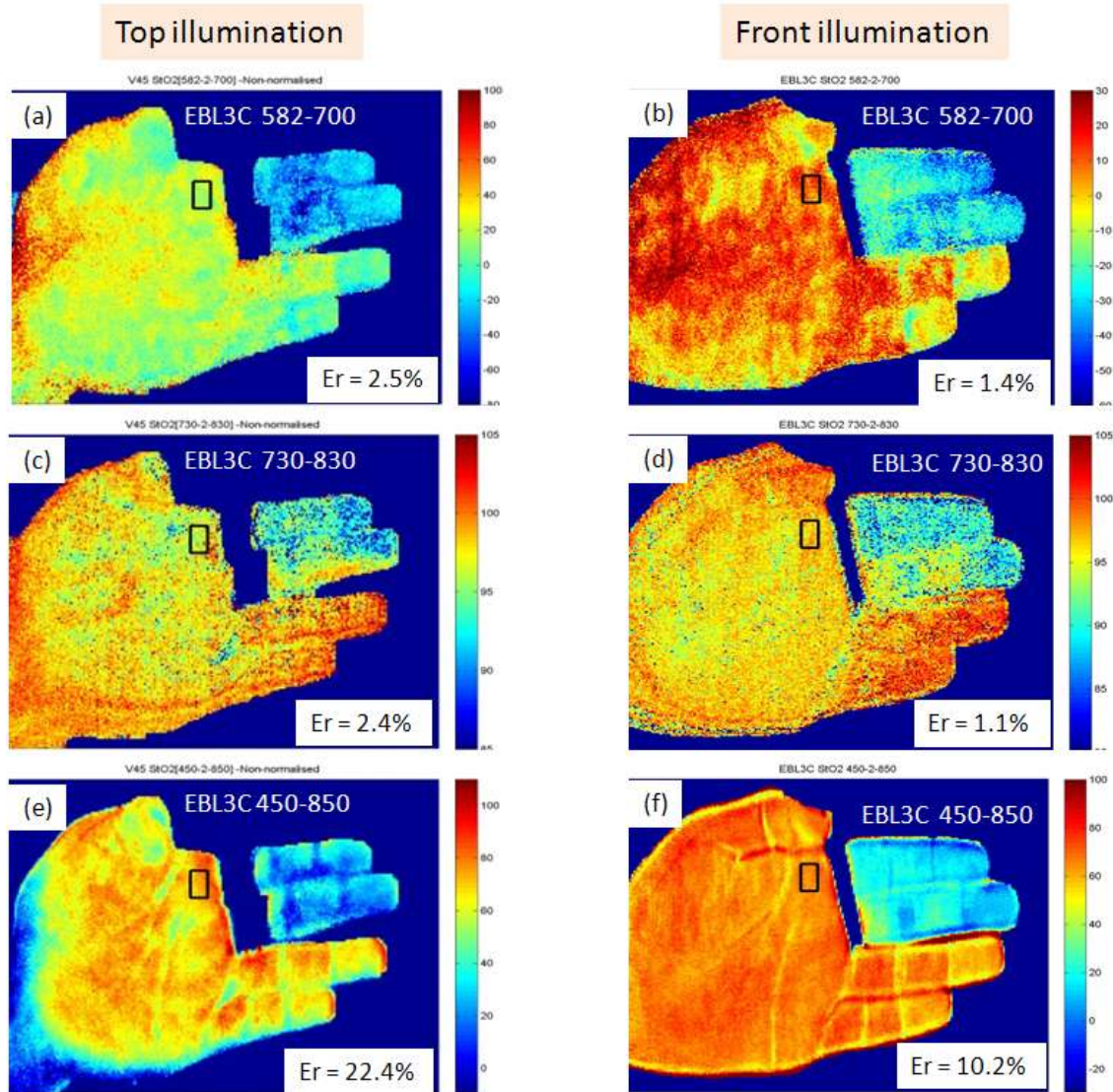


Figure 4-13 shows StO2 map produced by EBL3C under top (left column) and front (right column) illumination using the subset spectral ranges of [450:470], [472:514], [516:580] as input data.





**Figure 4-14 shows StO2 map produced by EBL3C under top (left column) and front (right column) illumination using the subset spectral ranges of [582:700], [730:830], [450:850] as input data.**

The Model errors that have been evaluated according to Equation 4-19 for the three ROIs in the palm (see Figure 4-2) under top illumination conditions are summarised in Table 2 and Table 3. It is observed that the BL3C and EBL2C have smaller model errors than those of BL2C, and that the EBL3C has the smallest model errors among the four models regardless of the ROI. Table 4 shows the model errors of the palm ROI1 under top and front illumination conditions. It is seen that the model errors of BL3C and EBL2C are smaller than those of BL2C, and the model errors of EBL3C are almost smallest in all

illumination conditions. These indicate that the extended BL model is more suitable than the basic BL one, and that the three-chromophore model is more appropriate than the two-chromophore models in terms of minimising the fitting errors.

**Table 2 model errors of palm ROIs of StO<sub>2</sub> map using various wavelength regions ([450 470]nm, [472 514]nm, [516 580]nm) of data and different BL models under top illumination condition.**

	Wavelength(nm)								
	450:470			472:514			516:580		
Method	ROI1	ROI2	ROI3	ROI1	ROI2	ROI3	ROI1	ROI2	ROI3
<b>BL2C</b>	5.88%	8.34%	8.08%	3.98%	3.83%	4.02%	9.72%	10.79%	10.85%
<b>BL3C</b>	1.34%	0.94%	0.74%	1.00%	1.01%	0.80%	2.44%	2.78%	2.52%
<b>EBL2C</b>	1.36%	1.01%	0.79%	0.81%	0.98%	0.69%	1.47%	1.37%	1.50%
<b>EBL3C</b>	1.31%	0.92%	0.74%	0.73%	0.97%	0.69%	1.27%	1.02%	0.94%

**Table 3 model errors of palm ROIs of StO<sub>2</sub> map using various wavelength regions ([582 700]nm, [730 830]nm, [450 850]nm)of data and different BL models under top illumination condition.**

	Wavelength(nm)								
	582:700			730:830			450:850		
Method	ROI1	ROI2	ROI3	ROI1	ROI2	ROI3	ROI1	ROI2	ROI3
<b>BL2C</b>	28.96%	48.21%	43.18%	4.85%	5.97%	5.45%	62.89%	67.87%	67.20%
<b>BL3C</b>	7.18%	1.00%	2.20%	3.15%	1.35%	1.84%	26.66%	7.66%	9.37%
<b>EBL2C</b>	9.04%	3.21%	5.23%	3.20%	1.47%	1.93%	30.60%	12.29%	17.13%
<b>EBL3C</b>	2.53%	0.74%	1.32%	2.41%	0.97%	1.30%	22.40%	4.84%	9.35%

The accuracies of the four BL models for assessing low value of oxygenations such as that in the ischemia fingers, have been evaluated here using the same formulation as that of the palm data set presented in the previous paragraphs (Equation 4-19). The finger ROI is denoted as black rectangular area in Figure 4-15. It is seen from Table 5 that the result of the EBL3C model outperforms the other three models with almost the lowest errors.

It is also noticed from Table 4 and Table 5 that the StO<sub>2</sub> is seen better assessed in terms of better fitting (smaller errors) by using subsets of spectral data than that using the complete spectral data set. It is found that the best result can be obtained using the wavelength range of [516-580]nm achieving small error less than ~2.5% under the EBL3C model.

**Table 4 model errors of palm ROI1 of StO<sub>2</sub> map using various wavelength regions of data and different BL models under top and front illumination conditions**

Model	Wavelength(nm)											
	450:470		472:514		516:580		582:700		730:830		450:850	
	Top illu	Front illu	Top illu	Front illu	Top illu	Front illu	Top illu	Front illu	Top illu	Front illu	Top illu	Front illu
BL2C	7.71%	8.96%	3.98%	3.99%	9.72%	10.42%	28.96%	42.87%	4.85%	5.16%	62.89%	66.37%
BL3C	0.56%	0.49%	1.00%	0.68%	2.44%	2.98%	7.18%	1.41%	3.15%	1.56%	26.66%	11.85%
EBL2C	0.58%	0.51%	0.81%	0.42%	1.47%	1.19%	9.04%	3.49%	3.20%	1.64%	30.60%	14.06%
EBL3C	0.58%	0.49%	0.73%	0.32%	1.27%	1.09%	2.53%	1.42%	2.41%	1.11%	22.40%	10.20%

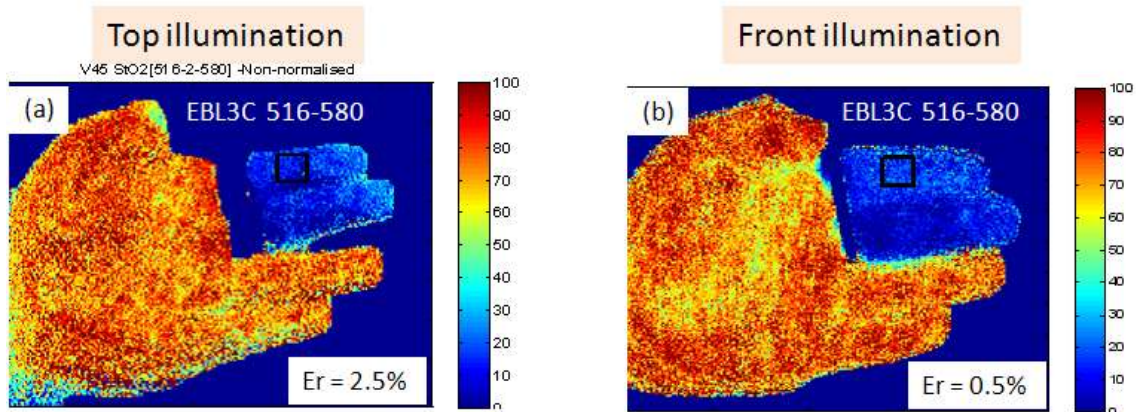


Figure 4-15 shows the finger ROIs (black square) for assessing the model errors of StO<sub>2</sub> accuracies as presented in Table 5.

**Table 5 model errors of finger ROI of StO<sub>2</sub> map using various wavelength regions of data and different BL models under top and front illumination conditions**

	Wavelength(nm)											
	450:470		472:514		516:580		582:700		730:830		450:850	
Method	Top Illu	Front Illu	Top illu	Front Illu	Top Illu	Front Illu	Top Illu	Front Illu	Top Illu	Front Illu	Top Illu	Front Illu
<b>BL2C</b>	8.85%	8.49%	4.41%	3.97%	11.58%	9.15%	42.67%	45.07%	6.32%	5.06%	68.35%	66.14%
<b>BL3C</b>	1.88%	0.94%	1.98%	0.71%	2.52%	3.23%	5.90%	1.44%	3.76%	1.34%	9.77%	11.46%
<b>EBL2C</b>	1.88%	0.94%	1.98%	0.59%	3.42%	0.53%	8.86%	3.63%	3.79%	1.41%	21.34%	11.57%
<b>EBL3C</b>	1.88%	0.94%	1.98%	0.59%	2.49%	0.47%	3.50%	1.44%	3.68%	1.17%	10.24%	7.61%

## 4.6 Conclusion

This chapter investigates the effectiveness of wavelength and model selections for improving the robustness of tissue oxygenation assessments, especially when the non-contact image based data like that of the hyperspectral image is used for the analysis. One purpose of the present work is to provide a set of real data to elucidate why some subsets of spectral data is more suitable for oxygenation assessments than others. This question has been raised in the community for some time but it remains unanswered, partly due to the commercial interest of this technology within the biomedical sector. Different authors in the field have adopted different range of specific wavelengths: some have chosen visible region (VIS) around 550-600nm region while others prefer to use near infra-red (NIR) wavelengths around 600-1050nm. There is also numerous works in the area using various forms of Beer-Lambert (BL) formulations for the StO<sub>2</sub> assessment, and it is not clear whether the basic BL formulation or the extended version would be more appropriate. We address these issues and to provide the result to clarify why some wavelengths are more suitable than others for the tissue StO<sub>2</sub> assessment.

It is shown that for simple target like that of the palm, the extended version of the Beer-Lambert model can only just applicable for the tissue StO<sub>2</sub> assessment within a small subset of spectral region between 516-580nm. No

StO<sub>2</sub> information could be obtained when wavelengths shorter than 470nm are used, presumably due to the limited penetration depths of these wavelengths within the palm tissue. StO<sub>2</sub> assessment using wavelengths between 580nm and 610nm requires highly accurate molar absorptivity of Hb and HbO<sub>2</sub>, and the Beer Lambert model is not adequate enough to account for the substantial scattering within the tissue for the near infrared spectrum in the 730-830nm region.

It is also shown in this work that the extended Beer Lambert model is more suitable than the basic one, and that the three-chromophore model is more appropriate for remote sensing of StO<sub>2</sub> than the model using two-chromophore as far as minimising of fitting error concern. The EBL3C has been found to be the most suitable model for the assessment of tissue oxygen saturation particularly when the data are collected by non-contact image based hyperspectral method.





## **5 IMPROVE TISSUE OXYGEN SATURATION ASSESSMENT BY USING BODY REFLECTANCE**

### **5.1 Motive of Research**

Most of the previous work [6][9][55][10][8][65] have commonly interpreted the absorbance of tissue using the logarithmic inverse of the apparent reflection from the tissue, which includes the surface specular (interface) reflection as well as the body tissue's diffusive reflection. The skin's specular reflectance is defined as the ratio of specular reflected light intensity from skin surface to the total incident light intensity. As the specular reflection of light from the skin surface gives no information about the skin nor the dermis layer, this part of the reflection should be excluded from the StO<sub>2</sub> assessment. This specular information has been estimated through the  $G'$  term in the BL models (Equation 4-7) presented in the previous chapters. However, the constant wavelength independent  $G'$  term that has been implemented previously is not adequate: for some wavelength ranges such as between [582-700]nm, the  $G'$  is so large that the resulting StO<sub>2</sub> level becomes un-physically negative. This chapter is devoted to the estimation of this specular reflection due to the skin surface and to improve the StO<sub>2</sub> assessment.

### **5.2 Specular Reflectance and Body Reflectance [66]**

The human skin tissue can be modelled as an opaque medium with infinite thickness (see Figure 5-1) in the visible to near infrared region, which implies that all photons that are directed to the skin either experiences specular (interface) reflection or penetrates into the dermis layer without travelling through the tissue. The light that enters into the tissue is either completely absorbed by chromophores (HbO<sub>2</sub>, Hb, and melanin) there, or is partially absorbed and partially scattered out of the skin tissue as the contribution to the body reflection. Figure 5-1 illustrates these two kinds of reflections from the human skin. It is seen that the light from interface reflection interacts with no chromophores and thus carries no StO<sub>2</sub> information. The amount of the specular reflection is defined by Fresnel's laws through the relationship between

the incidence angle, the refractive index of the skin tissue and the polarizing state of the incident light. The refractive index of human tissue is normally taken as 1.4 [23] in the visible to near infrared region, and the specular reflection is commonly assumed to be 5% in this wavelength region [7]. This is the conventional concept for assuming a wavelength independent specular reflection due to the skin, which is implemented in the previous EBL3C formulation (Equation 4-7). In fact the refractive index of skin is wavelength-dependent [22] and so is the specular reflection. It is noted from the previous chapters that the net effect of the constant  $G'$  term is the shift of the overall StO<sub>2</sub> scale. In this chapter the specular reflection of the skin surface is estimated and it is then subsequently removed for the StO<sub>2</sub> assessment.

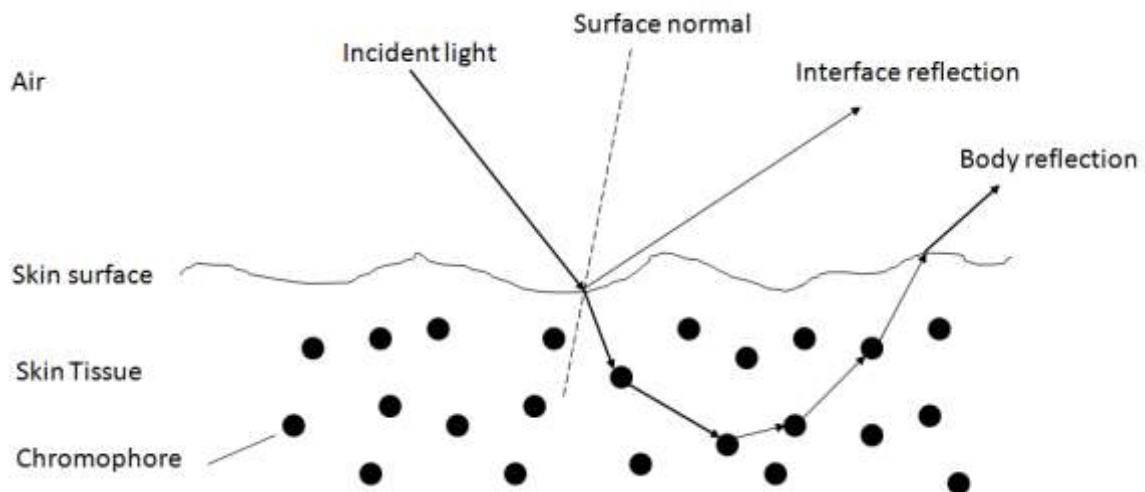


**Figure 5-1 shows the interface (specular) reflection, body reflection of skin. Incident light is partly reflected as interface reflection, partly absorbed by tissue chromophores, and partly reflected as body reflection.**

## **5.3 Specular Reflection Measurement of Human Skin**

### **5.3.1 Polarisation and Reflection**

The separation between the specular and body reflections from skin tissue can be achieved using polarisation techniques. As the result of multiple scatterings within the body tissues, the polarisation state of the body reflected beams tends to be more unpolarised, than that of specularly reflected beam from the skin surface. This change of the polarisation state due to multiple scattering can easily be detected, particularly when the incident beam is polarised, for example through a polariser. Then the reflection due to the body tissue can be selected and subsequently detected through a crossed polariser placed at the front of the HSI sensor, which thereby rejects most of the specular reflected beam from the skin surface.

### **5.3.2 Experiment Settings**

Two polarisers, shown in Figure 5-2, have been employed for the measurement of the specular reflected beam due to the skin surface. The polariser A (PLA) is placed in front of a halogen lamp as shown in Figure 5-2 (a). The halogen lamp is equipped with a diffuser same as the one used in Figure 4-1 (a). This illumination setting produces a diffusive and polarised irradiance to the target object. Polariser B (PLB) is firstly set in front of the PLA (see Figure 5-2 (b) & (c)) such that the PLB is adjusted to cross polarise with respect to PLA as shown in Figure 5-2 (c). Then PLA and PLB are repositioned to the front of the light source and the detector respectively as shown in Figure 5-2 (d) & (e).

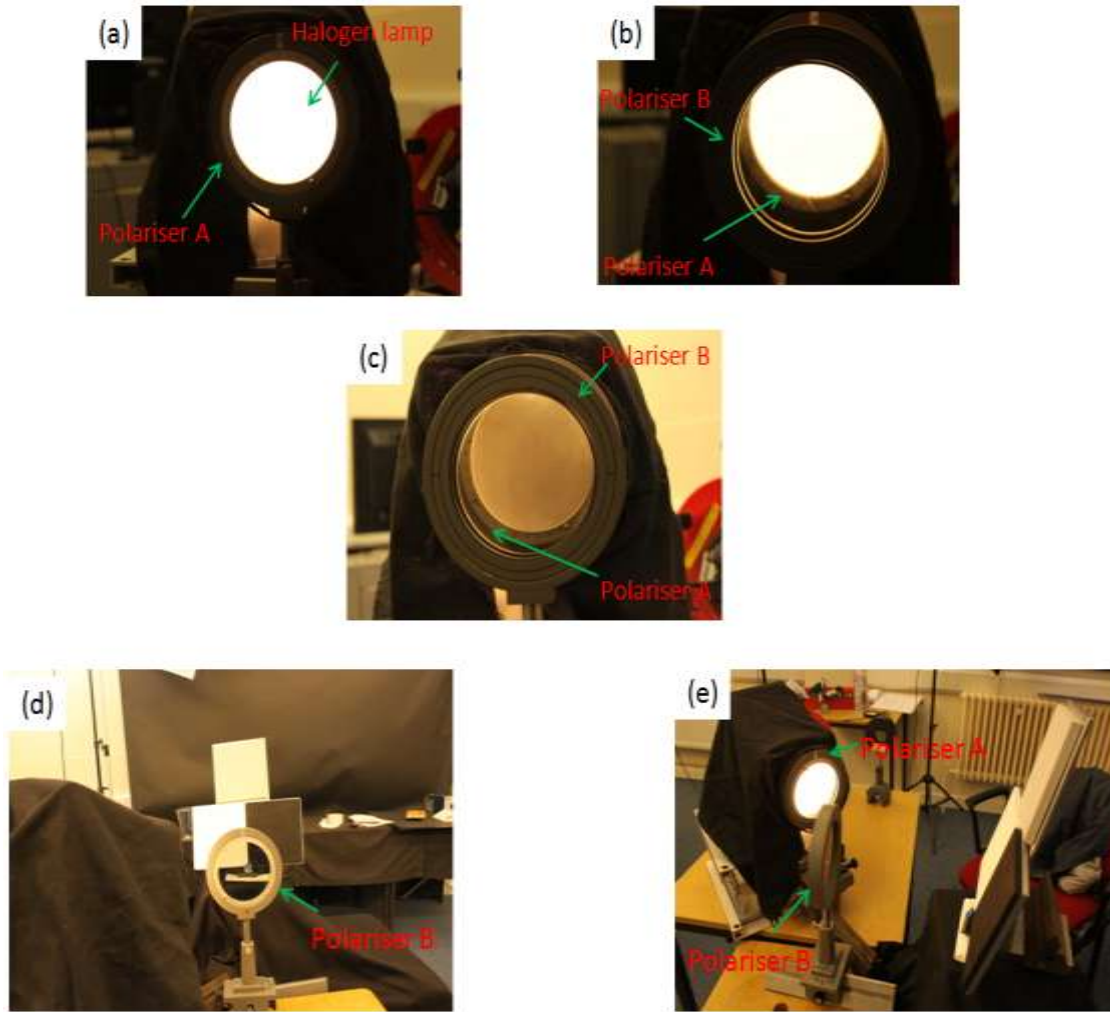


**Figure 5-2 shows the polarisation experiment for measuring the specular reflection due to skin surface: (a) Polariser A (PLA) is put in front of halogen lamp for generating a polarised light source; (b) Polariser B (PLB) is placed in front of PLA with polarisation parallel to that of PLB; (c) PLB is crossed polarise with PLA; (d) Front view of PLB crossed polarise with PLA; (e) Side view of (d).**

A human palm of Asian ethnics (Chinese) has been used as the target object. Standard white and black spectralons with reflectance being 0.98 and 0.02 in the wavelength range of [250-2500]nm respectively have been positioned in the background (see Figure 5-3) as calibration materials for the reflectance conversion via ELM using Equation 4-9, Equation 4-10, Equation 4-11.

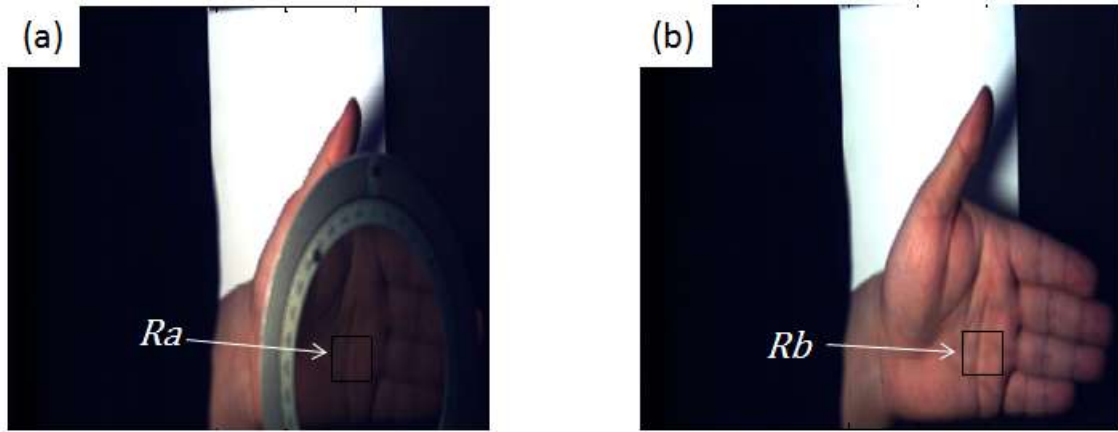
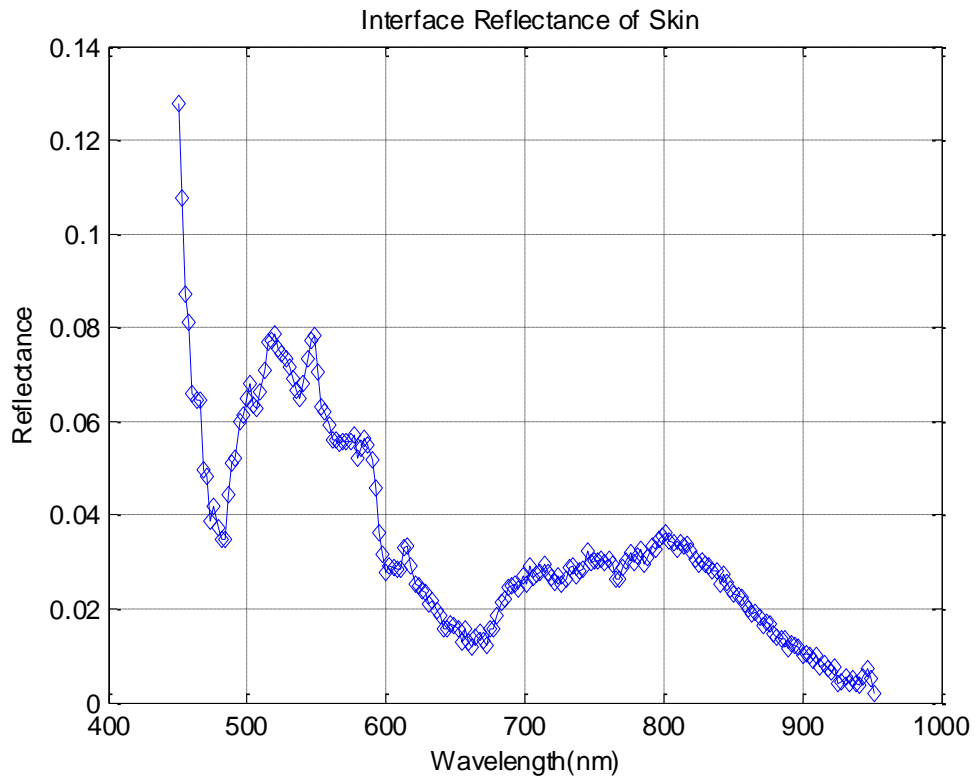


Figure 5-3 shows fRGB images of a palm. (a) With polariser in front of the palm. (b) Without polariser in front of the palm. The black square depicts the location of the ROI.

### 5.3.3 Measuring The Specular Reflectance of Skin

Two HSI images of the palm are taken with and without polariser in front of the target as shown in Figure 5-3 (a) and Figure 5-3 (b) respectively. The palm keeps stable in these two conditions and ROIs of the same area of the palm are selected.  $Ra$  and  $Rb$  are the mean reflectance of two ROIs with and without polariser respectively. From the section 5.3.1 it is known that  $Ra$  is solely body reflectance and  $Rb$  is the total reflectance including specular reflectance and body reflectance. Therefore, the skin specular reflectance is the difference between  $Rb$  and  $Ra$ , i.e.  $R_{specular} = Rb - Ra$ , with spectral characteristics as shown in Figure 5-4.



**Figure 5-4 shows Interface (specular) reflectance of skin in wavelength range of [450-950]nm.**

## 5.4 StO2 Measurement Using Body Reflectance

Unlike in the previous chapter where the absorbance is evaluated using  $\log(1/R)$  where  $R$  is the apparent reflectance of the target without taken into account of the specular reflection of skin (see Equation 4-8), in this section the body tissue reflectance is estimated by excluding the specular reflectance of skin, and the body absorbance can be written as:

$$A_{\lambda body} = \ln\left(\frac{1}{R_{\lambda body}}\right) = \ln\left(\frac{1}{R_{\lambda total} - R_{\lambda specular}}\right) \quad \text{Equation 5-1}$$

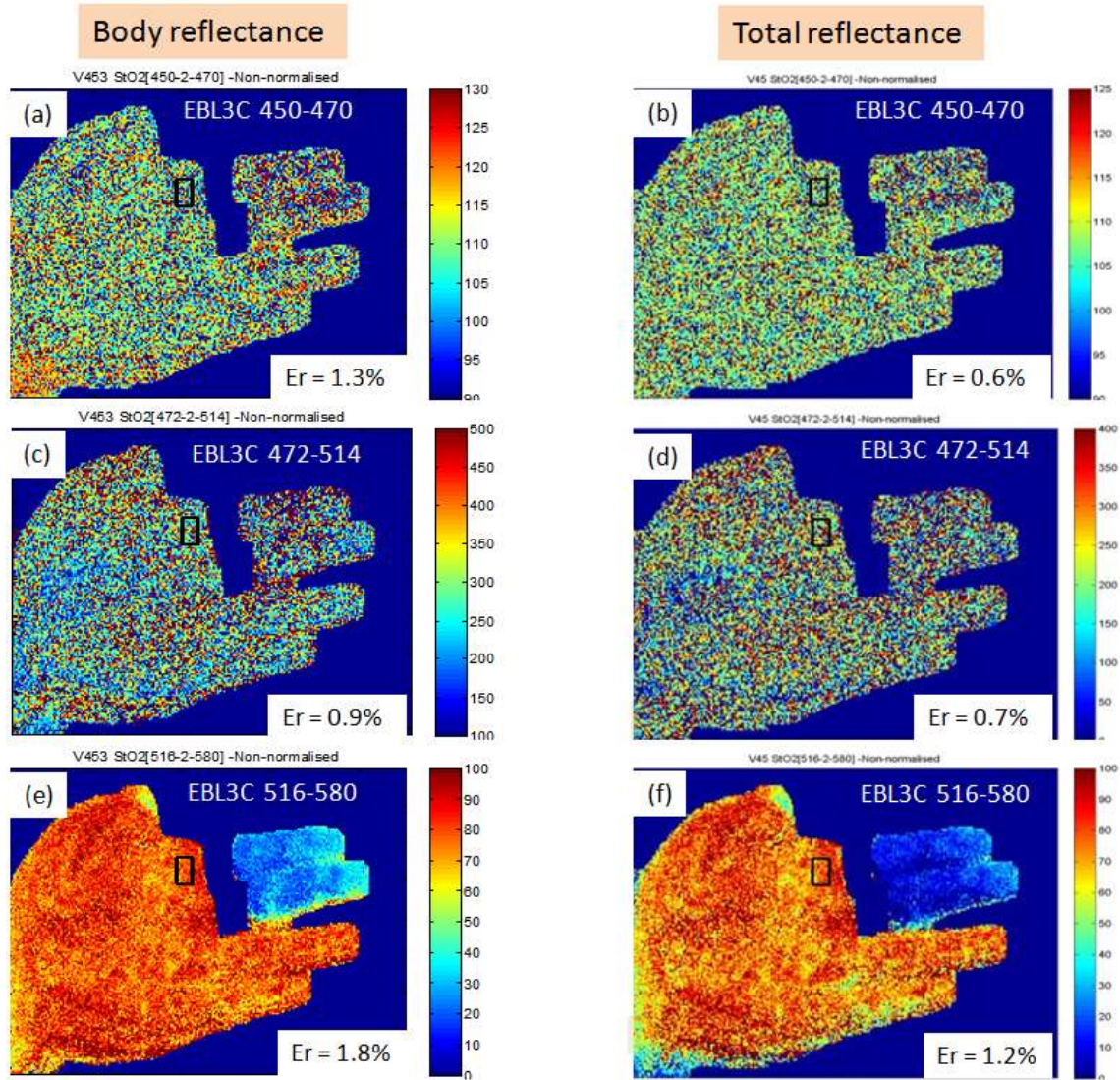
where  $A_{\lambda body}$ ,  $R_{\lambda total}$ ,  $R_{\lambda specular}$  and  $R_{\lambda body}$  denote the absorbance of the body tissue, the reflectance of total reflection, the specular reflectance of the skin and the body reflectance of the skin tissue respectively. Note that the spectral characteristics of  $A_{\lambda body}$  is quite different from the  $A_{\lambda}$ , which includes the specular reflection of skin surface.

The use of this  $A_{\lambda body}$  under the EBL3C model for the StO2 assessment is compared with that using  $A_{\lambda}$ , and the results are presented in the left and right columns in Figure 5-5 to Figure 5-8 respectively. The results of the StO2 maps for the top illuminated data (see Figure 4-1 (a)) are presented in Figure 5-5, Figure 5-6. And Figure 5-7, Figure 5-8 show the results of the front illuminated data (see Figure 4-1 (b)). The range of the spectral data input and the model error evaluated from the black rectangular ROI are labelled in each StO2 map for clarity.

It is observed from the figures that the distribution of the StO2 levels over the whole palm of the same data set has little difference between using the  $A_{\lambda body}$  and  $A_{\lambda}$ . However, it is the scaling of the StO2 level which is seen to be improved after using the  $A_{\lambda body}$  as the input data. For example, the un-physical negative values of the StO2 that were seen in the assessment using the [450-850]nm spectral data are absent in the  $A_{\lambda body}$  analysis for both of the top and front illuminated cases. For example, the maximum and minimum of the StO2 level for using the spectral inputs of [450-850]nm under the top illumination are found to be [110 -10] and [100 0] for the  $A_{\lambda}$  and  $A_{\lambda body}$  analysis respectively (see Figure 5-6 (e) and (f))

However, it is seen that the improvement for using the spectral input of [582-700]nm is not obvious in the  $A_{\lambda body}$  analysis. Small negative StO2 still exists after the specular reflection of skin is removed (see Figure 5-6 (a) and Figure 5-8 (a)). It is noted that the extinction coefficients of Hb and HbO2 in [580-610]nm exhibit rapid fall by almost 40 times, imposing large uncertainty in the absolute molar absorptivities within this narrow spectral region. As discussed in section 4.5.2, this will induce significant errors in the StO2 assessment which may be partly responsible for the above observation.

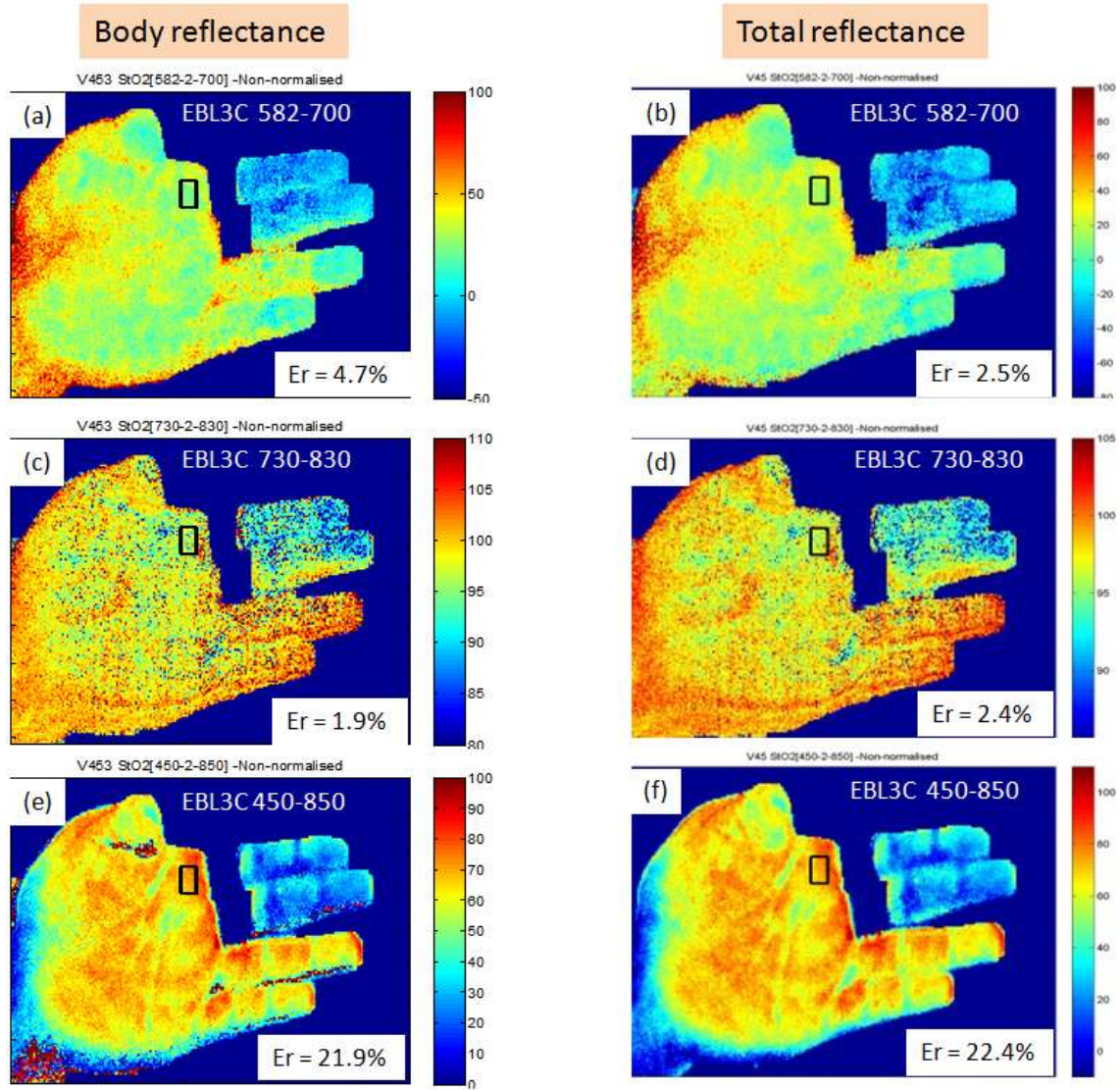




#### TOP ILLUMINATION

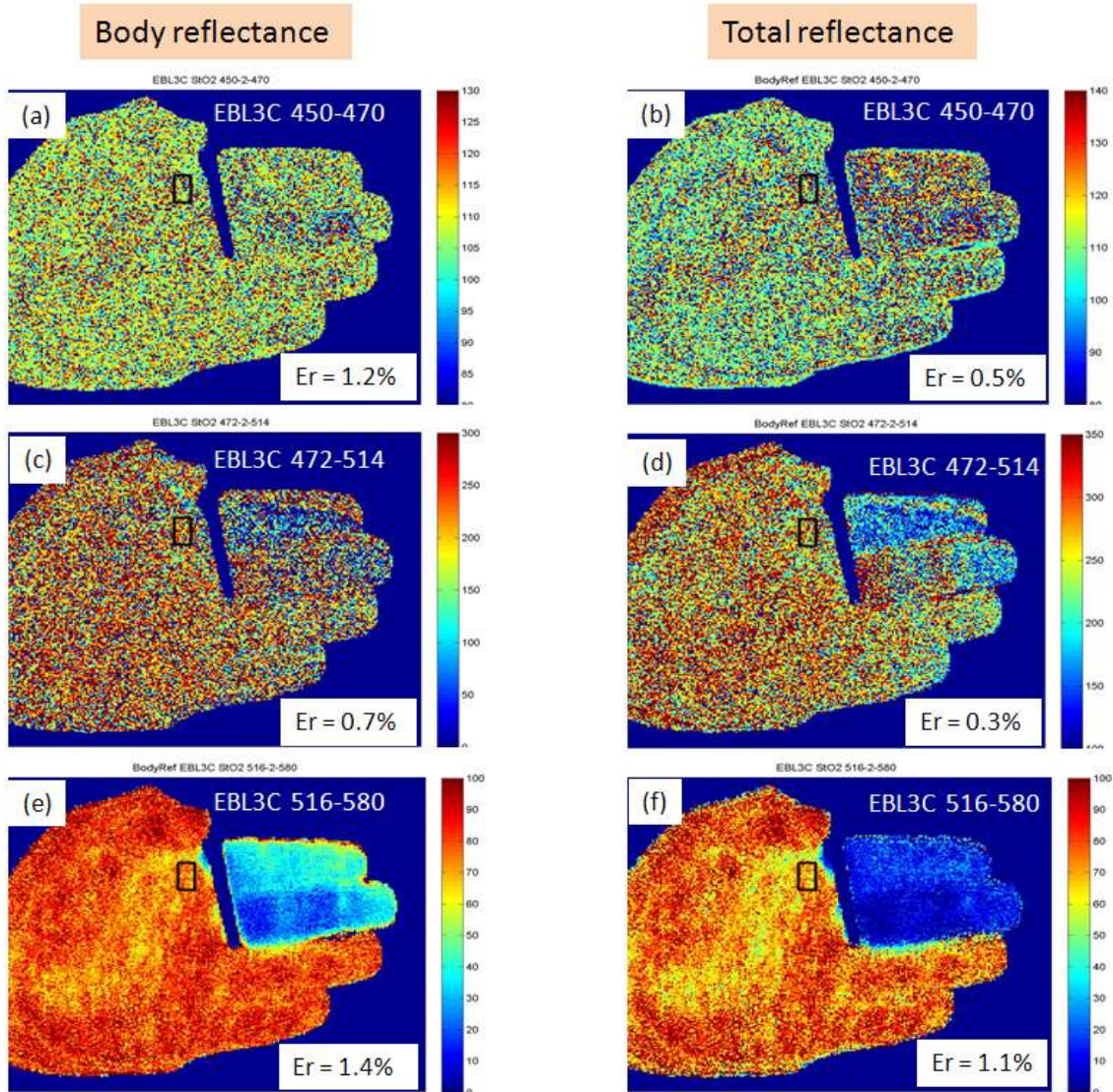
Figure 5-5 shows the StO<sub>2</sub> map obtained from the EBL3C model for a palm under top illumination using  $A_{\lambda_{\text{body}}}$  analysis (Left column) and  $A_{\lambda}$  analysis (right column) for the spectral inputs of [450-470]nm, [472-514]nm, [516-580]nm.





#### TOP ILLUMINATION

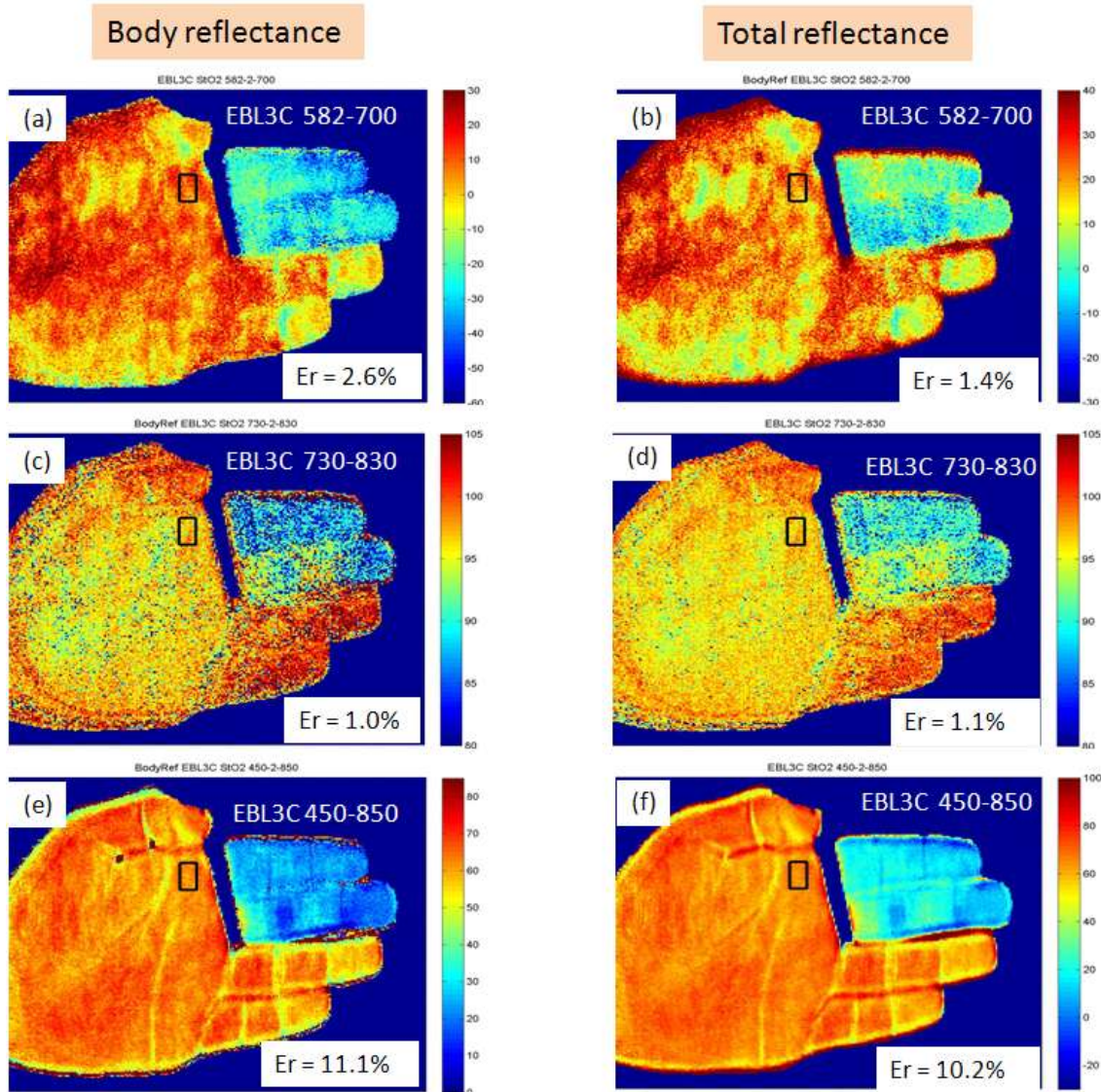
Figure 5-6 shows the StO<sub>2</sub> map obtained from the EBL3C model for a palm under top illumination using  $A_{\lambda, \text{body}}$  analysis (Left column) and  $A_{\lambda}$  analysis (right column) for the spectral inputs of [582-700]nm, [730-830]nm, [450-850]nm.



#### FRONT ILLUMINATION

Figure 5-7 shows the StO2 map obtained from the EBL3C model for a palm under front illumination using  $A_{\lambda, \text{body}}$  analysis (Left column) and  $A_{\lambda}$  analysis (right column) for the spectral inputs of [450-470]nm, [472-514]nm, [516-580]nm.





#### FRONT ILLUMINATION

Figure 5-8 shows the StO2 map obtained from the EBL3C model for a palm under front illumination using  $A_{\lambda, \text{body}}$  analysis (Left column) and  $A_{\lambda}$  analysis (right column) for the spectral inputs of [582-700]nm, [730-830]nm, [450-850]nm

It is found that there is negligible differences between the  $A_\lambda$  and  $A_{\lambda body}$  analysis using the 'optimal' spectral input range of [516-580]nm for the StO2 assessment: a mere ~3% increase after the specular skin reflection is removed (see Figure 5-5 (e) and (f)). The use of other spectral input ranges cannot produce better StO2 results (see previous sections).

However, it is also noticed that slightly higher StO2 levels have been found at the edges of the palm target when the specular reflection is removed (see Figure 5-5 (e), Figure 5-6 (e)). This may be due to the large incident angles involved in the round end of the edge of the palm, inducing significant bidirectional reflection differential effect: recalling that the specular reflection function was assessed only at small incident angles (see Figure 5-2) and thus it may not be applicable to this part of the target.

As discussed previously the results presented in Figure 5-5 (a) & (c), Figure 5-7(a) & (c) using spectral inputs of less than 516nm are not suitable for assessing StO2 because of the high absorptivities of these wavelengths by the epidermis.

Table 6 and Table 7 respectively present the model errors of the palm and finger ROIs under different BL models for the  $A_{\lambda body}$  analysis using various spectral input ranges. Again, this result has shown having a smaller error for the StO2 assessment using the EBL3C model. Note that these tables should be compared with that presented in Table 4 and Table 5 in section 4.5.4, which use the  $A_\lambda$  for StO2 processing. Although the model errors in the result using  $A_{\lambda body}$  in general are higher than that using the  $A_\lambda$ , the StO2 assessment is more realistic when the specular skin reflection is removed. For example, the ischemia finger shows unrealistic low StO2 level of ~5% in the  $A_\lambda$  result ( Figure 5-7(f)) while the  $A_{\lambda body}$  result indicates a more believable oxygenation of ~30-40% (see Figure 5-7(e)).

**Table 6 model Error of palm ROI at various wavelength ranges with BLs method using body reflectance.**

	Wavelength(nm)											
	450:470		472:514		516:580		582:700		730:830		450:850	
Method	Top illu	Front illu	Top illu	Front illu	Top illu	Front illu	Top illu	Front illu	Top illu	Front illu	Top illu	Front illu
<b>BL2C</b>	5.88%	6.96%	4.85%	4.83%	10.90%	11.44%	30.65%	42.65%	4.50%	5.20%	62.34%	65.43%
<b>BL3C</b>	1.34%	1.26%	1.69%	1.55%	1.90%	1.80%	6.44%	2.64%	2.12%	1.24%	24.03%	12.88%
<b>EBL2C</b>	1.36%	1.28%	1.40%	1.22%	2.75%	2.48%	8.18%	3.73%	2.16%	1.31%	26.97%	13.69%
<b>EBL3C</b>	1.31%	1.24%	0.94%	0.66%	1.76%	1.40%	4.69%	2.62%	1.89%	1.00%	21.80%	11.14%

**Table 7 model Error of finger ROI at various wavelength ranges with BLs method using body reflectance.**

	Wavelength(nm)											
	450:470		472:514		516:580		582:700		730:830		450:850	
Method	Top illu	Front illu	Top illu	Front illu	Top illu	Front illu	Top illu	Front illu	Top illu	Front illu	Top illu	Front illu
<b>BL2C</b>	7.18%	6.08%	5.48%	4.67%	12.82%	9.75%	42.46%	44.29%	6.26%	5.35%	67.67%	64.25%
<b>BL3C</b>	2.42%	2.04%	2.42%	1.75%	3.18%	1.78%	5.97%	1.43%	3.51%	1.22%	10.35%	10.76%
<b>EBL2C</b>	2.45%	2.03%	2.40%	1.40%	4.95%	2.61%	8.56%	3.60%	3.52%	1.26%	20.25%	10.89%
<b>EBL3C</b>	2.48%	2.07%	2.40%	1.09%	3.13%	1.57%	3.71%	1.43%	3.50%	1.20%	10.62%	7.64%

## 5.5 Conclusion

In this chapter a study of the effect of the specular reflection due to the skin on the accuracy of the remote sensing of StO<sub>2</sub> is performed. The diffuse scattered photons due to the body tissue have been assessed using polarisation techniques. The specular reflection of the skin is evaluated as the difference between the total reflection ( $A_{\lambda}$ ) without using polariser and the skin tissue's body reflection ( $A_{\lambda body}$ ). In great contrast to most of the previous reported work, the specular reflection of skin is found to be wavelength-dependent.

The most significance improvement for using the tissue's body reflection ( $A_{\lambda body}$ ) in this work is the enhancement of the StO<sub>2</sub> fidelity which exhibits more realistic oxygenation values over the whole target, than that of previous work which conventionally uses total reflections ( $A_{\lambda}$ ) for the evaluation of tissue oxygen saturation and/or to assume a wavelength independent effect of the specular reflection of skin. Furthermore, the un-physical negative values of

StO<sub>2</sub> as seen in the conventional analysis using total reflections  $A_\lambda$  from target, are almost completely removed when the body tissue reflection  $A_{\lambda body}$  is adopted for the analysis.

It is also evidenced from this work that not only the specular reflection from skins can cause errors in the remote sensing of oxygenation, the accuracy of the extinction coefficients of the chromophores, such as Hb and HbO<sub>2</sub>, can induce significant errors in StO<sub>2</sub> assessment too. This factor becomes more important especially when large drop or increase of extinction coefficients are occurred within a small spectral region, such as that in [582-700]nm range, which can induce large errors in the oxygenation assessment. One good example is the persistence of the negative StO<sub>2</sub> values of the target for using this range of input data even after the specular reflection of skin is removed.

Similar to the results in the last chapter, it is confirmed that spectral data in the wavelength range shorter than 516nm cannot give information about blood oxygenation in the palm tissue, and the EBL3C has been found to be the most suitable method for the remote sensing of blood oxygenation over all other four BL models.

## **6 COMPARISON OF HYPERSPECTRAL IMAGING AND THERMAL IMAGING FOR ASSESSING TISSUE OXYGEN SATURATION**

### **6.1 Introduction**

Hyperspectral imaging (HSI) and thermal imaging (TI) techniques both can assess tissue oxygen saturation (StO<sub>2</sub>) either directly or by measuring the skin blood perfusion as discussed in section 3.7.3. Both techniques can monitor StO<sub>2</sub> in a stand-off distance without contacting to the target tissue. In this chapter, we examine how these two technologies perform in assessing StO<sub>2</sub> in normal conditions, where ambient temperature is constant and body temperature scheme is not dominating, and in some extreme conditions, where the ambient temperature experiences 15°C change or the perspiration prevails. The HSI StO<sub>2</sub> and TI temperature of the same object in various conditions are compared line to line in this chapter, it is found that the HSI StO<sub>2</sub> are more reliable than TI temperature in assessing tissue oxygen saturation.

### **6.2 Instrumentations and HSI StO<sub>2</sub> Assessment Algorithm**

The Hyperspectral imaging (HSI) system that employed is the VNIR HSI system described in section 2.5.2, i.e. a Headwall dispersive imaging spectrometer together with a home-made mirror scanning system as shown in Figure 2-8(a). The system is capable to work in the spectral regions of 400nm to 1000nm with a minimum 0.678nm step. The thermal imaging (TI) system consists of a FLIR SC7600 mid wave infrared camera for skin temperature measurement with a temperature resolution of 0.02°C in the working range of -20°C to +100°C. Broad band halogen lamps have been used throughout the imaging process as illumination source. The algorithm for producing HSI StO<sub>2</sub> is EBL3C (Equation 4-7) described in section 4.2.2, the body reflectance is used for generating absorbance (see Equation 5-1 in section 5.4). Since each pixel of the StO<sub>2</sub> map is affected by surrounding tissues, the final StO<sub>2</sub> map is generated by averaging the raw StO<sub>2</sub> map. Considering the curved contour of objects (face



and palm) imaged in this project, a circular average filter is employed for preserving the objects' outlines. The raw StO<sub>2</sub> map of a human face and the StO<sub>2</sub> maps after averaged by using circular average filter of radius sizes 1, 2, 3, and 4 pixels are presented in Figure 6-1. It is seen that the use of 3 pixel radius size can smooth up the StO<sub>2</sub> while maintaining pattern information, while others cannot produce smooth enough of StO<sub>2</sub> image or impose distortions to the image. Therefore, a circular average filter of 3 pixel radius size has been utilised for smoothing the StO<sub>2</sub> map throughout this research.

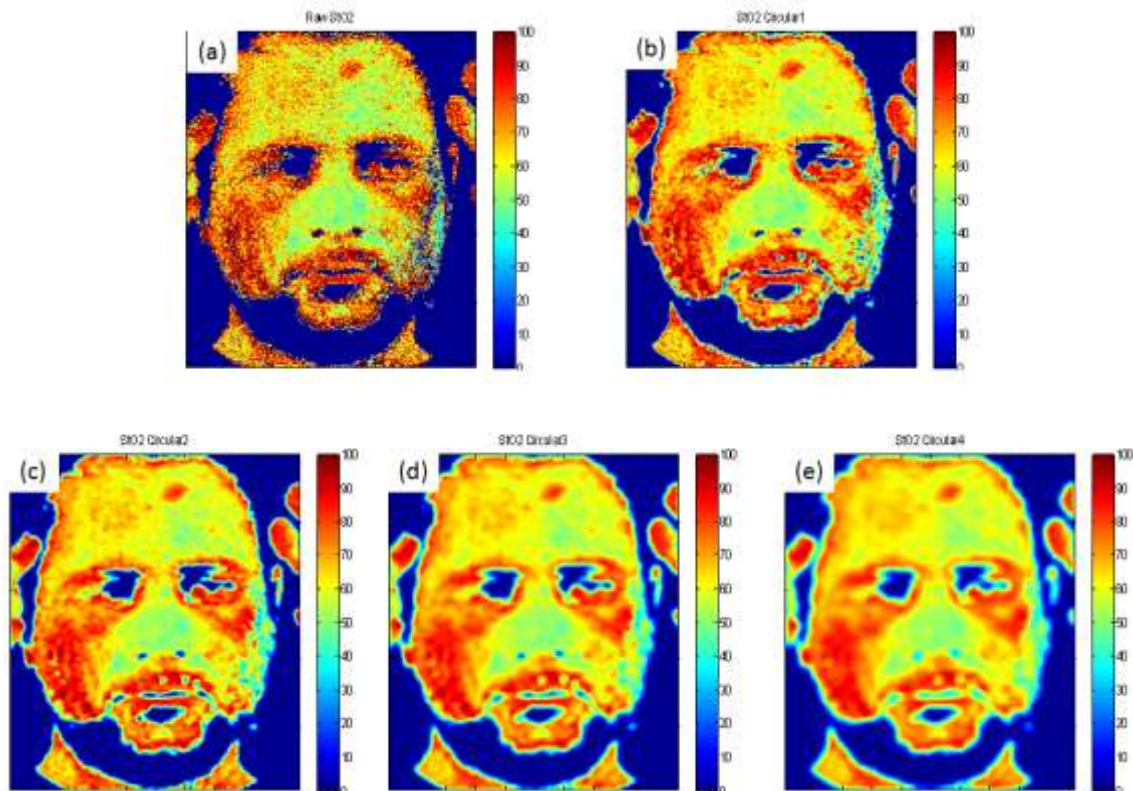


Figure 6-1 shows raw and averaged StO<sub>2</sub> map of a human face. (a) Raw StO<sub>2</sub> map generated with EBL3C using HSI data in [516-580]nm; (b) Averaged StO<sub>2</sub> map generated by averaging (a) with a circular average filter of radius of 1 pixel; (c) 2 pixels; (d) 3 pixels; (e) 4 pixels.

### 6.3 Consistency of HSI StO<sub>2</sub> and TI Temperature

The skin temperature is modulated by the StO<sub>2</sub> in the assumption that ambient temperature and metabolism rate are stable, and that there is no body temperature regulation schemes, such as perspiration, being dominant. To



verify that the change of HSI StO<sub>2</sub> is consistent to the change of TI temperature and vice versa, ischemia experiment is introduced. Ischemia assessments using HSI have been reported in the past showing the effectiveness of the technique for the detection of HbO<sub>2</sub> [13][65][6]. In this work, we compare the StO<sub>2</sub> assessment according to the HSI data with the skin temperature of the ischemia tissues measured by TI as shown in Figure 6-2. The ischemia state is introduced to forefinger and middle finger of a palm of a healthy volunteer by using a tight rubber band over the two fingers for three minutes. After the TI and HSI images of the palm with ischemia fingers are taken, the rubber band is dismissed, which results in fresh blood flushing into the two fingers and makes them being hyperfusion immediately.

The top panel of the Figure 6-2 shows the TI temperature maps of the palm, and the bottom panel shows the HSI StO<sub>2</sub> maps. The left column of the Figure 6-2 illustrates the palm with ischemia fingers, and right column illustrates the palm with hyperfusion fingers. It is seen that the changes of the StO<sub>2</sub> and temperature on the two fingers are consistent to each other. The skin temperature and the StO<sub>2</sub> of the ischemia fingers drop by almost 4°C and 55% respectively with respect to the undisturbed palm. And the hyperfusion fingers see a rise of 1°C and 20% of skin temperature and StO<sub>2</sub> respectively with respect to the normal palm. It is also noticed from the Figure 6-2 that the skin temperature correlates very well with the StO<sub>2</sub> over the whole palm.

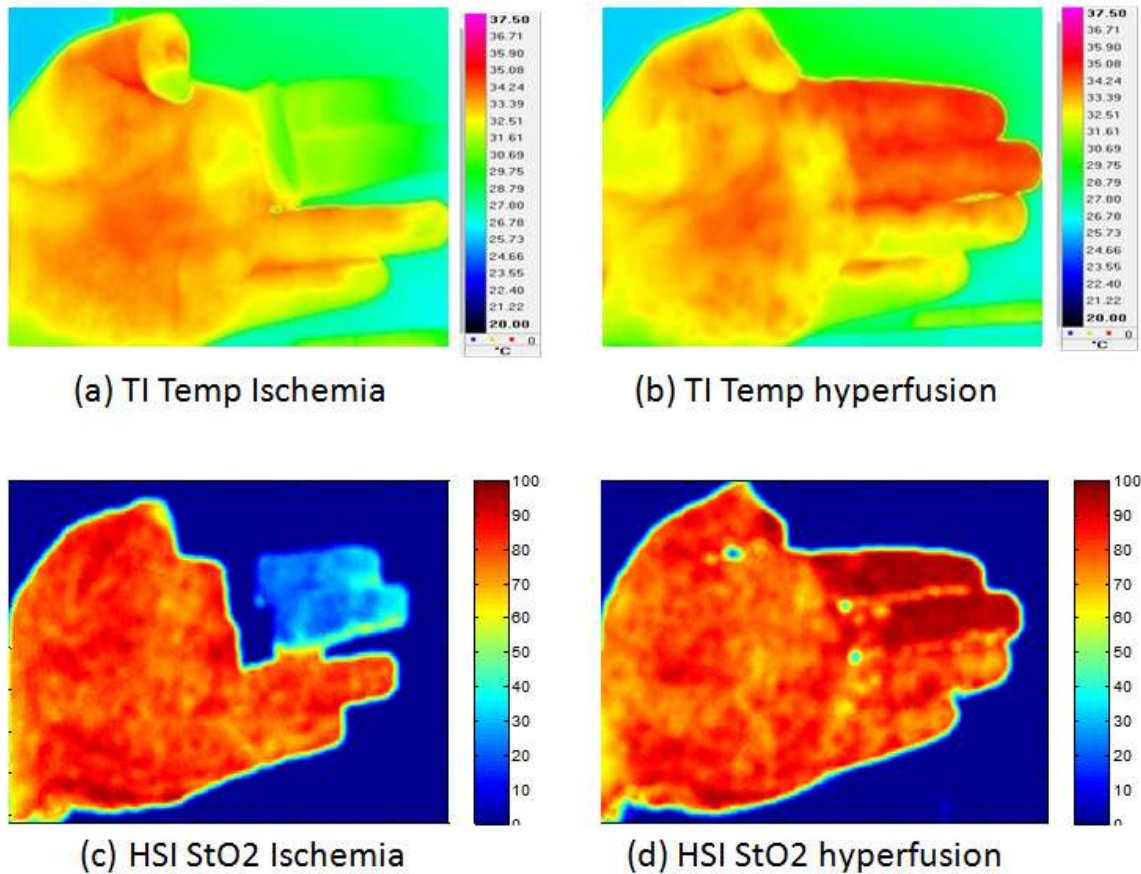


Figure 6-2 shows TI temperature, and HSI StO2 maps of a palm with two fingers in ischemia state and hyperfusion state. (a) Temperature map measured by TI of a palm with two fingers in ischemia state; (b) Temperature map measured by TI of the palm with two fingers in hyperfusion state; (c) StO2 map measured by HSI of the palm with two fingers in ischemia state; (d) StO2 map measured by HSI of the palm with two fingers in hyperfusion state. Note that the change of the StO2 and Temperature of two fingers are consistent to each other very well.

## 6.4 Ambient Temperature Effect

In this section, we compare the environment temperature effect on the skin temperature with that on the skin tissue StO2. Two different ambient temperatures are introduced in a controlled experiment for examining how the StO2 and skin temperature are modulated by environment temperature. In the experiment, subjects are requested to sit on a chair comfortably and calmly in a laboratory environment with room temperature of 20°C for an hour. The TI and HSI data are recorded when their heart beat rates reach a very stable state

during this period. They are then asked to walk outside to stay in an outdoors environment for 10 minutes, where the temperature is around 5°C. The TI and HSI data are recorded again as soon as the subjects return from the outside. Shown in Figure 6-3 is the face temperature and StO<sub>2</sub> maps of a subject. The top panel is temperature, and bottom is StO<sub>2</sub>. The left column is the maps in indoors environment, and the right column is the maps immediately after returning from outdoors environment. The heart beat rate (HBR) of the subject at the time when the TI and HSI data is recorded and is shown at the bottom left corner of each map.

It is seen that the HBR of the subject is stable throughout the experiment, indicating that the body blood circulation is nearly constant. However, the large differential temperatures between the indoor and outdoor environments have caused an abrupt drop of skin temperatures in the face and more notably in the nose region with a reduction of ~8°C observed after the subject returned from outside (Figure 6-3 (b)). This skin temperature in the face is seen to recover after 10 minutes rest in the room at 20°C after the event. In great contrast to the skin temperature measurement, the StO<sub>2</sub> is seen to remain fairly stable after the subject return from outside (left column of Figure 6-3). The StO<sub>2</sub> in the forehead region is seen to drop by a negligible 0.2% of the indoor value, presumably due to the constriction of blood vessels after being in the cold outdoor environment for 10 minutes. Same observations are seen in other parts of the facial region, and the change of the StO<sub>2</sub> due to ambient temperature variation is found to be within experimental error.

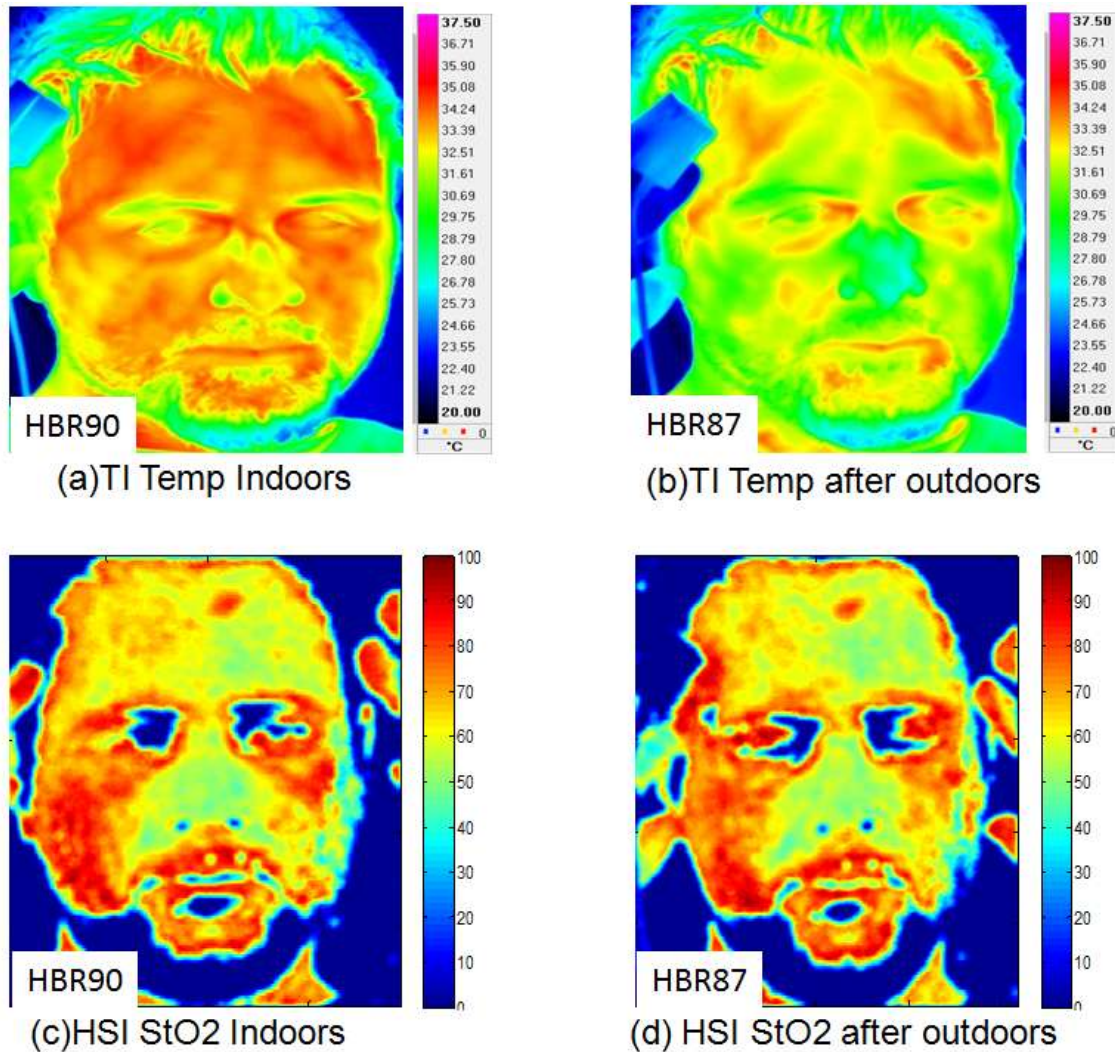


Figure 6-3 shows TI temperature, TI blood perfusion, and HSI StO2 maps of the same human face in warm and in cool situation. (a) Face temperature map in indoors environment, the Heart Beat Rate (HBR) of the subject is 90 at the moment the TI data is recorded; (b) Face temperature map immediately after returning from outdoors environment, HBR is 87; (c) Face StO2 map in indoor environment, HBR is 90; (d) Face StO2 map immediately after returning from outdoors environment, HBR is 87. Abrupt environment temperature changing has great effect on skin temperature, but little on StO2 in this experiment setting.

## 6.5 Perspiration Effect

In this section the effect of sweating on skin temperature and skin tissue StO<sub>2</sub> are examined. For introducing perspiration state, subjects are requested to conduct some exercises in warm indoors environment till sweating. The TI and HSI data of the subjects when they are in baseline condition (calm state before exercise) and in sweating condition are recorded. It is expected that the blood perfusion in the facial region is generally increased after moderate physical exercise [14][13][67].

Figure 6-4 shows the StO<sub>2</sub> maps and the temperature maps in the bottom and top panels respectively. The maps of the baseline condition, great perspiration condition after exercise, and 8 minutes after great perspiration of a test subject are shown in the left, middle and right columns respectively. The HBR of the subject is shown in the bottom left corner of each map. The RGB image of the perspiration is shown in Figure 6-5 where droplets of sweat can be seen clearly.

It is observed that the perspiration reduces the skin temperature dramatically by  $\sim 5^{\circ}\text{C}$  corresponding to  $\sim 11\%$  drop with respect to the base line state particularly in areas of sweat (Figure 6-4). In great contrast to the skin temperature measurement, the StO<sub>2</sub> in the forehead is seen to increase by  $\sim 3.2\%$ , *higher* than the base line state, which is normally the case due to the increase of physical activities, rise of HBR, and perhaps adrenaline in the blood stream [14][13][67]. The heavy sweat observed in the forehead regions (see Figure 6-5) appears to have no effect on the StO<sub>2</sub> deduced from the HSI data in respect of dragging value down as it does to the skin temperature. The skin temperatures in the sweat region are seen not able to be recovered fully even after 8 minutes of rest (Figure 6-4 (c)).



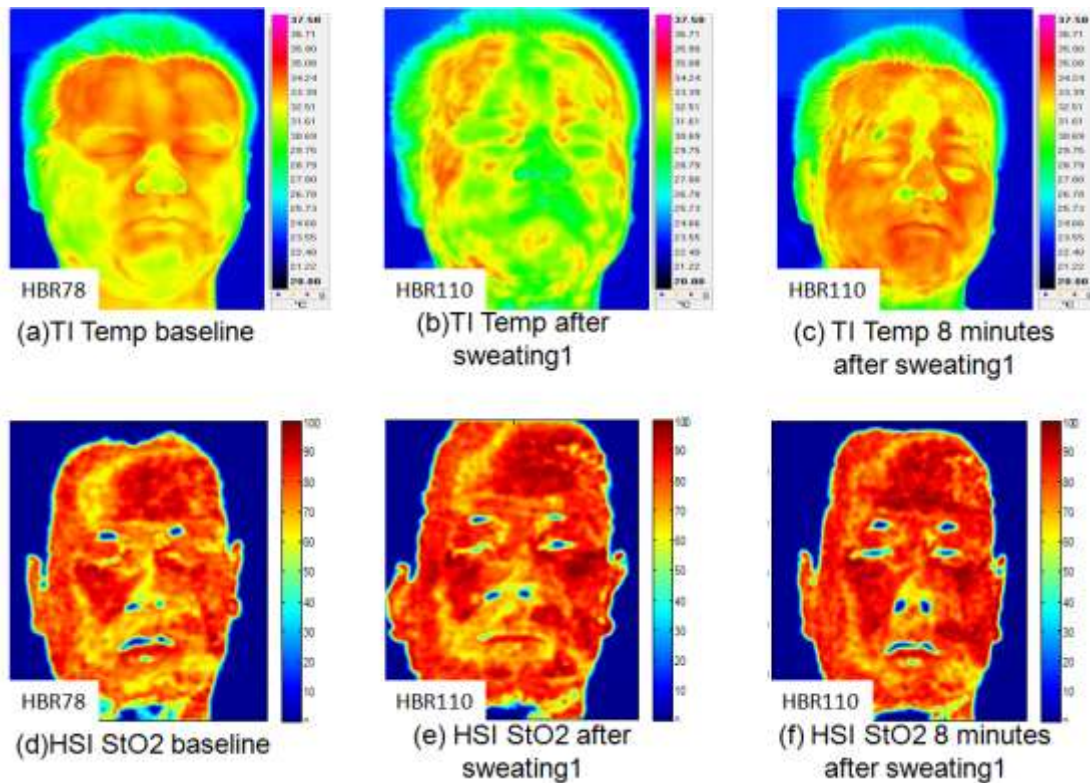


Figure 6-4 shows of TI temperature, and HIS StO2 maps of the face of a healthy subject in baseline and sweating conditions.(a) Baseline face temperature map, HBR is 87; (b) face temperature map in sweat condition, HBR is 110; (c) face temperature map after 8 minutes of (b), HBR is 110; (d) baseline face StO2 map, HBR is 87; (e) face StO2 map in sweat condition, HBR is 110; (f) face StO2 map after 8 minutes if (e), HBR is 110.



Figure 6-5 shows RGB image of the subject after excise in warm environment. Sweat is notable around forehead.

## 6.6 Conclusion

In this chapter we have investigated the relations and differences between StO<sub>2</sub> obtained from HSI technology and the skin temperature from the TI technology. Under normal circumstances of constant ambient temperature and when the subject is not sweating, the StO<sub>2</sub> that deduced from HSI data correlates well with the skin temperature of the tissue.

However, experiment has shown that the skin temperature is very sensitive to the variation of ambient temperatures as well as bodily perspiration. In both cases the skin temperature of tissues can be changed as much as ~10% of the body temperature and it takes a long time (>10 minutes) for the affected tissue to recover back to the normal state.

In contrast to the TI data, the StO<sub>2</sub> that deduced from the HSI is seen relatively independent to the variation of ambient temperatures and bodily perspiration artefacts. The StO<sub>2</sub> have been seen remain stable when the ambient temperature is varied by 15°C, and it is seen to increase by ~3.2% after the physical exercise. This expected small amount of increase in StO<sub>2</sub> after exercise is consistent with the elevation of the blood circulation in the body and perhaps partially due to the increase of adrenaline in the blood stream.

In conclusion, the HSI data is seen more reliable than skin temperature measurement for the assessment of tissue oxygen saturation, which is more independent of ambient temperature change and perspiration.





## **7 SURVEY OF ANXIETY DETECTION**

### **7.1 Introduction**

One main objective of this research is the sensing of emotions, such as anxiety, from a stand-off distance. This chapter is devoted to the review of existing emotion detection techniques, such as the detection of anxiety through hormone detection, functional magnetic resonance imaging (fMRI), facial expression, thermal imaging and techniques based on StO<sub>2</sub>.

### **7.2 Hormones Detection**

Two hormones, adrenaline and cortisol, are released by adrenal medulla and cortex respectively during anxiety state. The detection of these hormones can disclose the human anxiety. High performance liquid chromatography (HPLC) is often employed to analyse the adrenalin content in blood. However, this method is non-realtime, invasive, and imposable for remote sensing purpose. To measure the cortisol secreted during anxiety, saliva test [68] is used. The salivary cortisol measurement is widely employed in psychological research for assessing the activation of hypothalamus-pituitary-adrenal (HPA) axis due to its non-invasive and easy operation manner. Although the measurement of salivary cortisol relies on chemelectronic way, which is not realtime, it would be a good reference for detection result of this project. Therefore, the background of stressor-induced salivary cortisol measurement is reviewed in this section.

Following the psychological stressors being identified as threat, HPA axis may be activated and the end product of the axis cortisol is released from the adrenal cortex into the blood stream. Around 90%-95% cortisol in the plasma becomes invalid in acting on the target tissues as they are bound to the corticosteroid-binding globulin (CGB), albumin, and erythrocyte membranes to less extent. The rest 5%-10% unbound cortisol travels in the blood stream to target tissue and affects the metabolism there. Due to the characteristics of light molecular weight and lipid-solubility, unbound cortisol is capable of easily diffusing through the acini, which are clusters of cells acting as basic secretory units of salivary gland. The concentration of salivary cortisol is independent of

the saliva flow and is highly correlated to the concentration of unbound cortisol in plasma (with correlation coefficient larger than 0.90). Thus it is widely accepted that the salivary cortisol concentration is a good biomarker of activation of HPA axis.

The time lag between increase of cortisol in plasma and the increase of salivary cortisol is within minutes. The rise of the concentration of salivary cortisol is observed in the first minute of the injection 5 mg cortisol into blood in [69], and the maximum salivary cortisol concentration appears after 1-2 minutes of injection. However, the release of the cortisol from the adrenal cortex is modulated by the ACTH from pituitary gland. There is 10-15 minutes lag between the maximum secretions of these two hormones, despite of age, gender, and individual difference according to various papers reporting the time dependence of the cortisol response [70][71][72]. Figure 7-1 shows that the ACTH keeps rising till the top at the point the stressor test is over, and then begins to drop towards the baseline. While the total plasma cortisol and salivary cortisols have delay response. From the moment when the stressor test is over, the cortisol concentration continues experiencing increase till around 12 minutes later and then starts to fall. And moreover, it takes around 20-50 minutes [70][71][72] for the highest cortisol concentration to go back to baseline value just before the stressor test begins. This is illustrated in Figure 7-1. Around 50 minutes are required for both the plasma cortisol and salivary cortisol drops back to normal.

It is believed that distress (negative) can trigger the cortisol response. A lot of experiments have been performed to activate the HPA axis via various psychological stressors including public speaking [73], cognitive task, [74] emotion induction [75], and etc. Dickerson [76] inspects 208 laboratory studies of acute psychological stressors and concludes that not all the stressors elicit the same cortisol response. Meta-analysis shows that the combination of public speaking and cognitive task has the maximum effect size of cortisol increase as Figure 7-2 shows. And with respect of the characteristics of stressors, Dickerson concludes further that it is the stressors with uncontrollable and

social-evaluative essentials that give the strongest cortisol response (Figure 7-3) and the longest recovery time, which means a situation, in which participants may not achieve the final goal even if they tried their best and participants may be negatively estimated, is a best candidate stressor for obtaining strongest cortisol response.

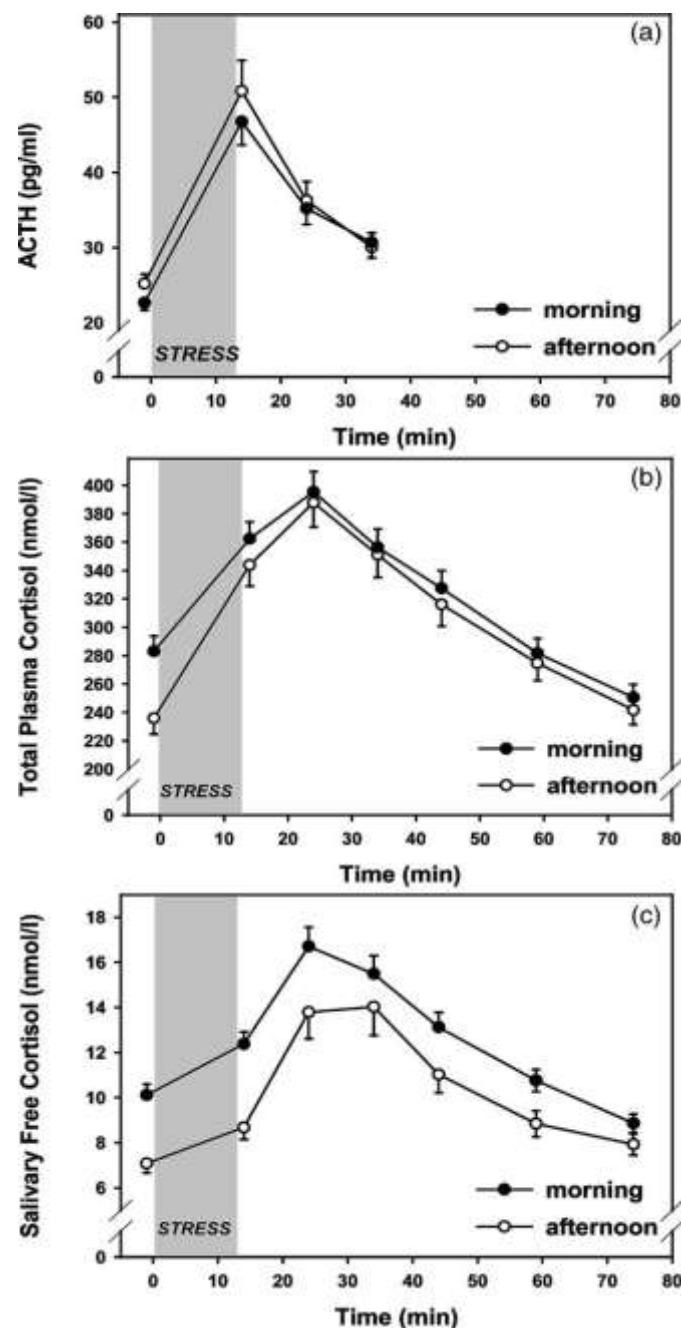
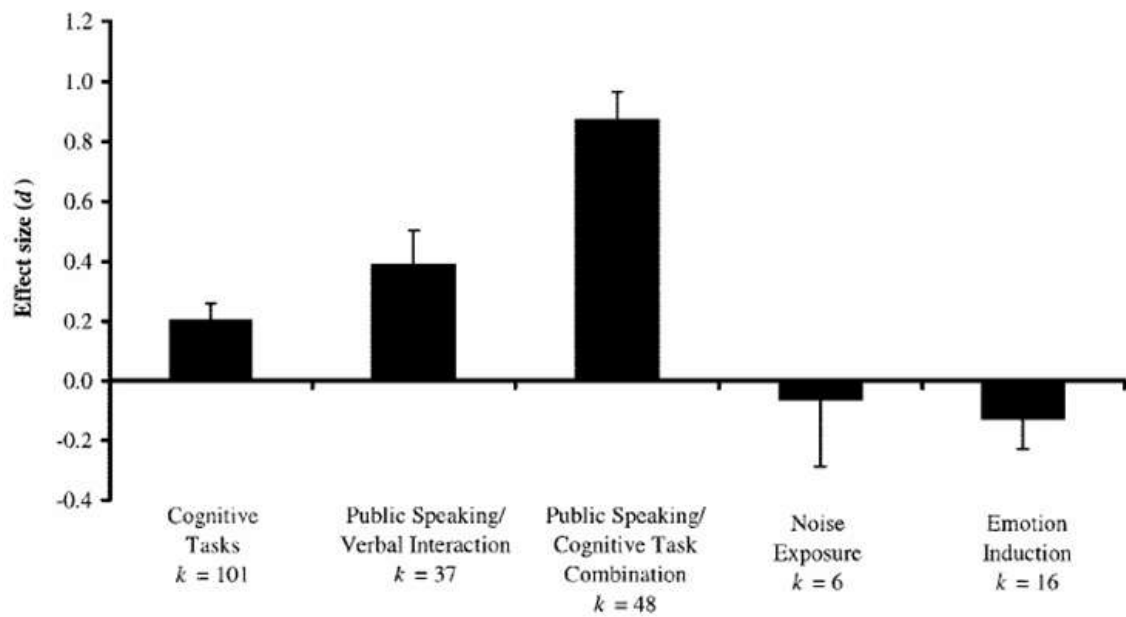
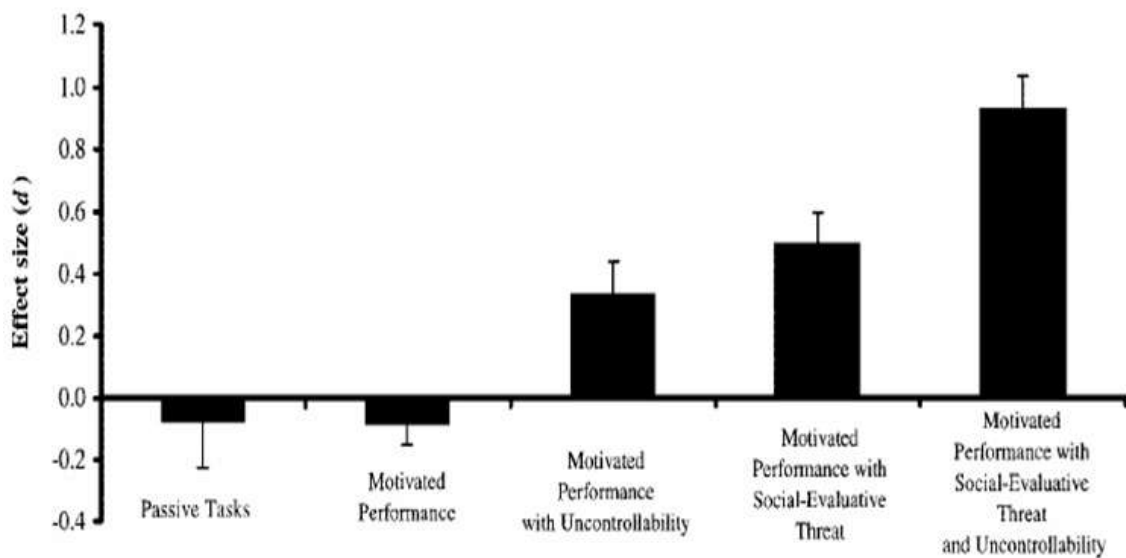


Figure 7-1 (a) ACTH concentration Vs time. (b) Total plasma cortisol concentration Vs time. (c) Salivary free cortisol concentration Vs time. [72]



**Figure 7-2 effect size of cortisol increase sorted by types of stressors. The combination of public speaking and cognitive task has the maximum effect size of cortisol increase. [76]**



**Figure 7-3 effect size of cortisol increase sorted by characteristics of stressors. It is the stressors with uncontrollable and social-evaluative essentials that give the strongest cortisol response. [76]**

### **7.3 Direct Brain Activity Probe: Functional Magnetic Resonance Imaging (fMRI)**

Functional magnetic resonance imaging is the most accurate non-invasive technology reported so far for detecting human anxiety. It monitors the oxygen consumption information of some areas in a brain, which will be activated during a specific emotion, experience, thought, or action. The theory behind this technology is that the more oxygen consumed by the areas, the more activated the brain areas are, and the more emotion related to the brain area is induced.

BOLD signal is an indicator of local oxygen uptake in fMRI. Haemoglobin inside the blood is capable of carrying oxygen that is then consumed by the active area. The form of haemoglobin fully bound with oxygen is called oxy-haemoglobin, and the form of haemoglobin with oxygen having been consumed by tissues is named as deoxy-haemoglobin. The paramagnetic deoxy-haemoglobin induces strong field inhomogeneity. Thus more deoxy-haemoglobin in an area results in a shorter  $T2^*$  relaxation time, While more diamagnetic oxy-haemoglobin in the area results in a longer  $T2^*$  relaxation time. The blood oxygen-level dependent (BOLD) signal widely employed in fMRI is the signal indicating the concentration of oxy-haemoglobin in a particular area in brain based on the  $T2^*$  relaxation time. The higher the BOLD signal is, the higher the concentration of oxy-haemoglobin is. Therefore, the changes of local BOLD signal reveal the oxygen consumption and the activated level of the area.

Detecting deception using fMRI was first reported by Kozel [77] in 2005. The anterior cingulate and the prefrontal cortex are examined for detection purpose for the first time according to his paper. The accuracy of detection is as high as 90% at that time. Follow on the initial report on the very successful detection of anxiety due to guilty, similar work about the anxiety detection based on fMRI was reported in [78], [79], and [80]. The fMRI is even employed to disclose the anxiety state of people when they are lying in court in 2009 for its high accuracy [81]. Although, there are many other strengths of fMRI, such as non-invasive, no exposure to radiation, and etc., apart from accuracy, this technology is not practical for remote detection purpose. An MRI scanner is highly expensive and

not portable at all. Moreover, for obtaining BOLD signal, the MRI scanner has to be very close to the testee, which losses the covertness for remote sensing.

## 7.4 Facial Expression

Distinctive facial expression is believed to be associated with specific emotional state. The facial expression recognition, a branch of computer vision, focuses on recognising the local facial Action Units (AUs) representing the facial muscular activities that code the facial expression. There are many methods presented for AUs recognition from previous publications [82][83][84]. Forty four facial AUs, some of which are shown in Figure 7-4, and eight head pose action units at 5 asymmetric intensity levels are defined in Facial Action Coding System (FACS) [85], which includes all possible muscle movement in terms of frequency and duration scores. Based on the FACS scoring system, the anxiety expression is related to AUs as shown in Table 8.

Anxiety detection via facial expression recognition relies very much on the recognition of the AUs, which may be controlled by trained person. Though this method can be used in remote monitoring, it may not be reliable if the expression is suppressed.

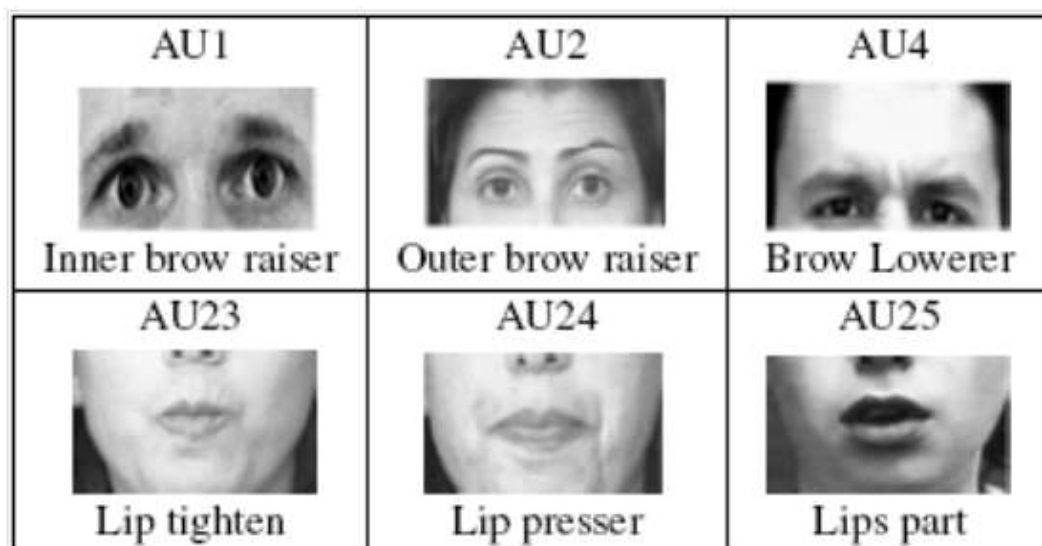


**Figure 7-4 illustration of facial Action Units representing the facial muscular activities that code the facial expression.[85]**

**Table 8 scores of AUs of high and low state anxiety based on FACS.[85] Some scores, such as fear actions, are the score of group of Aus.**

Means for Facial Action Codes for state anxiety		
Facial Action Codes	State anxiety	
	High	Low
Fear actions	1.54	0.76*
Eye blinks	20.78	19.00*
Total movement	11.3	9.81***
Enjoyment smiles	0.3	0.32
Non-enjoyment smiles	1.76	1.62
Anger-contempt-disgust	0.57	0.38
Sadness-pain	0.14	0.14
Doubt	1.08	0.95

Note:\*P<0.01;\*\*P<0.05; \*\*\*P<0.02

## 7.5 Physiological Signal Based Anxiety Detection Techniques

Physiological changes of human on the onset of anxiety include raised heart beat, raised respiration rate, higher blood pressure, higher body temperature, perspiration, muscle contraction, pupil dilation, etc. These physiological signals, being able to serve as anxiety features, are detectable via various medical meters, or custom developed equipments.

Healey et al [86]presented a system called SmartCar to assess drivers emotional anxiety by recording physiological signal of respiration rate, heart beat rate, skin conductance, and muscle contraction. The accuracy of the detection is reported in the range of 62.2% to 88.6%, depending on the combination of features. In [87], blood volume pulse, galvanic skin response (GSR), and pupil diameter are used to detect computer users' anxiety, so that a better human computer interface can be given, which responses the users' anxiety accordingly. The accuracy of anxiety prediction is from 78.65% to 90.10%, depending on the types of classifier. Heart beat rate, skin temperature variation, and electrodermal activity are utilised in [88]for assessing the emotion related to the activation of sympathetic nervous system. The anxiety can be

differentiated from anger, sadness, and surprise with accuracy from 61.76% to 78.43%.

Polygraph testing is one of the most well-known technologies utilising the physiological signals, such as blood pressure, pulse rate, perspiration, body temperature, GSR, to detect human anxiety induced by lying. Although Polygraphs are used in some countries as an interrogation tool, its accuracy and validity have been questioned by scientists [89][90]. And with the same way for obtaining physiological signal measurement as that of medical meters method, it is also impossible for this method to be implemented in remote sensing.

The physiological signal measurement via custom developed or medical meters for anxiety detection can give an accuracy higher than chance probability in general. However, it is not practical in remote sensing application, as the meters and the testees have to be closely contacted.

## **7.6 Thermal Imaging**

Thermal imaging is the only method thus far, except for HSI, which can probe human anxiety remotely. Distinctive heat pattern around face region is believed to be associated with specific emotion state. Thermal signature of anxiety was first observed by Pavlidis et al [91][16][92][15][93] in the early of 21<sup>st</sup> century, who reported that a person's anxiety, alertness, and fear, when he/she experienced a sudden startle, can be disclosed by the increased temperature around periorbital region (see Figure 7-5). The data from our lab in Cranfield also supports that the elevated temperature not only in the periorbital but also in the forehead area during emotional anxiety [67]. This elevation of forehead temperature is also reported by Levine et al in [94], where two different types of emotional stressors are found to be able to increase the forehead temperature as shown in Figure 7-6. The temperature of the forehead area during the two types of stressor, i.e. stroop and mental arithmetic, are found to be highly correlated with correlation coefficient of 0.96 in [94]. Following the founding of the elevation of blood flow in particulars area of face, Pavlidis et al [95][96] proposed that high resolution thermal imaging system can be employed for



continuously monitoring the anxiety state of human based on the changing of temperature pattern of the face. Algorithms for tracking small region of interest of periorbital region is presented in [97] for obtaining stable and high SNR temperature measurement over very small region of interest of periorbital.

Apart from investigating temperature changing of human upon stressor, the responses of mammals to stimulus are studied in many publications. The nose temperature of monkeys is found to be decreasing onset of threat or in negative emotional state in [98][99]. The cows' eye temperature is found to be fairly constant even if they are in stressor test [100]. The temperature of rat's body, back, tail, and paw are investigated in [101]. Remarkable drop of the temperature in the tail and paw is found, which lasts for all fear stimulus experiment. On the other hand, the temperature of eye, head, and back increases.

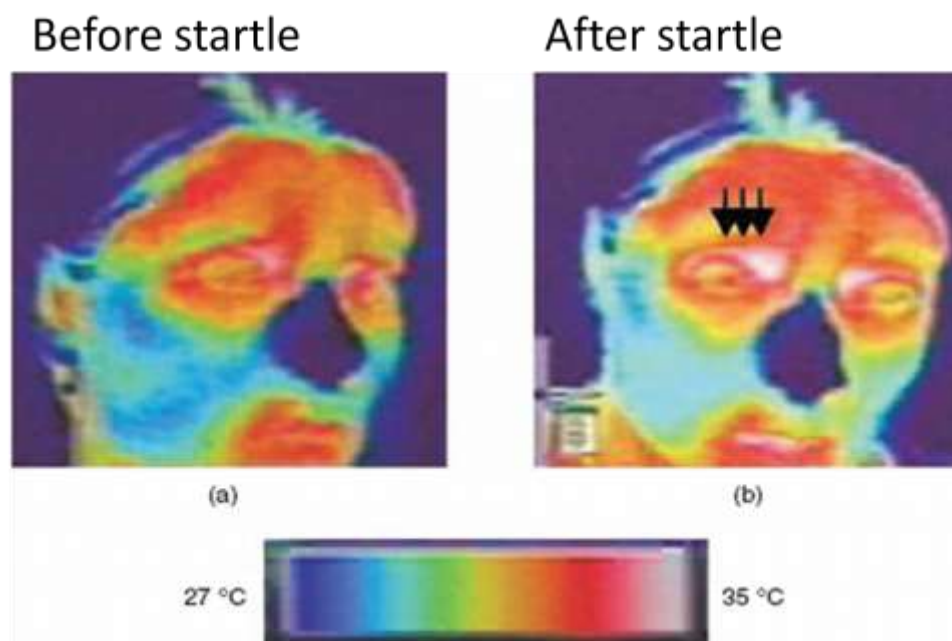


**Figure 7-5 (a) thermal image of face before startle. (b) Thermal image of face after startle. According to the colour bar, the temperature around periorbital region, pointed by the arrows, increases after startle [91].**

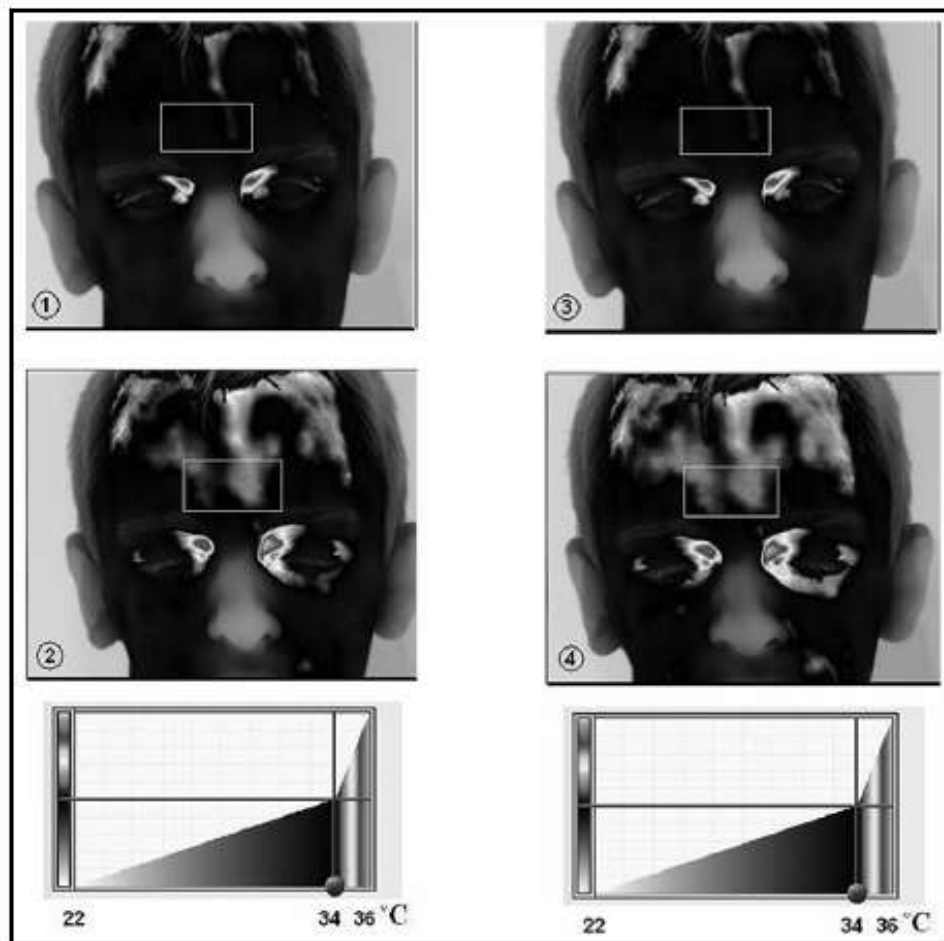


**Figure 7-6 thermal images of a male subject. (1) baseline before Stroop stressor (2) during Stroop stressor provocation test (3) baseline before mental arithmetic stressor provocation (4) after the mental arithmetic stress provocation. The bright pixel around forehead area shows higher temperature after the emotional stressor.**

Physiological signals can be remotely monitored via thermal imaging. In [46] [102], a bioheat model for estimating blood flow speed is reported. The blood perfusion in the tissue region without large superficial vessels is calculated by a perfusion model [95], while the blood flow in the main superficial vessels is computed by a directional model [46]. In [103], the heart beat rate is measured via the temperature variation induced by the fluctuation of blood flow inside the blood vessel on the side of the neck. To obtain best SNR signal, the temperature variation as a function of time along a neck blood vessels is monitored. Fast Fourier Transfer is employed for obtaining the changing

frequency of temperature and thus the pulse rate. The comparison between the measurement by thermal imaging and that by a conventional medical pulse meter shows up to 99% accuracy. In [104], vascular map is first created, based on which blood vessels on forehead are selected. The temperature variation of the blood vessels is fed into wavelet-based signal filter to obtain the pulse rate. The accuracy of the measurement in [104] is claimed to be 89%-99%. And in [105][102], a method for measuring respiration rate is presented based on the temperature variation around the nostril (see Figure 7-7). The correlation between the thermal-measured breath rate and ground-truth rate is reported as 0.9906. The three physiological signals detected by the thermal imager can be employed as an input to the affective computing model used in medical meters method for classification purpose.

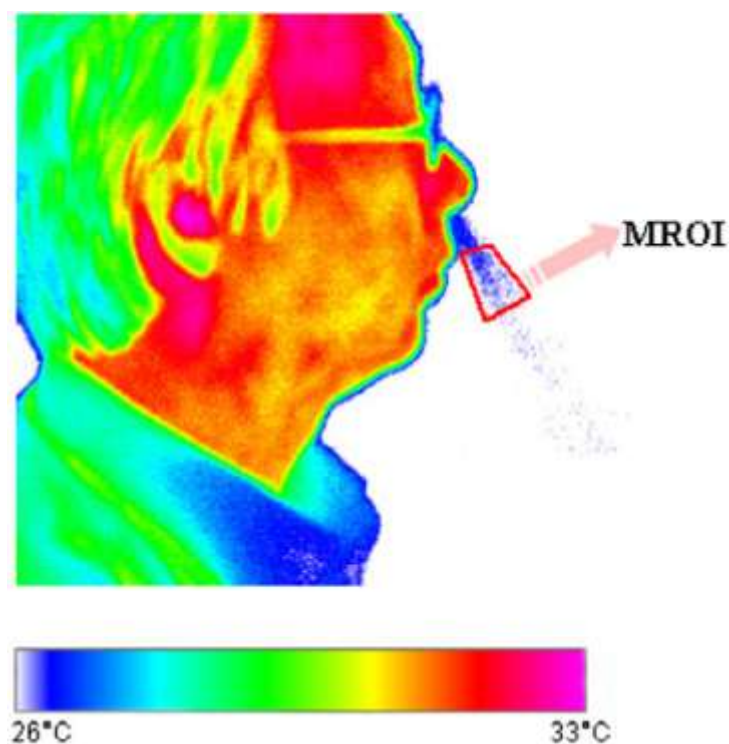


**Figure 7-7 the temperature in the selected region MROI is modulated by the air in the out of the nose. The frequency of the changing of the temperature is taken as the respiration rate.**

In 2011, Jarlier et al [106] reported for the first time that distinctive heat pattern is associated with the activation of specific facial action unite (AU). The difference between the peak temperature of each activated AU and the baseline temperature of each AU is shown in Figure 7-8, from which the obvious difference between AU12 heat pattern and AU4 heat pattern can be observed. As the combination of AU encodes the human expression, the results shown in [106] may open new avenues for detecting human emotion using thermal imaging techniques.

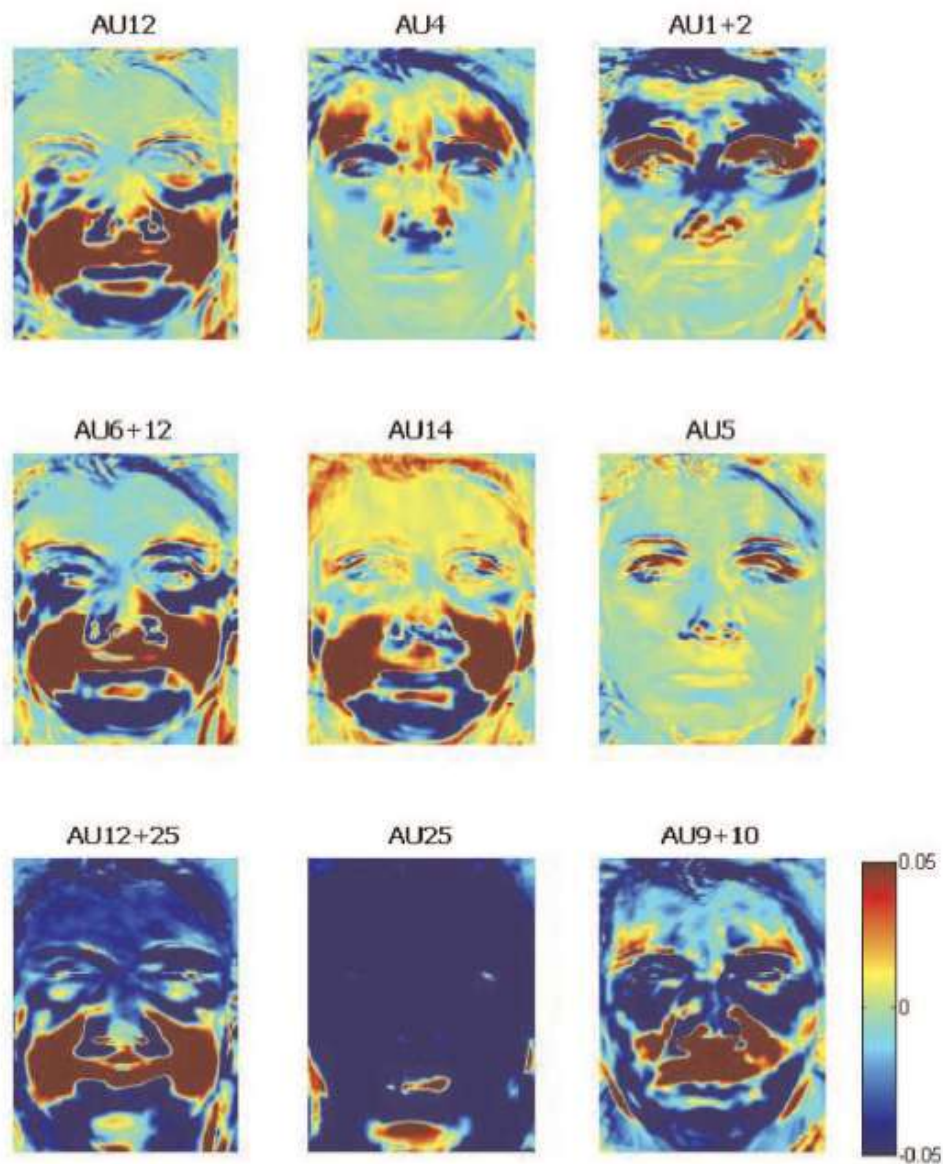


**Figure 7-8 heat patterns (maximum temperature –baseline temperature) change for every AU [106]**

The thermal imaging is a promising technology for assessing human anxiety remotely. There are both pros and cons for this technology. It can give real-time measurement of the face surface temperature, which is the feature for detecting anxiety. However, the temperature measurement can be affected by many factors, such as sweat and ambient temperature. In the case that the face temperature is modulated by the sudden change of sweat or environment temperature, the detection of anxiety can be unreliable (see chapter 6).

## **7.7 Emotion and Tissue Oxygen Saturation**

### **7.7.1 Emotion and Stressor**

Any event or situation is regarded as a stressor to human, if it is deemed as possible threat or needs to be adapted to. The stressor, including physical stressor and mental stressor, can induce emotion associated with anxiety, nervous, worry, and etc. The physical stressor is the stimulus that has direct effect on human body. It can be an uncomfortable external environment condition, such as heat, cold, or noise, or can be due to the internal physical/ physiologic demands of the human body. The mental or emotional stressor is the stimulus only received by human brain and with no direct physical impact on the body. The perceiving to the stimulus may place demands on either the cognitive systems (thought processes) or the emotional system (feeling responses, such as anger or fear) in the brain. The emotion induced by stressor is mainly anxiety, and thus in this thesis the anxiety and stressor-induced emotion have the same meaning if there is no specific explanation.

### **7.7.2 Signature of Stressor-induced Emotion: Arousal of Tissue Oxygenation**

Adrenaline is secreted through hypothalamus-pituitary-adrenal (HPA) axis in response to stressor. It binds to specific adrenergic receptors of peripheral tissues, which prepare the body for the fight-and-flight response [107][108][109][110]:

- Acceleration of heart and lung action

- Liberation of nutrients for muscular action, such as glucose, oxygenation
- Increase of blood pressure, and the blood becomes stickier
- The spleen discharges red and white blood cells, allowing the blood to transport more oxygen throughout the body. Blood flow can increase up to 300 - 400%, priming the muscles, lungs, and brain for added demands.
- Redirection of blood to provide the highest perfusion and fuel to the aroused brain, heart and muscles
- Constriction of blood vessels in many parts of the body, such as skin, stomach & intestine
- Acceleration of instantaneous reflexes
- Dilation of pupil (mydriasis)
- Increase of sweat
- Suppression of concentration, short term memory, rational thought and navigation ability
- Auditory exclusion (loss of hearing), and general effect on the sphincters of the body and tunnel vision
- Inhibition of lacrimal gland (responsible for tear production) and salivation (mouth dryness)
- Inhibition of stomach and upper-intestinal action (digestion slows down or stops)
- Relaxation of bladder, evacuation of colon, inhibition of erection

The first five responses increase the tissue oxygen saturation and tissue oxygen content notably. A controlled adrenaline infusion into human forearm experiment [111] with variable doses shows that the haemoglobin oxygen saturation of venous blood draining from the forearm muscle experiences significant transient increase (Figure 7-9) independent of the dose usage, which indicates a transient increase of muscle tissue oxygen saturation or tissue oxygen content (see section 3.5 for details). The response after the transient increase is dose dependent. The smaller dose (0.05µg/min, 0.1 µg/min intra-

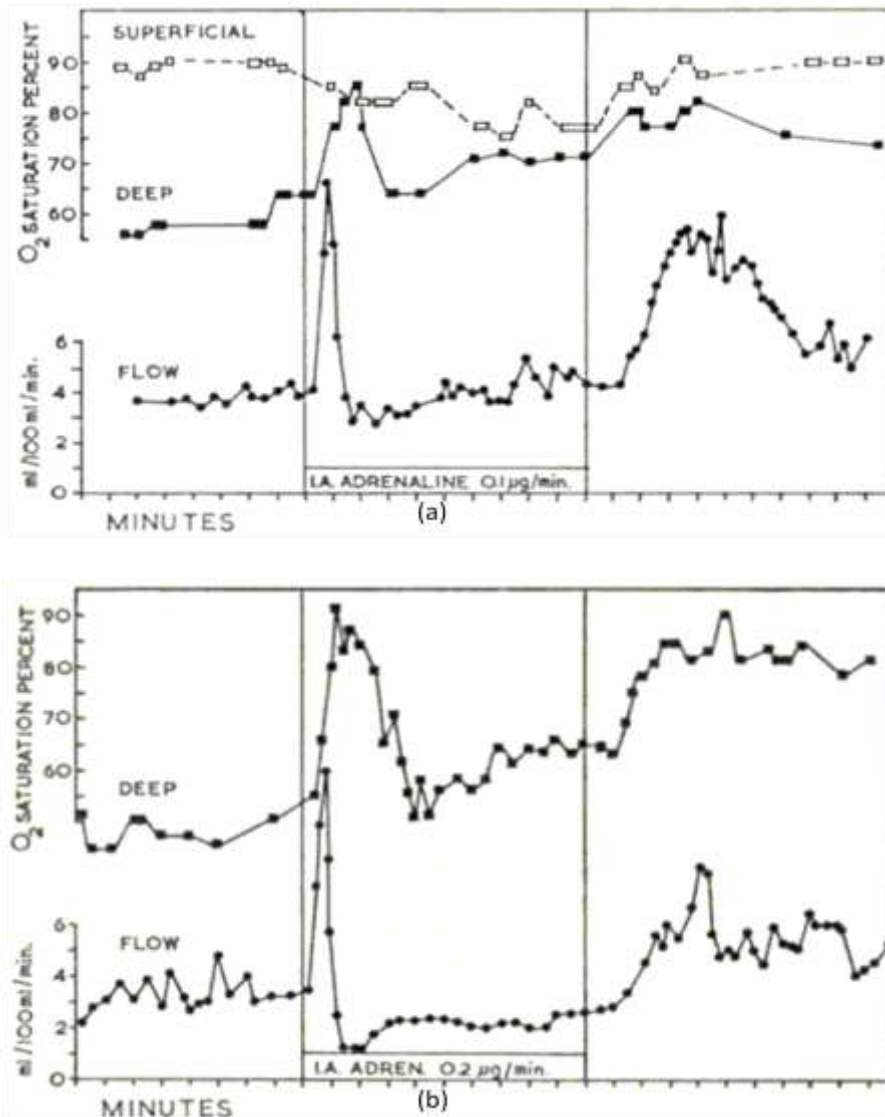


Figure 7-9 (a) DEEP is the haemoglobin oxygen saturation of deep venous blood draining from the forearm muscle. IA. ADREN represents the period Intra-arterial infusion of adrenaline  $0.1\mu\text{g}/\text{min}$ . The venous haemoglobin oxygen saturation has a transient increase, and then maintains a small increase compared to the baseline throughout the infusion. After 4 minutes of stopping the infusion, the oxygen saturation begins to drop. (b) DEEP is the haemoglobin oxygen saturation of deep venous blood draining from the forearm muscle. IA. ADREN represents the period Intra-arterial infusion of adrenaline  $0.2\mu\text{g}/\text{min}$ . The venous haemoglobin oxygen saturation has a transient increase and then decrease to the same even lower level than the baseline. After stopping the infusion, the oxygen saturation goes up and keeps nearly constant for 8 minutes, showing that with the washout of the larger dose infusion, the small dose effect appears (increase the adrenaline) [111].

arterial infusion) induces a sustained increase of venous haemoglobin oxygen saturation, while the larger dose (0.2µg/min, 0.5 µg/min intra-arterial infusion) tends to decrease the oxygen saturation. The dose-dependent response of tissue is also proved by the post-infusion showing that the venous oxygen saturation decreases with the gradual washout of smaller dose of adrenaline, but increases in the larger dose case (Figure 7-9).

A great amount of adrenaline infusion, 2µg/kg per minute, was employed in [112] to investigate the oxygen usage of heart muscle of dog. The oxygen extraction of the muscle decreases dramatically, while the oxygen consumption increases a little during the infusion (Figure 7-10). This results in an increase in muscle tissue oxygen saturation (content) throughout the period of infusion.

A transient increase of blood flow (Figure 7-11), indicating transient increase of oxygen saturation (see section 3.5 for details), on rat's masseter muscle after intravenous infusion is observed in the experiment performed very recently [113]. The response of blood flow after the initial rise is also dose-dependent. The larger dose decreases the blood flow more (Figure 7-11). This experiment also supports that the adrenaline secreted from adrenal gland has the similar effect on the masseter oxygen saturation. The electrical stimulation of SPLN nerve, in charge of regulating adrenaline secretion from adrenal medulla, of the same rats in the experiment causes uninterrupted rise of masseter blood flow at some frequencies (Figure 7-11)

The increase of superficial blood flow (1-2mm [114] below the skin surface) on human facial region upon the onset of emotional stressor is reported recently. The mean blood flow of forehead [114][115] [116] and cheek [115][116] during anxiety state increases, which reveals that the tissue oxygen content (see section 3.5 for details) of those regions is affected by the emotion or the hormone secreted along with emotion.

From all the publications above, at least one point is clear that the anxiety hormone adrenaline or anxiety itself can trigger higher oxygen saturation (content) in certain tissues (including facial tissues), although the increase can be transient or sustained. In the case of very short-term increase,



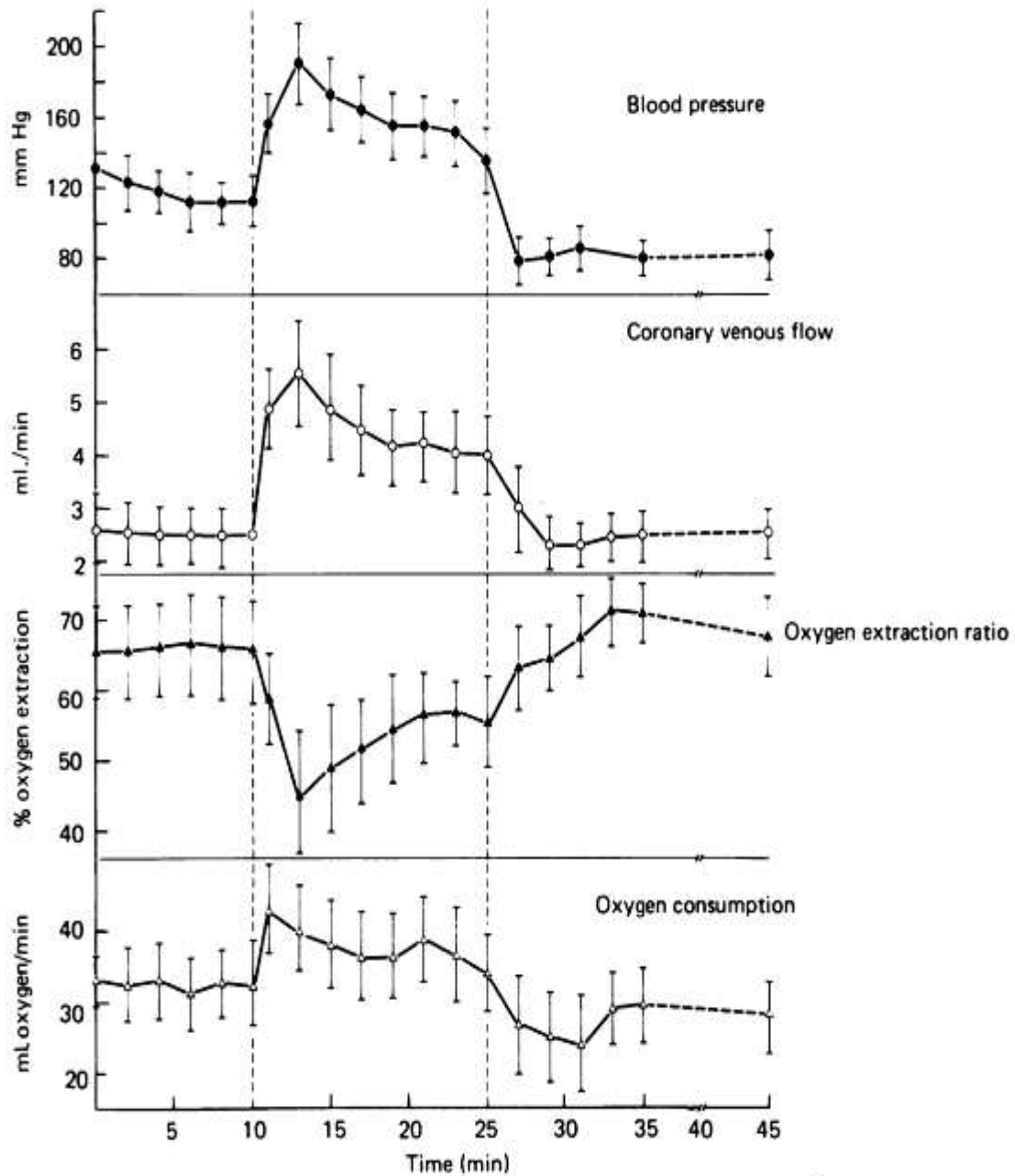


Figure 7-10 shows the variations of blood pressure, coronary venous flow, and oxygen extraction ratio and oxygen consumption of a dog under controlled injections of adrenaline (2ug/kg per min at the arrowed point) in an intravenous infusion experiment [112]. It is observed that an increase of blood pressure by almost 2-fold, together with ~90% increase of oxygen content in the blood while the oxygen consumptions by tissues are seen to remain more or less constant after the adrenaline injection, resulting in an abrupt drop of overall oxygen extraction ratio to almost a half causing a net increase of blood oxygenation ~100 - 200% after the adrenaline injections.

the post-transient response may be influenced by the amount of adrenaline and the severity of the stressor. With the effect of very large amount of adrenaline or sustained stimulation of the adrenal medulla, the higher tissue oxygenation may be maintained.

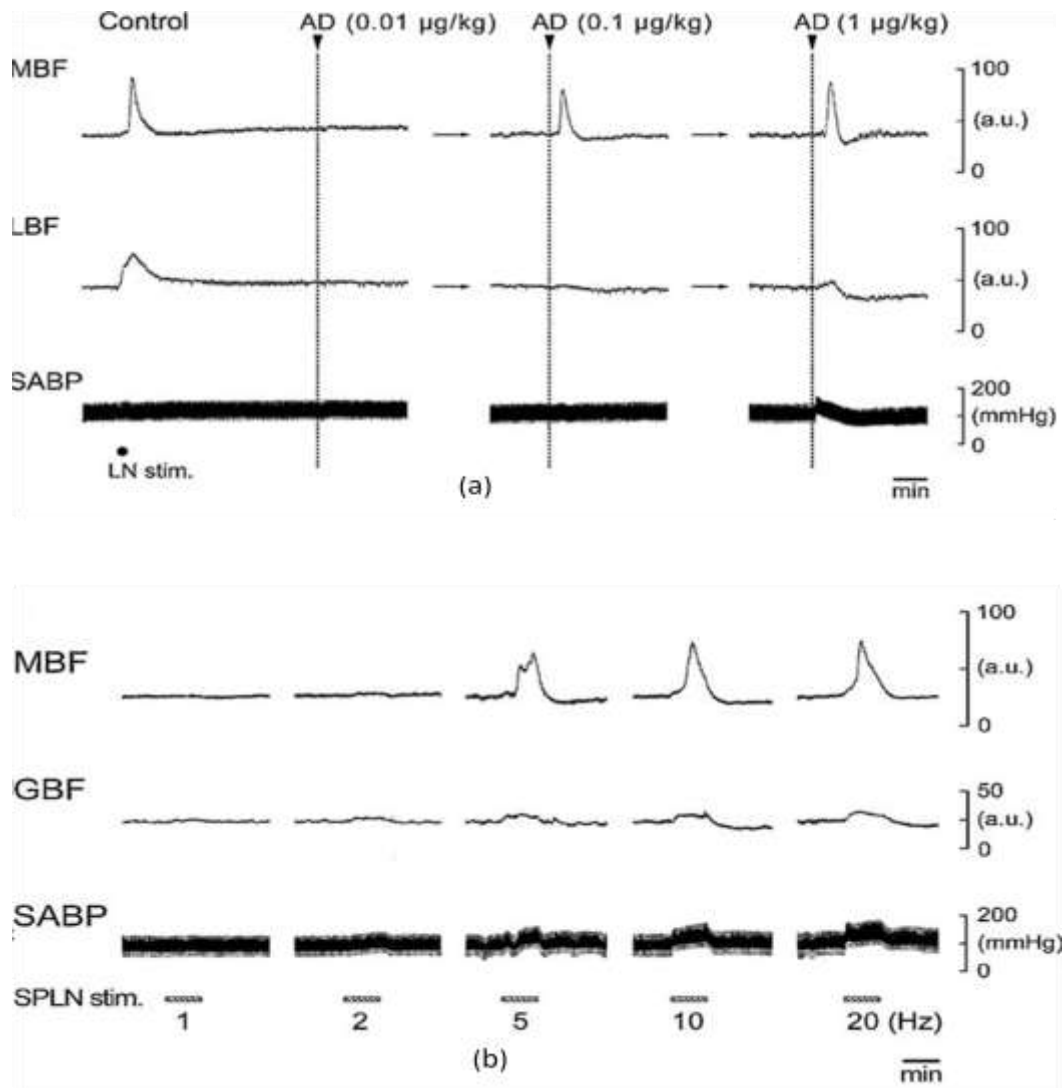


Figure 7-11 (a) MBF is the blood flow of masseter muscle. AD represents adrenaline infusion. The transient increase of masseter blood flow caused by adrenaline is clear both in 0.1 $\mu\text{g/kg}$  and 1 $\mu\text{g/kg}$  dose. The larger dose decreases the blood flow lower than baseline after the initial rise. (b) Electrical stimulation of SPLN nerve with 5Hz, 10Hz, and 20Hz, cause uninterrupted rise of masseter blood flow. [113]

## **8 EMOTION DETECTION BASED ON TISSUE OXYGEN SATURATION**

### **8.1 Introduction**

Emotions and bodily physiological reactions are closely related, although the relationship is complicated and it may not be a one to one correspondence. One purpose of this work is to examine whether the physiological signal of tissue oxygen saturation (StO<sub>2</sub>) can be made use for the detection and/or classification of emotion. This is the first study of its kind [13][14][21] in the area of affective computing, and our approach is in great contrast and perhaps compliment to the conventional methods that use facial expression for emotion classification. One distinct difference between our work with respect to other work in the field is that, we have employed non-involuntary physiological feature, such as StO<sub>2</sub>, for remote sensing of people's emotion for the first time.

This chapter presents the results for using the StO<sub>2</sub> feature to detect the emotions of humans after they are subjected to various emotional and physical stimulations. The study involved 21 subjects and physiological features of StO<sub>2</sub> and heart beat rate (HBR) have been used for monitoring and classification of their emotions. In this study two main kinds of basic emotions have been considered: (1) Calm emotion and (2) Strong emotions specifically distress due to (a) panic and anxiety resulting from psychological pressure and (b) pain or fatigue resulting from physical demands. These two different kinds of emotions in (a) and (b) are denoted as mental strong emotion (MSE) and physical strong emotions (PSE) in this thesis.

All of the work presented in this thesis has been basic research which is required for the fundamental understanding of how physiological feature can be used for remote sensing of people's emotion. Most of the work presented has already been published [13][14].

### **8.2 MSE and PSE**

Three main techniques for inducing MSE in this study have been mental mathematics, public speech, and recognition-memory task. One or all of these

three mental stimulations have been applied to every participant until an arousal of heart beat rate is observed. Every participant is asked to perform mental calculation over 25-30 simple arithmetic and they are required to give answers within tight time scales of ~4-5 seconds. The participants were firstly informed of the expected score before the test in order to impose a psychological pressure to them. The test is designed in such a way that a gradual increase of the difficulty of the question approaching to the middle of the session is introduced, thereby increasing the psychological pressure gradually.

Alternatively a public speech or a presentation is requested to be given by the participants in front of a panel of referee or interviewee. The presentation can be in the form of a job interview or a description of a project.

Finally a memory test will be given to the participants: the task is to remember a set of two images which appears together in the same powerpoint slide. In the learning session a series of pairs of images will be flashed out and each will remain on the TV screen for ~2 seconds. After flashing about 6-10 slides of images, the participants are then requested to identify which two of the five images that appear in a test slide are in a pair that has been flashed out previously. The participants are required to answer each test slide within a time limit of 5 seconds.

The stimulation of PSE can be achieved either by requesting the participants to run two floors of stairs up and down in short periods of 20-30 seconds, or to perform a muscle endurance exercise of doing a half squat like horse stance for 1-2 minutes.

### **8.3 Experimental Procedures and Protocols**

There are 21 healthy volunteers (subjects A-U) recruited from the students and staffs within Cranfield University for the emotion sensing experiment. These participants are from various origins and career background. Among them, there are 19 male and 2 female of students and staffs. The large percentage of male participants involved in this work is due to the constraints in a male dominant institute typically of a defence college, and the gender effect on the

StO<sub>2</sub> response to the MSE and PSE is not known for the moment. The procedures and the protocol of the experiment have been approved by the Ethics Committee. The heart beat rate (HBR) of every participant is monitored throughout the experiment, and the testing sequence in general is as follows:

- A. An explanation of the experimental procedure is firstly given to each participant when they enter into the laboratory. They are then given 5 to 10 minutes of settling time, during which their baseline information, in this case, the HSI data, video and colour pictures, are recorded.
- B. MSE induction like that described in previous section is then given. HSI data are recorded during the test especially at the moments before and after arousal of HBR when they occur during the test session
- C. A rest period of about 10-20 minutes is given after the MSE induction. The HBR of participants is monitored until they return to their base line before the next test proceeds.
- D. The final test involves PSE stimulation as described previously and the HSI data are recorded right after the physical exercise is completed.

## **8.4 Facial StO<sub>2</sub> and Emotion**

The StO<sub>2</sub> result is generated under the EBL3C model (Equation 4-7) using HSI data in the spectral range of [516-580]nm. The final StO<sub>2</sub> map is averaged with a circular averaging filter (see section 6.2) of 3 pixels.

Previous publications in bio-medical field have shown a rise of blood oxygenation in the tissue upon the onset of emotional distress (see section 7.7.2). The present results have shown that all the 21 participants exhibit an increase of StO<sub>2</sub> level in the facial region, particularly at around the forehead region, when they are subjected to MSE stimulation. However, it is not always true in the PSE case and the forehead StO<sub>2</sub> can increase and sometimes even a drop below the base line level when they experience vigorous physical distress.

The facial StO<sub>2</sub> images of three participants are given in Figure 8-1, where the left, middle and right columns represent the facial tissue oxygenation of the

baseline, under MSE and PSE respectively. The HBR of the participant in the moment or recording is shown in the bottom right corner of each image. It is seen that all three participants exhibit an increase of tissue oxygenation in the facial region, particularly at around the forehead and eye socket areas, when they are under MSE stimulation.

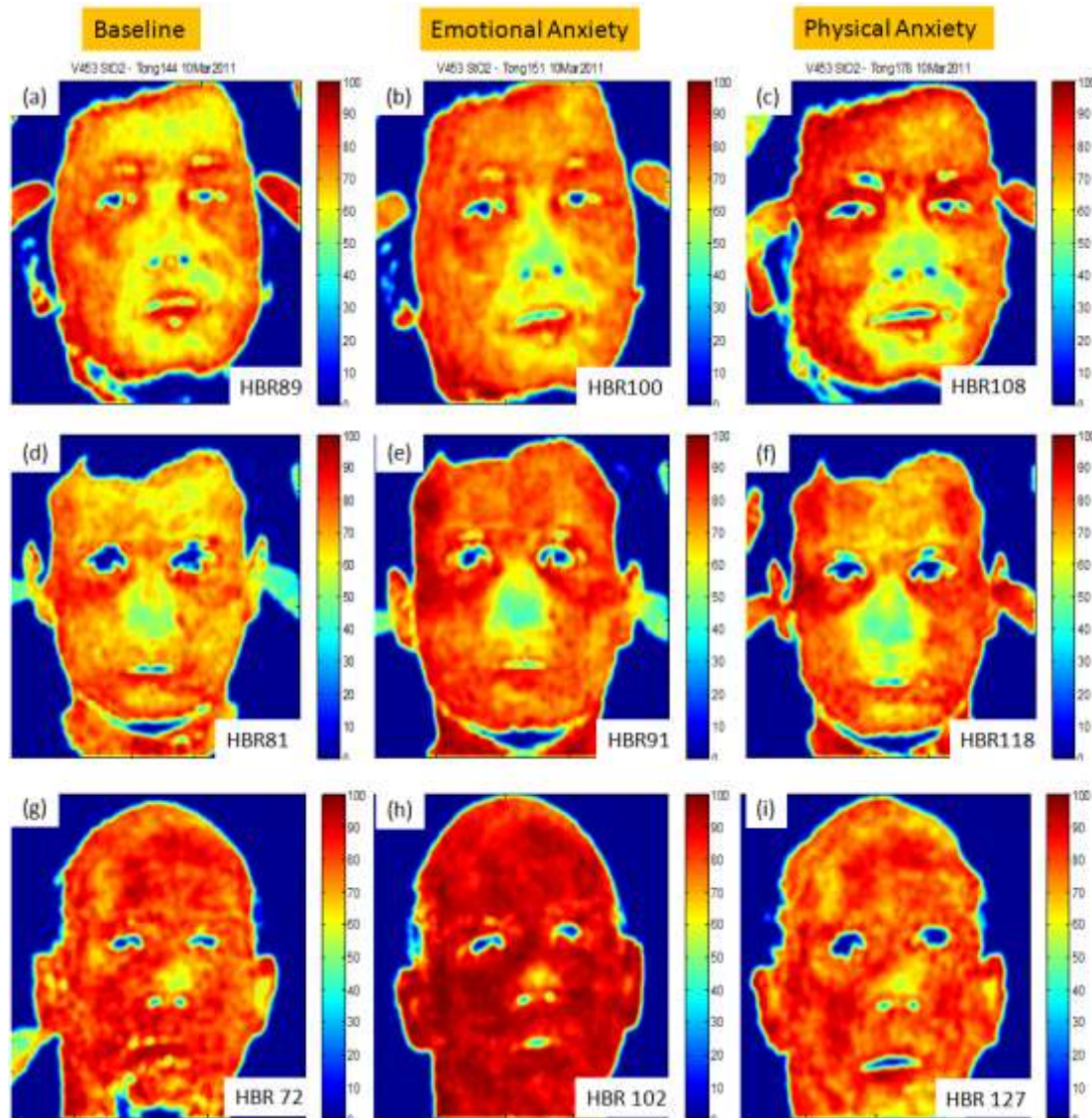
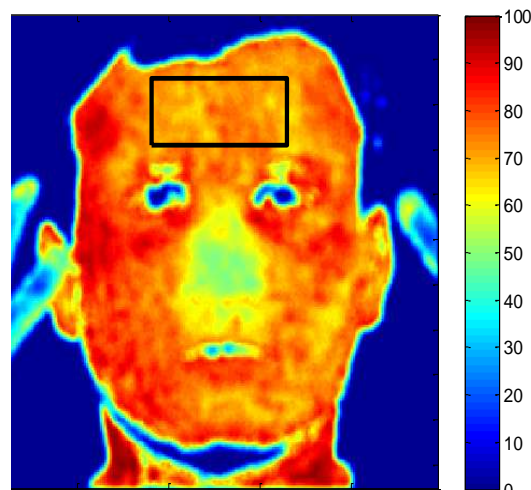


Figure 8-1 shows StO<sub>2</sub> maps of three participants under baseline, MSE, and PSE. (a)Participant A in baseline; (b) Participant A under MSE; (c) Participant A under PSE; (d)Participant B in baseline; (e) Participant B under MSE; (f) Participant B under PSE; (a)Participant O in baseline; (b) Participant O under MSE (c) Participant O under PSE;

However, the tissue oxygenations after PSE stimulation can go up, such as participant A (top row of Figure 8-1 ) and participant B (middle row of Figure 8-1), and it can also reduce as is seen in participant O (bottom row of Figure 8-1) despite of the increased HBR after PSE stimulation.

To investigate how the StO2 level changes due to MSE and PSE, the average StO2 of 11 ROIs in the face have been studied. However, only the StO2 of the foreheads of 21 participants is highlighted here, due to the fact that the other results are not allowed to be released at present. The region of interest (ROI) on the forehead for calculating average StO2 is the centre part of the forehead, and it is shown in Figure 8-2 using a black rectangle.



**Figure 8-2 shows Region of Interests on forehead for generating average StO2 and standard deviation StO2 of forehead.**

The average StO2 of the ROI and its standard deviation, and also the HBR for all participants under MSE stimulation have been summarised in Table 9. Due to the different physique of individuals, the average baseline StO2 of the participants on the forehead spans from as low as 50% (participant M) to as high as 84% (participant O). This diversity of baseline can also be seen from the various HBR readings, which can be as low as 50 (participant F) and as high as 89 (participant A). All the HBRs of the candidates are seen to be increased in the both MSE and PSE stimulations, suggesting positive responses to the stimulations from all the participants.

The rate of the increase in the StO<sub>2</sub> and the HBR as the result of MSE and PSE stimulations are given in Table 10. It is quite clear that all participants response positively to the MSE stimulation, ranging from a minimum elevation rate of StO<sub>2</sub> ~1.5% (participant L) to a maximum of 28% change seen in participant I. However, it is not quite the case for the PSE: only 11 out of 21 participants exhibit an increase of StO<sub>2</sub>. This observation may be related to the different physique of individuals with different blood regulation capabilities, which will directly affects the oxygenation demands and supplies to the working muscle.

**Table 9** tabulates the HBR, the averaged (Avg) StO<sub>2</sub> and its standard deviation (Std) of 21 participants' forehead ROI.

Participant	Baseline			MSE			PSE		
	Avg StO <sub>2</sub> (%)	Std StO <sub>2</sub> (%)	HBR (bps)	Avg StO <sub>2</sub> (%)	Std StO <sub>2</sub> (%)	HBR (bps)	Avg StO <sub>2</sub> (%)	Std StO <sub>2</sub> (%)	HBR (bps)
A	64.14	5.43	89	72.01	3.24	100	74.98	6.50	108
B	65.77	4.18	81	77.04	2.94	91	69.97	4.03	118
C	61.64	5.45	92	67.63	3.02	110	73.58	5.45	120
D	72.52	6.00	69	80.23	5.26	90	82.98	6.97	131
E	73.24	4.14	79	78.60	5.60	87	63.71	4.44	103
F	70.81	4.04	50	73.33	3.51	60	64.53	3.76	110
G	66.69	3.63	71	70.03	3.88	76	66.84	3.89	86
H	68.79	3.26	88	75.46	2.69	91	69.77	3.22	100
I	56.07	5.66	65	71.97	4.01	71	68.29	4.71	82
J	60.16	6.36	89	72.96	4.58	94	58.79	4.35	104
K	77.01	3.83	75	80.96	3.83	85	77.93	3.62	112
L	78.05	4.09	75	79.22	3.28	100	72.18	5.12	110
M	50.10	5.07	75	59.11	5.23	80	50.01	5.73	150
N	75.05	6.96	67	76.54	6.41	73	68.39	8.73	94
O	84.12	4.80	72	90.70	3.12	75	80.03	5.29	127
P	78.29	4.71	80	80.83	4.55	90	72.90	3.72	120
Q	67.25	4.76	65	71.70	4.09	75	76.54	5.18	103
R	68.48	3.26	84	76.72	4.09	100	71.01	5.18	120
S	63.29	3.26	70	71.20	4.37	75	59.48	4.08	110
T	75.96	6.37	75	82.85	4.86	100	76.98	5.51	120
U	68.92	4.93	61	74.98	4.01	77	60.95	5.53	110

Elevation of blood oxygenation is one of the physiological changes of human body in response to the stressor, however, when a person is in the physical excited emotion, the blood flow to the brain can be decreased [117] [118]if the exercise is heavy to the subject and leading to fatigue. Thus the less inflow of blood to the brain can reduce the facial StO<sub>2</sub> to make it lower than that of the



baseline. It is not the same in the case of MSE stimulation where little or no muscle is under physical action, hence more oxygenated blood as the result of the increasing HBR upon MSE stimulation, may be driven to the brain through the forehead regions.

**Table 10 gives the percentages rate of change in HBR and forehead StO2 as the result of MSE and PSE stimulation. Note that the StO2 due to PSE can either drop or rise with respected to the base line.**

Participant	(MSE-Base)/Base		(PSE-Base)/Base	
	Avg StO2	HBR	Avg StO2	HBR
A	12.3%	12.4%	16.9%	21.3%
B	17.1%	12.3%	6.4%	45.7%
C	9.7%	19.6%	19.4%	30.4%
D	10.6%	30.4%	14.4%	89.9%
E	7.3%	10.1%	-13.0%	30.4%
F	3.6%	20.0%	-8.9%	120.0%
G	5.0%	7.0%	0.2%	21.1%
H	9.7%	3.4%	1.4%	13.6%
I	28.3%	9.2%	21.8%	26.2%
J	21.3%	5.6%	-2.3%	16.9%
K	5.1%	13.3%	1.2%	49.3%
L	1.5%	33.3%	-7.5%	46.7%
M	18.0%	6.7%	-0.2%	100.0%
N	2.0%	9.0%	-8.9%	40.3%
O	7.8%	4.2%	-4.9%	76.4%
P	3.2%	12.5%	-6.9%	50.0%
Q	6.6%	15.4%	13.8%	58.5%
R	12.0%	19.0%	3.7%	42.9%
S	12.5%	7.1%	-6.0%	57.1%
T	9.1%	33.3%	1.3%	60.0%
U	8.8%	26.2%	-11.6%	80.3%

If the oxygen consumption rate of the body remains more or less constant during the MSE stimulation, the increase of HBR may induce an increase in the overall StO2 of the body. A scatter plot of the rate of change in StO2 versus the rate of change of HBR under MSE stimulation for all participants is shown in Figure 8-3. It is observed that there is no obvious correlation between these two quantities!

This may be again due to the very distinctive blood regulation mechanisms and physiques of the individuals. If this individual's difference is removed, for example, to plot the rate of change of HBR and StO<sub>2</sub> of the same individual, then a correlation between these two quantities is expected. Unfortunately the number of data points acquired for each participant in this trial is very limited, with three or utmost four HSI images taken for each participant and therefore a plot like figure 8-3 cannot be made at present. The limitation is mainly constraint by the low frame rate of the HSI hardware which cannot record image in real time. More work in the direction of using more sophisticated scattering model together with more advanced HSI hardware is needed.

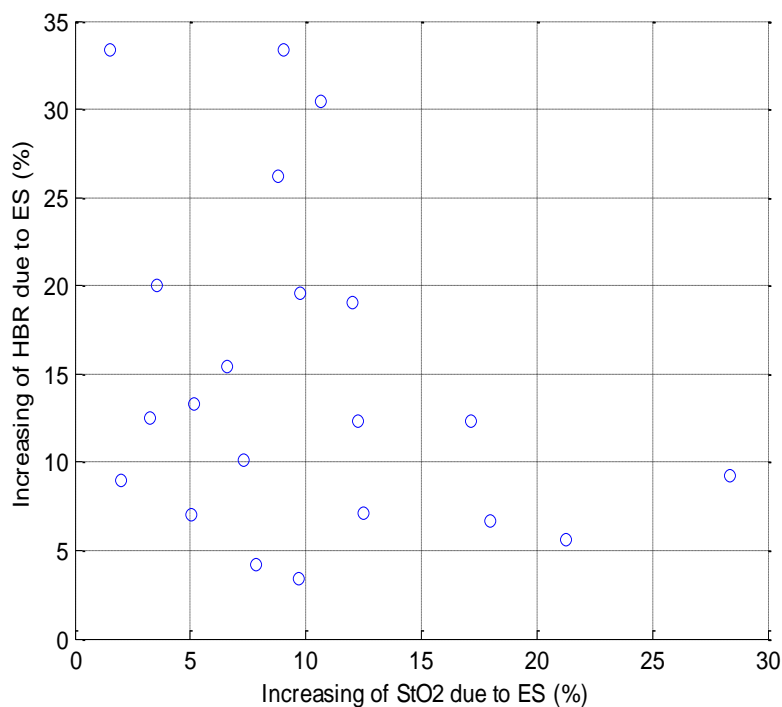


**Figure 8-3 the scatter plot of the rate of change in StO<sub>2</sub> Vs the Increasing-Rate-of-HBR for all participants under MSE stimulation which shows no correlation between these two quantities.**

## 8.5 Conclusion

In this chapter, we have studied how the physiological feature of StO<sub>2</sub> can be made use for the detection and/or classification of strong emotions such as distress caused by mental and physical stressors. The trial consists of 21

participants and the StO<sub>2</sub> of the forehead is evaluated using the ELB3C absorption model. It is found that the StO<sub>2</sub> in the forehead is generally increased in all 21 participants after they are experiencing mentally strong emotion (MSE) stimulation. However, half of the participants exhibit an increase of the StO<sub>2</sub> after physical strong emotion (PSE) stimulation, and the other half show a reduction of blood oxygenation in the forehead. An attempt for correlating the rate of the change of HBR and StO<sub>2</sub> using data of all participants is not successful. This is very likely due to the difference of the individual's physique and health conditions.

In conclusion, this part of the work produces a very first database of human's StO<sub>2</sub> map in the facial region under two different kinds of stressors. The StO<sub>2</sub> feature particularly in the forehead ROI can be a promising feature for the detecting of strong emotions from stand-off distances.



## 9 CONCLUSION AND FUTURE WORK

The objective of this PhD project is to investigate how a specific human physiological feature, namely tissue oxygen saturation (StO<sub>2</sub>), can be assessed by remote sensing techniques and how this feature could be used in the application of detecting human emotion. Hyperspectral Imaging (HSI) technique is employed in this research for measuring StO<sub>2</sub> in stand-off distance based on extended Beer Lambert law model. The design and calibration of HSI system utilised in the research are summarised. The effects of selecting various sub-range wavelengths and different BL model on the StO<sub>2</sub> assessment are investigated, it is found that the EBL3C model in the wavelength region [516-580]nm produces best StO<sub>2</sub> results in respect of best reproducibility and least fitting error. The use of polariser can eliminate the effect of interface reflectance and thus improve the accuracy of StO<sub>2</sub> assessment.

The StO<sub>2</sub> is employed as a feature for stressor-induced emotion detection for the very first time in this research. It is found, from our anxiety test involved 21 participants, that the forehead StO<sub>2</sub> is elevated upon the emotional stressor, and can be either increased or decreased upon physical stressor. It is also confirmed from the data collected that the elevation rate of heart beat rate due to emotional stressor cannot correlate to that of StO<sub>2</sub>.

This PhD project has established an initial data base of diffusive optical scattering from skin, epidermis and dermis layers, over a range of wavelengths for one skin type (Chinese ethnics), and investigated how the StO<sub>2</sub> changes upon the physical and emotional stressor. The future work would include:

- A. Establish database of diffusive optical scattering from skin tissue of various skin type over wavelengths range from visible to short wave near infra-red;
- B. Develop more sophisticated model, such as two-layer skin model, for better understanding the skin diffusive optical scattering towards a more accurate assessment of StO<sub>2</sub>;

- C. Employ Monte Carlo method for more accurately simulating the skin scattering parameters;
- D. Develop robust method for remotely measuring heart beat rate based on broad band HSI data;
- E. Develop robust method for remotely measuring glucose level based on HSI data in short wave near infra-red region;
- F. Employ more physiological features, such as heart beat rate and glucose level, for detecting stressor-induced emotion in a stand-off distance with contactless way.

## REFERENCES

- [1] R. Bezemer, J. M. Karemaker, E. Klijn, D. Martin, K. Mitchell, M. Grocott, M. Heger and C. Ince, "Simultaneous multi-depth assessment of tissue oxygen saturation in the thenar and forearm using near-infrared spectroscopy during a simple cardiovascular challenge," *Critical Care*, vol. 13, no. Suppl5, p. S5, 2009.
- [2] T. Wang and C. Hung, "Role of Tissue Oxygen Saturation Monitoring in Diagnosing Necrotizing Fasciitis of the Lower Limbs," *Annals of Emergency Medicine*, vol. 44, no. 3, pp. 222-228, 2004.
- [3] X. Cheng, J. Mao, R. Bush, D. B. Kopans, R. H. Moore and M. Chorlton, "Breast Cancer Detection by Mapping Hemoglobin Concentration and Oxygen Saturation," *Applied Optics*, vol. 42, no. 31, pp. 6412-6421, 2003.
- [4] J. T. Kuenstner and K. H. Norris, "Near infrared hemoglobinmetry," *J Near Infrared Spectroscopy*, vol. 3, pp. 11-18, 1995.
- [5] G. A. Shaw and H. K. Burke, "Spectral imaging for remote sensing," *Lincoln Laboratory Journal*, vol. 4, no. 1, pp. 3-28, 2003.
- [6] K. J. Zuzak, M. D. Schaeberle and M. T. Gladwin, "Noninvasive Determination of Spatially Resolved and Time-Resolved Tissue Perfusion in Humans during Nitric Oxide Inhibition and Inhalation by Use of a Visible-Reflectance Hyperspectral Imaging Technique," *Circulation*, vol. 104, pp. 2005-2910, 2001.
- [7] V. Tuchin, *Tissue Optics: light scattering methods and instruments for medical diagnosis*, Washington: SPIE, 2007.
- [8] K. J. Zuzak, M. D. Schaeberle, E. N. Lewis and I. W. Levin, "Visible Reflectance Hyperspectral Imaging: Characterization of a Noninvasive, in Vivo System for Determining Tissue Perfusion," *Analytical Chemistry*, vol.

74, no. 9, pp. 2021-2028, 2002.

- [9] K. Zuzak, M. Gladwin, R. Cannon and I. Levin, "Imaging haemoglobin oxygen saturation in sickle cell disease patients using noninvasive visible reflectance hyperspectral techniques: effects of nitric oxide," *Am J Physiol Heart Circ Physiol*, vol. 285, pp. H1183-1189, 2003.
- [10] K. J. Zuzak, S. C. Naik, G. Alexandrakis, D. Hawkins, K. Behbehani and E. H. Livingston, "Characterization of a Near-Infrared Laparoscopic Hyperspectral Imaging System for Minimally Invasive Surgery," *Anal. Chem.*, vol. 79, pp. 4709-4715, 2007.
- [11] J. Edwards, H. J. Jackson and P. E. Pattison, "Emotion recognition via facial expression and affective prosody in schizophrenia: A methodological review," *Clinical Psychology Review*, vol. 22, no. 6, pp. 789-832, 2002.
- [12] B. Fasel and J. Luetttin, "Automatic facial expression analysis: a survey," *Pattern Recognition*, vol. 36, no. 1, pp. 259-275, 2003.
- [13] T. Chen, P. Yuen, K. Hong, A. Tsitiridis, F. Kam, J. Jackman, D. James, M. Richardson, W. Oxford, J. Piper, F. Thomas and S. Lightman, "Remote sensing of stress using Electro-optics imaging technique," in *Proceedings of the SPIE*, 7486, 2009.
- [14] P. Yuen, T. Chen, K. Hong, A. Tsitiridis, F. Kam, J. Jackman, D. James, M. Richardson, W. Oxford, J. Piper, F. Thomas and S. Lightman, "Remote detection of stress using Hyperspectral imaging technique," in *IET Digest, 3rd International Conference on Imaging for Crime Detection and Prevention*, 2009.
- [15] I. Pavlidis, J. Levine and P. Baukol, "Thermal image analysis for anxiety detection pp. 315–318.," in *Proceedings of the 2001 IEEE International Conference on Image Processing*, Thessaloniki, Greece, 2001.



- [16] I. Pavlidis and J. Levine, "Thermal image analysis for polygraph testing," *IEEE Engineering in Medicine and Biology Magazine*, vol. 21, no. 6, pp. 56-64, 2002.
- [17] P. W. Yuen and M. Richardson, "An introduction to hyperspectral imaging and its application for security, surveillance and target acquisition," *The Imaging Science Journal*, vol. 58, no. 5, pp. 241-253, 2010.
- [18] R. B. Smith, "Introduction to Hyperspectral Imaging," 5 Jan 2012. [Online]. Available: <http://www.microimages.com>. [Accessed April 2012].
- [19] P. Yuen and G. Bishop, "Hyperspectral multiple approach fusion for the long-range detection of low observable objects: MUF2," in *Proceedings of the SPIE, Volume 6396*, 2006.
- [20] F. Vagni, "Survey of Hyperspectral and Multispectral Imaging Technologies, Volume TR-SET-065-P3," Research and Technology Organisation, North Atlantic Treaty Organisation, BP 25, F-92201 Neuilly-sur-Seine Cedex,, 2007.
- [21] P. Yuen, T. Chen, K. Hong, A. Tsitiridis and F. Kam, "Final report on the feasibility study remote sensing of intent using Electro-Optics technique Final CTC report contract DSTLX-1000013688.," Final CTC report contract DSTLX-1000013688, 2009 .
- [22] T. L. Troy and S. N. Thennadil, "Optical Properties of Human Skin in the Near Infrared Wavelength Range of 1000 to 2200nm," *J. Biomed. Opt.*, vol. 6, pp. 167-176, 2001.
- [23] H. Ding, J. Q. Lu, W. A. Wooden and X. H. H. P. J. Kragel, "Refractive indices of human skin tissues at eight wavelengths and estimated dispersion relations between 300 and 1600nm," *Physics in Medicine and Biology*, vol. 51, pp. 1479-1489, 2006.
- [24] Y. Lee and K. Hwang, "Skin thickness of Korean adults," *Surgical and*

*Radiologic Anatomy*, vol. 24, no. 3-4, pp. 183-189, 2002.

- [25] R. Logan, "The Structure of Your Skin," 2007. [Online]. Available: <http://www.natural-skin-health.com/skinstructure.html>. [Accessed April 2012].
- [26] S. Prahl, "Optical Absorption of Hemoglobin," Oregon Medical Laser Center, 15 Dec 1999. [Online]. Available: <http://omlc.ogi.edu/spectra/hemoglobin/>. [Accessed 20 March 2012].
- [27] TheFreeDictionary, "Oxygen-haemoglobin dissociation curve," [Online]. Available: <http://encyclopedia.thefreedictionary.com/Oxygen-haemoglobin+dissociation+curve>. [Accessed 7 March 2012].
- [28] J. Swan, "The circulation," 2007. [Online]. Available: <http://classvideos.net/anatomy/pdf/circulation-pdf.pdf>. [Accessed 7 March 2012].
- [29] B. Grassi, L. B. Gladden and M. Samaja, "Faster adjustment of O<sub>2</sub> delivery does not affect VO<sub>2</sub> on-kinetics in isolated in situ canine muscle," *J Appl Physiol*, vol. 85, pp. 1394-1403, 1998.
- [30] W. N. Stainsby and A. B. Otis, "Blood flow, blood oxygen tension, oxygen uptake, and oxygen transport in skeletal muscle," *Am J Physiol*, vol. 206, pp. 858-866, 1964.
- [31] F. Torella, S. L. Haynes and C. N. McCollum, "Cerebral and Peripheral Oxygen Saturation during Red Cell Transfusion," *Journal of Surgical Research*, vol. 110, p. 217–221, 2002.
- [32] N. P. J. Day, N. H. Phu and D. P. Bethell, "The effects of dopamine and adrenaline infusions on acid-base balance and systemic haemodynamics in severe infection," *Lancet*, vol. 348, pp. 219-223, 1996.
- [33] A. Jubran, "Pulse oximetry," *Critical Care*, vol. 3, no. 2, pp. 11-17, 1999.

- [34] M. Wolf, K. Siebenthal, M. Keel, V. Dietz, O. Baenziger and H. U. Bucher, "Tissue oxygen saturation measured by near infrared spectrophotometry correlates with arterial oxygen saturation during induced oxygenation changes in neonates," *Physiol. Meas.*, vol. 21, pp. 481-491, 2000.
- [35] P. Rasmussen, E. A. Dawson, L. N. Johannes, J. Lieshout, N. H. Secher and A. Gjedde, "Capillary-oxygenation-level-dependent near infrared spectrometry in frontal lobe of humans," *Journal of Cerebral Blood Flow & Metabolism*, vol. 27, no. 5, pp. 1082-93, 2007.
- [36] C. L. Ives, D. K. Harrison and G. S. Stansby, "Tissue oxygen saturation, measured by near-infrared spectroscopy, and its relationship to surgical-site infections," *British Journal of Surgery* , vol. 94, pp. 87-91, 2007.
- [37] K. D. Wolff, C. Marks, B. Uekermann, M. Specht and K. H. Frank, "Monitoring of flaps by measurement of intracapillary haemoglobin oxygenation with EMPHO II: experimental and clinical study," *British Journal of Oral and Maxillofacial Surgery*, vol. 34, pp. 524-529, 1996.
- [38] R. A. Shaw, J. R. Mansfield, V. V. Kupriyanov and H. H. Mantsch, "In vivo optical/near-infrared spectroscopy and imaging of metalloproteins," *Journal of Inorganic Biochemistry* , vol. 79, pp. 285-293, 2000.
- [39] D. Yudovsky, A. Nouvong, K. Schomacker and L. Piloni, "Assessing diabetic foot ulcer development risk with hyperspectral tissue oximetry," *Journal of Biomedical Optics* , vol. 16, no. 2, p. 026009, 2011.
- [40] V. Assendelft, *Spectrophotometry of Haemoglobin Derivatives*, Assen, Netherlands: Koninklijke Van Gorcum & Comp. NV, 1970.
- [41] L. C. Cancio, A. I. Batchinsky and J. R. Mansfield, "Hyperspectral imaging: A new approach to the diagnosis of hemorrhagic shock," *The Journal of Trauma: Injury, Infection, and Critical Care*, vol. 60, no. 5, pp. 1087-1095, 2006.

- [42] S. Wray, M. Cope, D. T. Delpy, J. S. Wyatt and E. O. Reynolds, "Characterization of the near infrared absorption of cytochrome aa3 and haemoglobin for the non-invasive monitoring of cerebral oxygenation," *Biochim. Biophys. Acta Bioenerget*, vol. 933, no. 1, pp. 184-192, 1988.
- [43] A. P. Harris, M. J. Sendak, R. T. Donham, M. Thomas and D. Duncan, "Absorption characteristics of human fetal hemoglobin at wavelengths used in pulse oximetry," *J. Clin. Monitor. Comput.*, vol. 4, no. 3, pp. 175-177, 1987.
- [44] S. Takatani and D. Graham, "Theoretical analysis of diffuse reflectance from a two-layer tissue model," *IEEE Trans. Biomed. Eng.*, vol. 26, no. 12, pp. 656-664, 1979.
- [45] D. Yudovsky, A. Nouvong and L. Pilon, "Hyperspectral Imaging in Diabetic Foot Wound Care," *Journal of Diabetes Science and Technology*, vol. 4, no. 5, pp. 1099-1113, 2010.
- [46] M. Garbey, A. Merla and I. Pavlidis, "Estimation of blood flow speed and vessel location from thermal video," in *Proceedings of the IEEE Computer Society Conference on Computer Vision and Pattern Recognition*, Washington D.C., 2004.
- [47] I. Fujimasa, T. Chinzei and I. Saito, "Converting Far Infrared Image Information to Other Physiological Data," *IEEE Engineering in Medicine and Biology Magazine*, vol. 19, no. 3, pp. 71-76, 2000.
- [48] Z. Xie, G. Liu, S. Wu, Z. Fang and G. Yun, "A novel infrared face recognition method in DCT domain," in *Proceedings of the 2010 International Conference on Wavelet Analysis and Pattern Recognition*, Qingdao, 2010.
- [49] G. M. Palmer, A. N. Fontanella, G. Zhang, G. Hanna, C. L. Fraser and M. W. Dewhirst, "Optical imaging of tumor hypoxia dynamics," *Journal of*

*Biomedical Optics*, vol. 15, no. 6, p. 066021, 2010.

- [50] S. Choe, A. P. Acharya, B. G. Keselowsky and B. S. Sorg, "Intravital microscopy imaging of macrophage localization to immunogenic particles and co-localized tissue oxygen saturation," *Acta Biomaterialia* , vol. 6, no. 9, pp. 3491-3498, 2010.
- [51] S. L. Best, A. Thapa, M. J. Holzer, N. Jackson, S. A. Mir, J. A. Cadeddu and K. J. Zuzak, "Minimal Arterial In-flow Protects Renal Oxygenation and Function During Porcine Partial Nephrectomy: Confirmation by Hyperspectral Imaging," *Urology*, vol. 78, no. 4, pp. 961-966, 2011.
- [52] A. Nouvong, B. Davis, B. Hoogwerf, A. tajaddini, E. Mohler and E. Medenilla, "Evaluation of Diabetic Foot Ulcer Healing With Hyperspectral Imaging of Oxyhemoglobin and Deoxyhemoglobin," *Diabetes care* , vol. 32, no. 11, pp. 2056-2061, 2009.
- [53] L. Leonardi, M. G. Sowa, J. R. Payette and H. H. Mantsch, "Near-infrared spectroscopy and imaging: a new approach to assess burn injuries," *Am Clin Lab.*, vol. 19, no. 8, pp. 20-2, 2000.
- [54] W. T. KNOEFEL, N. KOLLIAS, D. W. RATTNER, N. S. NISHIOKA and A. L. WARSHAW, "Reflectance spectroscopy of pancreatic microcirculation," *J.Appl. Physiol.* , vol. 80, no. 1, pp. 116-123, 1996.
- [55] K. J. Zuzak, R. P. Francis, E. F. Wehner, J. Smith, M. Litorja, D. W. Allen, C. Tracy, J. Cadeddu and E. Livingston, "Hyperspectral Imaging Utilizing LCTF and DLP Technology for Surgical and Clinical Applications," in *Proc of SPIE 7170*, 2009.
- [56] D. T. Delpy, M. Cope, V. Zee, S. Arridge, S. Wray and J. Wyatt, "Estimation of optical path length through tissue from direct time of flight measurements," *Phys. Med. Biol.*, vol. 33, pp. 1433-42, 1988.
- [57] A. Sassaroli and S. Fantini, "Comment on the modified Beer–Lambert law

for scattering media,” *Phys. Med. Biol.*, vol. 49, p. N255–N257, 2004.

- [58] M. Kohl, C. Nolte, H. R. Heekeren, S. Horst, U. Scholz, H. Obrig and A. Villringer, “Determination of the wavelength dependence of the differential pathlength factor from near-infrared pulse signals,” *Phys. Med. Biol.*, vol. 43, p. 1771–1782, 1998.
- [59] R. Huang and S. Jacques, “Skin optics summary,” 1998. [Online]. Available: <http://omlc.orgi.edu/news/jan98/skinoptics.html>. [Accessed 20 March 2012].
- [60] D. Hattery, M. Hassan, S. Demos and A. Gandjbakhche, “Hyperspectral Imaging of Kaposi’s Sarcoma for Disease Assessment and Treatment Monitoring,” in *AIPR 2002 Proceedings 31st Applied Imagery Pattern Recognition Workshop From color to Hyperspectral: Advancements in Spectral Imagery Exploitation*, 2002.
- [61] S. Jacques, “Optical Absorption of Melanin,” Oregon Medical Laser Center, 2001. [Online]. Available: <http://omlc.orgi.edu/spectra/melanin/index.html>. [Accessed April 2011].
- [62] G. M. Smith and E. J. Milton, “The use of the empirical line method to calibrate remotely sensed data to reflectance,” *International Journal of Remote Sensing*, vol. 20, no. 13, pp. 2653-2662, 1999.
- [63] V. V. Barun, A. P. Ivanov, A. V. Volotovskaya and V. S. Ulashchik, “Absorption Spectra and Light Penetration Depth of Normal and Pathologically Altered Human Skin,” *Journal of Applied Spectroscopy*, vol. 74, no. 3, pp. 430-439, 2007.
- [64] R. Splinter and B. A. Hooper, *An introduction to biomedical optics*, Taylor & Francis, New York: Taylor & Francis, 2007.
- [65] K. Zuzak, R. Francis, J. Smith, C. Tracy, J. Cadeddu and E. Livingston, “Novel hyperspectral imager aids surgeons SPIE Newsroom,” in *SPIE*

Newsroom DOI: 10.1117/2.1200812.1394, 31 December 2008.

- [66] S. A. Shafer, "Using color to separate reflection components," *Color research and application*, vol. 10, no. 4, pp. 210-218, 1985.
- [67] K. Hong, P. Yuen, T. Chen, A. Tsitiridis and F. Kam, "Detection and classification of stress using thermal imaging technique," in *SPIE European Symposium on Optics/Photonics in Security & Defence, ESD09-SD110-16*, 2009.
- [68] NatrualTech, "The adrenal stress profile Available at:," 2010. [Online]. Available: [http://www.natratech.com/Products/saliva\\_test.htm](http://www.natratech.com/Products/saliva_test.htm) . [Accessed 7 March 2012].
- [69] G. F. Read, "Immunoassays of steroids in saliva," in *proceedings of the Ninth Tenovus Workshop*, Cardiff, 1982.
- [70] I. S. Federenko, M. Nagamine and D. H. Hellhammer, "The heritability of hypothalamus pituitary adrenal axis responses to psychosocial stress is context dependent," *The Journal of Clinical Endocrinology & Metabolism*, vol. 89, no. 12, pp. 6244-6250, 2004.
- [71] B. M. Kudielka, Kieschbaum and C, "Sex differences in HPA axis response to stress: a review.," *Biological Psychology*, vol. 69, pp. 113-132, 2004.
- [72] B. M. Kudielka, S. N. C and D. H. Hellhammer, "Acute HPA axis responses, heart rate and mood changes to psychosocial stress (TSST) in humans at different times of day," *Psychoneuroendocrinology*, vol. 29, p. 983-992, 2004.
- [73] M. D. Sauro, "A study on the effects of sociotropic cognition and dysphoric mood on cardiovascular, hormonal, affect, and memory response in young women," *Dissertation Abstracts International*, 4830B (UMI No. AA13029972)., vol. 62, no. 10, 2002.

- [74] R. M. Condren, A. O'Neill and M. C. M. Ryan, "HPA axis response to a psychological stressor in generalized social phobia.," *Psychoenuroendocrinology*, vol. 27, p. 693–703, 2002.
- [75] J. W. Berry and E. L. Worthington, "Forgivingness, relationship quality, stress while imagining relationship events, and physical and mental health," *Journal of Counseling Psychology*, vol. 48, pp. 447-455, 2001.
- [76] S. S. Dickerson and M. E. Kemeny, "Acute stressors and cortisol response: a theoretical integration and synthesis of laboratory research," *Psychological Bulletin*, vol. 130, no. 3, pp. 355-391, 2004.
- [77] F. A. Kozel and K. A. Johnson, "Detecting deception using functional magnetic resonance imaging," *BIOL PSYCHIATRY*, vol. 58, pp. 605-613, 2005.
- [78] M. Bles and J.-D. Haynes, "Detecting concealed information using brain imaging technology," *Neurocase: The Neural Basis of Cognition*, vol. 14, no. 1, pp. 82-92, 2008.
- [79] S. Bhatt, J. Mbwana, A. Adeyemo, A. Sawyer, A. Hailu and J. VanMeter, "Lying about facial recognition: An fMRI study," *Brain and Cognition* , vol. 69, pp. 382-390, 2009.
- [80] F. A. Kozel, K. A. Johnson, E. L. Grenesko, S. J. Laken, S. Kose, X. Lu, D. Pollina, A. Ryan and M. S. George, "Functional MRI detection of deception after committing a mock sabotage crime," *Forensic science*, vol. 54, no. 1, pp. 220-231, 2009.
- [81] A. Madrigal, "WIRED SCIENCE," 16 March 2009. [Online]. Available: <http://www.wired.com/wiredscience/2009/03/noliemri/>. [Accessed 5 March 2012].
- [82] M. Valstar, I. Patras and M. Pantic, "Facial action unit recognition using temporal templates," in *IEEE International Workshop on Human-Robot*



*Interaction*, 2004.

- [83] L. Zhang, Y. Tong and Q. Ji, "Interactive labeling of facial action units," in *19th International Conference on Pattern Recognition*, 2008.
- [84] Y. Tong, W. Liao and Q. Ji, "Facial action unit recognition by exploiting their dynamic and semantic relations," *IEEE Transactions on Pattern Analysis and Machine Intelligence*, vol. 29, no. 10, pp. 1682-1699, 2007.
- [85] P. Ekman, W. V. Friesen and J. C. Hager, *Facial action coding system the manual*, Salt Lake City: A Human Face, 2002.
- [86] J. Healey and R. Picard, "SmartCar: Detecting Driver Stress," in *15th International Conference on Pattern Recognition*, 2000.
- [87] J. Zhai and A. B. Barreto, "Realization of stress detection using psychophysiological signals for improvement of human-computer interactions," in *SoutheastCon Proceedings IEEE*, 2005.
- [88] K. H. Kim, S. W. Bang and S. R. Kim, "Emotion recognition system using short-term monitoring of physiological signals," *Med. Biol. Eng. Comput.*, vol. 42, pp. 419-427, 2004.
- [89] C. McCauley and R. F. Forman, "A Review of the Office of Technology Assessment Report on Polygraph Validity," *Basic and Applied Social Psychology*, vol. 9, no. 2, pp. 73-84, 1998.
- [90] "Scientific Validity of Polygraph Testing: A Research Review and Evaluation—A Technical Memorandum," (Washington, D. C.: U.S. Congress, Office of Technology Assessment, OTA-TM-H-15, November 1983)..
- [91] I. Pavlidis, J. Levine and P. Baukol, "Thermal Imaging for Anxiety Detection'," in *IEEE workshop on Computer Vision Beyond the Visible Spectrum: Methods and Applications*, 2000.

- [92] I. Pavlidis, N. Eberhardt and J. Levine, "Human behavior: Seeing through the face of deception," *nature*, vol. 415, no. 687, p. 35, 2002.
- [93] I. Pavlidis and J. Levine, "Monitoring of periorbital blood flow rate through thermal image analysis and its application to polygraph testing," in *Proceedings of the 23rd Annual International Conference of the IEEE Engineering in Medicine and Biology Society*, Istanbul, Turkey, 2001.
- [94] J. A. Levine, I. T. Pavlidis, L. MacBride, Z. Zhu and P. Tsiamyrtzis, "Description and clinical studies of device for the instantaneous detection of office-place stress," *Work*, vol. 34, no. 3, pp. 359-364, 2009.
- [95] I. Pavlidis, "Continuous physiological monitoring," in *Proceedings of the 25th Annual International Conference of the IEEE Engineering in Medicine and Biology Society*, Cancun, Mexico , 2003.
- [96] C. Puri, L. Olson, I. Pavlidis, J. Levine and J. Starren, "Stresscam:non-contact measurement of users' emotional states through thermal imaging," in *Proceedings of the 2005 ACM Conference on Human Factors in Computing Systems( CHI)*, Portland, 2005.
- [97] P. TSIAMYRTZIS, J. DOWDALL, D. SHASTRI, I. PAVLIDIS, M. FRANK and P. EKMAN, "Imaging Facial Physiology for the Detection of Deceit," *International Journal of Computer Vision*, vol. 71, no. 2, pp. 197-214, 2007.
- [98] K. Kuraoka and K. Nakamura, "The use of nasal skin temperature measuremnet in studying emotion in macaque monkeys," *Physiology & Behavior*, vol. 102, pp. 347-355, 2011.
- [99] K. Nakayama, S. Goto, K. Kuraoka and K. Nakamura, "Decrease in nasal temperature of rhesus monkeys (*Macaca mulatta*) in negative emotional state," *Physiology & Behavior*, vol. 84, pp. 783-790, 2005.
- [100] M. Stewart, J. Webster, G. Verkerk, A. Schaefer, J. Colyn and K. Stafford,

“Non-invasive measurement of stress in dairy cows using infrared thermography,” *Physiology & Behavior*, vol. 92, pp. 520-525, 2007.

[101] D. M. L. Vianna and P. Carrive, “Changes in cutaneous and body temperature during and after conditioned fear to context in the rat,” *European Journal of Neuroscience*, vol. 21, pp. 2505-2512, 2005.

[102] I. Pavlidis, J. Dowdall, N. Sun, C. Puri, J. Fei and M. Garbey, “Interacting with human physiology,” *Computer vision and image understanding*, vol. 108, pp. 150-170, 2007.

[103] N. Sun, M. Garbey, A. Merla and I. Pavlidis, “Imaging the cardiovascular pulse,” in *Proceedings of the IEEE Computer Society Conference on Computer Vision and Pattern Recognition*, San Diego, CA, 2005.

[104] T. R. Gault, N. Blumenthal, A. A. Farag and T. Starr, “Extraction of the superficial facial vasculature, vital signs waveforms and rates using thermal imaging,” in *Computer vision and pattern recognition workshop, 2010 IEEE computer society conference on*, 2010.

[105] J. Fei, Z. Zhu and I. Pavlidis, “Imaging breathing rate in the CO<sub>2</sub> absorption band,” in *Proceedings of the 27th Annual International Conference of the IEEE Engineering in Medicine and Biology Society*, Shanghai, 2005.

[106] S. Jarlier, D. Grandjean, S. Delplanque, K. N'Diaye, I. Cayeux, M. I. Velazco, D. Sander, P. Vuilleumier and K. R. Scherer, “Thermal analysis of facial muscles contractions,” *IEEE transactions on affective computing*, vol. 2, no. 1, pp. 2-9, 2011.

[107] B. L. Seaward, *Managing stress: principles and strategies for health and well-being*. 5th ed., London: Jones&Bartlett, 2005.

[108] E. A. Randolfi, “The Psychophysiology of Stress Part II,” April 2007. [Online]. Available:

<http://www.msubillings.edu/cahpfaculty/randolfi/436/psychphys2.html>.  
[Accessed 2011].

- [109] Wikipedia, "Peripheral nervous system," [Online]. Available: [http://en.wikipedia.org/wiki/Peripheral\\_nervous\\_system](http://en.wikipedia.org/wiki/Peripheral_nervous_system). [Accessed 2011].
- [110] F. Jones, J. Bright and A. Clow, "Stress: myth, theory, and research," London, Prentice Hall, 2001.
- [111] S. L. Skinner and R. F. Whelan, "Skinner S. L., and Whelan R. F., The circulation in forearm skin and muscle during adrenaline infusions," *Austral. J. exp. Biol.*, vol. 40, pp. 163-172, 1962.
- [112] M. S. Creates and J. Grayson, "THE EFFECT OF ADRENALINE AND NORADRENALINE ON CORONARY VASCULAR RESERVE IN THE DOG," *J. Physiol.*, vol. 309, pp. 557-568, 1980.
- [113] H. Ishii, T. Niioka and H. Izumi, "Circulating adrenaline released by sympathoadrenal activation elicits acute vasodilatation in the rat masseter muscle," *Archives of Oral Biology*, vol. 54, pp. 486-494, 2009.
- [114] P. D. Drummond, "The effect of adrenergic blockade on blushing and facial flushing," *Psychophysiology*, vol. 34, pp. 163-168, 1997.
- [115] P. D. Drummond, "The effect of anger and pleasure on facial blood flow," *Australian Journal of Psychology*, vol. 46, pp. 95-99, 1994.
- [116] P. D. Drummond and J. W. Lance, "Facial flushing and sweating mediated by the sympathetic nervous system," *Brain*, vol. 110, p. 793– 803, 1987.
- [117] S. Ogoh and P. N. Ainslie, "Cerebral blood flow during exercise: mechanisms of regulation," *J Appl Physiol*, vol. 107, pp. 1370-1380, 2009.
- [118] J. T. Olin, A. C. Dimmen, A. W. Subudhi and R. C. Roach, "Cerebral blood flow and oxygenation at maximal exercise: The effect of clamping carbon

dioxide," *Respiratory Physiology & Neurobiology*, vol. 175, no. 1, pp. 176-180, 2011.



## APPENDICES

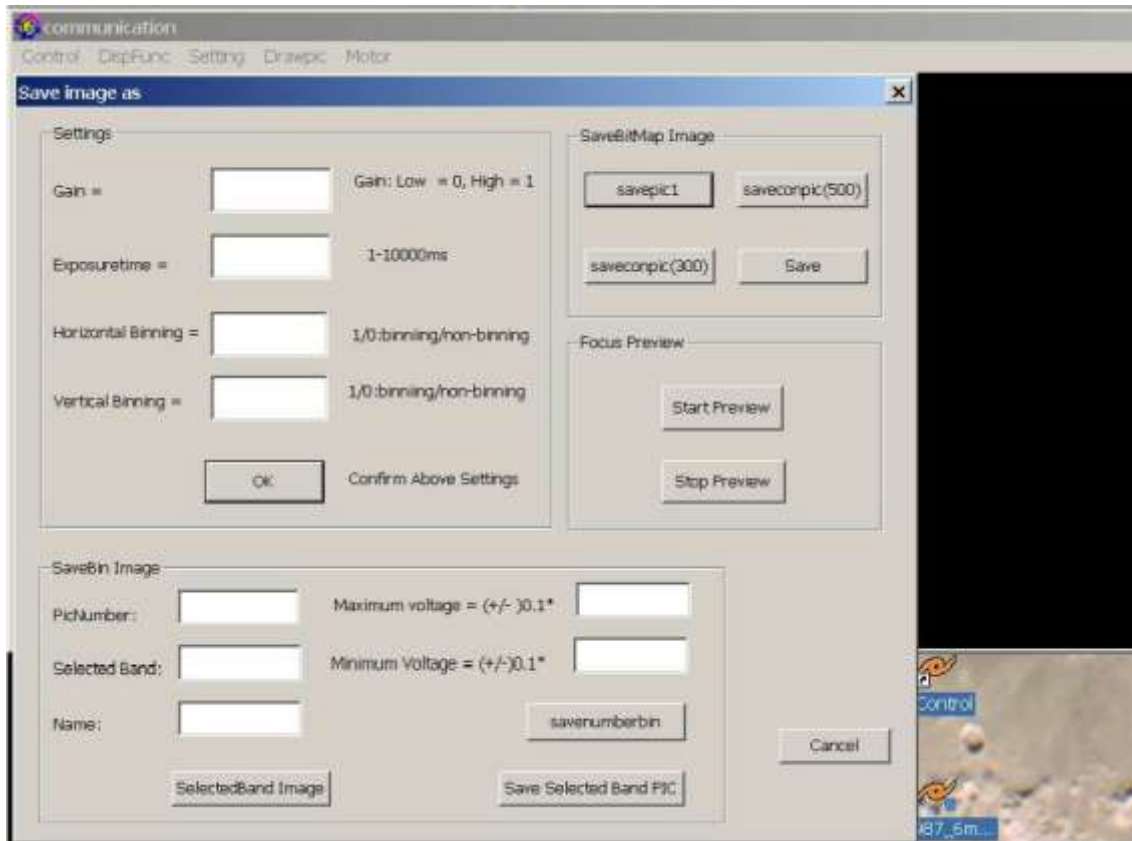
### Appendix A VNIR\_3.0@Cranfield

#### A.1 GUI

The graphic user interface (GUI) of VNIR\_3.0 merges the *Settings* GUI and *Capture Image* GUI of VNIR\_1.0 and includes new group-box *Focus Preview*. Figure\_Apx A-1 illustrates what the GUI of VNIR\_3.0 looks like. The control panel 'Save image as' is for setting parameters for camera control, building hyperspectral cube, and preview. Behind the control panel 'Save image as' is the display window for preview and focusing purpose, on which a 2D spatial image in a selected band is shown. The buttons and edit boxes are explained as below:

##### A. Settings group-box

1. Gain (edit box): the input can be '1' or '0', which understood by camera as high gain or low gain settings. Under high gain setting, all the pixel values of every frame are multiplied by a constant. While, under low gain setting, the pixel values keep unchanged.
2. Exposure time (edit box): the input can be any integer in the range of the 1 to 10000. The unit of the input is milliseconds.
3. Horizontal Binning (edit box): the input can be '1' or '0'. To bin the output frame of camera, an input '1' is required. An input of '0' means not to bin the frame. The CCD of the VNIR camera is of size 1932by1024. To bin the frame horizontally reduces the output frame into 696by1024.
4. Vertical Binning (edit box): the input can be '1' or '0'. An input '1' means to bin the output frame, input '0' means not to bin. To bin the frame vertically reduces the output frame into 1392by512.
5. OK (press button): Pressing this button confirms the settings above.



**Figure\_Apx A-1 GUI of VNIR\_3.0. The control panel is on the top layer, and the window for display purpose is on the second layer.**

## B. SaveBin Image group-box

1. Maximum Voltage (edit box): the input can be any integer from -50 to 50. The voltage to the motor determines the position of mirror attached to the motor. A 0 voltage input to the motor makes the angle between the mirror surface and the horizon 45°, so that the camera sees horizontally. A positive voltage input to the motor makes the angle between the mirror surface and the horizon larger than 45°, and a minus voltage makes the angle smaller than 45°. The actual maximum voltage value to the motor is the input maximum value divided by 10. Any input value larger than 50 is set to 50.

2. Minimum Voltage (edit box): the input can be any integer from -50 to 50. The actual minimum voltage value to the motor is the input minimum value divided by 10. Any input value smaller than -50 is set to -50. In the case of input minimum voltage is larger than input maximum voltage, error message pops up.



3. PicNumber (edit box): the input can be any integer in the range of 1 to 600. Under the condition that both horizontal and vertical binning are set to 1, the input can be any integer from 1 to 1200. The input value determines the number of frames for building a hyperspectral image cube.
4. Selected Band (input text): the input can be any integer in the range of 1-1024 when Vertical Binning is set as '0', and in the range of 1-512 when Vertical Binning is set as '1'. The input value determines the waveband, in which a 2D spatial image is shown.
5. Name (edit box): the input is the file name of the hyperspectral image cube. If the name keeps unchanged, such as 'test', then the first image cube will be named as 'test0', and second image cube is named as 'test1', and so on. All the image cubes with given names are stored in a specific data file for easily retrieving later.
6. savenumberbin (press button): pressing this button makes the imaging system begin to build hyperspectral image cube with specified size, to display in realtime a 2D spatial image in a selected waveband on the display window, and to store the hyperspectral image cube with a specified name in the hard disk of PC.
7. SelectedBand Image (press button): pressing this button makes a 2D spatial image in the selected waveband displayed on the display window. This button is expected to be pressed after the hyperspectral image cube is made. The input to the SelectedBand text affects the display result.
8. Save Selected Band PIC (press button): pressing this button makes the 2D spatial image in the selected band is saved, a pop-up window will appear to guide the save procedure.

#### C. Focus Preview group-box

1. Start Preview (press button): pressing this button starts a focus session.
2. Stop Preview (press button): pressing this button stops the focus session.  
(Detailed description are given in the paragraph followed)

#### D. SaveBitMap Image group-box

This group of buttons are for test only.

### A.2 Input Voltage Range Selection

The voltage output to motor in VNIR\_1.0 has to be from positive to minus value, with +5 V corresponding to +30° and -5V to -30°. The limitation of the input option makes the situation impossible where the scanner needs to begin from zero or minus degree. In VNIR\_3.0, the fourth argument of function *GetDigtItemInt* is changed into TRUE, so that the input voltage range can be any sub-range between -5v to 5v, which enable the scanner to run between any specified degrees. A voltage protection scheme is also introduced in VNIR\_3.0. Any input voltage smaller than -5V or larger than +5v will be replaced with -5v or +5v respectively.

### A.3 Data Synchronisation, Transformation and Display

The VNIR\_3.0 is able to handle hyperspectral image cube with size as large as 696\*512\*1024 without crushing. In the meantime, a full 696\*1024 image can be displayed on screen.

The readout value of each frame is stored in a block memory Mem\_A with initial address pointed by *pic1->adr (CCambuf \*pic1)*, whose size is set as  $(1392*1024+1024*10)*2$  bytes by the function *pic1->Allocate(szie)*. As the CCD size of the VNIR camera is 1392\*1024 and the pixel depth is 12 bits, the size allocated to the memory is slightly larger than actual need. The data transferred out from the Mem\_A is determined by *lp->pic1->Add\_to\_list()* function as  $2*actwidth*actheight$ , where actwidth and actheight are the actual width and height of the  $x-\lambda$  image per frame.

The second important block of memory in PC is the memory Mem\_B with size of '2\*actwidth\*actheight\*frames' bytes for storing the hyperspectral image cub. Here, 'frames' is the number of frames used to build the image cube.

In order to display a 2D  $x-y$  image in slected wavelength, another block of memory Mem\_C with size of  $2*actwidth*frames$  bytes is required. It is this memory that will be the source of raw data transferred to the screen device

context. A pointer *listdatapreview/preview\_focus* stores the initial address of the Mem\_C.

The data is transferred freely from Mem\_A to Mem\_B or Mem\_C by using *memcpy* function provided by C++.

Bitmap data in the PC memory Mem\_D (stack), without being assigned initial values, is created in *WinMain* function by *pic1->Setbuffer* calling *pic1->SetBitmap* that returns the handle of the Bitmap *hbm*. Considering *BitBlt/StrechBlt* can transfer specific size of bitmap, the Mem\_D is fixed as *actwidth\*1024* bytes (image to be showed on screen will be of 8-bit depth) for holding *xy* bitmap image in selected wavelength built from 1-1024 frames. The initial address of Mem\_D is pointed by *CCamdisp.pic8*.

The raw data is converted from 12bits/pixel into 8bits/pixel and then copied from Mem\_C to Mem\_D by *conv\_buf\_12to8 (0, width, frames, (unsigned short\*)pic->adr,pic8,bwlu )* function in *CCamdisp.Convert*. The parameter *frames* in the *conv\_buf\_12to8* was *height* in VNIR\_1.0, which makes only 512-pixel height (Y=512) of image be able to be displayed on screen in vertical binning model. As there is no explanation of the usage of *conv\_buf\_12to8* from the manual provided by the company, the modification of the parameter from *height* to *frames* solely depends on analysis and trial and error. The codes below taken from source codes of VNIR\_3.0 are for displaying the raw data on screen.

*//hWnd is the handle of Main window, hbm is handel of bitmap. Before applying //BitBlt,hbm has to be selected into memory device context of the client window that is //created by CreateCompatibleDC.*

```
myhdc=GetDC(hWnd);
```

```
myhdcmem=CreateCompatibleDC(myhdc);
```

```
SelectObject(myhdcmem,hbm)
```

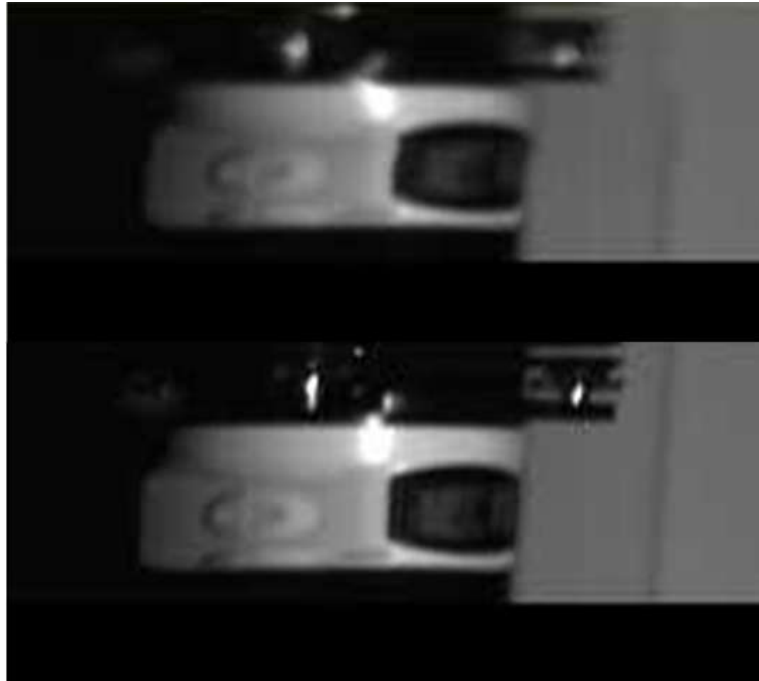
```
BitBlt(myhdc,0,0,width,lines,myhdcmem,0,0,SRCCOPY)
```

#### A.4 Optical Focusing

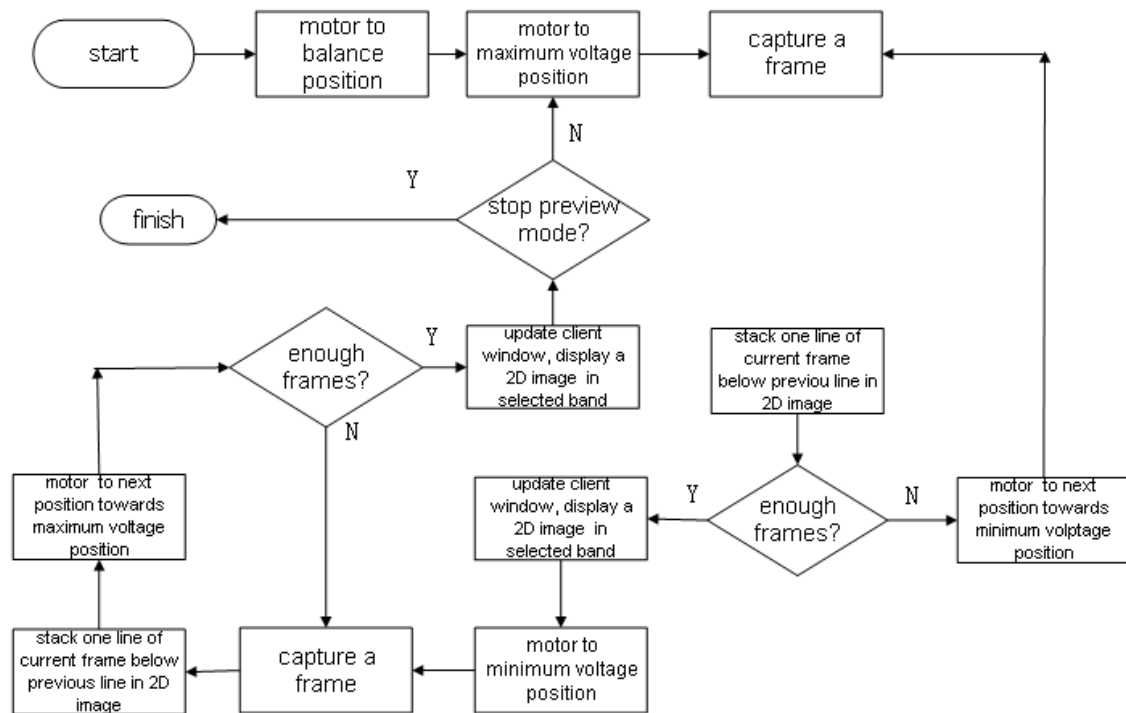
The VNIR camera cannot focus automatically. However, manual focus is tedious if every adjustment relies on the latest result of 2D spatial image. A preview mode for focus purpose is provided in VNIR\_3.0. Under this mode, motor rotates continuously from maximum voltage position to minimum voltage

position then back to maximum voltage position. The scanning angle of the motor in this mode is much smaller than that in the mode of building hyperspectral image cube, since only small object is required as a reference for focus. After the motor completes every full scanning angle, the client window for preview is updated, so that the original display on the window is shifted down and a new 2D spatial image in the selected wavelength can be displayed in the top of client window. The effect of every adjustment is obvious by comparing the top 2D image and the second top one. Figure\_Apx A-2 illustrates a client window in a focus session. The reference object in the client window is a small yellow laser machine. By comparing the latest image of the reference object, which is on the top of the client window, with the very original image of the reference, which is at the bottom of the client window, we know that the focus is becoming worse, since the very original image is much sharper and brighter than the latest one. In VNIR\_3.0, a thread function is written for implementing the preview. Flow chart of this thread function is given in Figure\_Apx A-3. Only a parameter passed to the thread from the main function can stop the preview mode, thus it will not be terminated until scanner reaches minimum voltage position and then back to zero voltage position. The codes for updating the client window and displaying latest 2D images are as following

```
lprect=&rect;
GetClientRect(myhwndmain, lprect);
//update client window, copy the whole client window to the place which is
'number+30' //pixels below to the top line of the client window, thus the new x-y
image can take the //place of 'number'-pixel height area. The 30 pixels will be
the //gap between each x-y //image.
BitBlt(lp->camdisp->myhdc,0,number+30,lprect->right,lprect->bottom,lp-
>camdisp-
>myhdc,0,0,SRCCOPY);
SelectObject(lp->camdisp->myhdcmem,lp->camdisp->hbmpp);
//copy latest x-y image to the top of the client window.
BitBlt(lp->camdisp->myhdc,0,0,lp->camdisp->width,number,lp->camdisp-
>myhdcmem,0,0,SRCCOPY);
```



**Figure\_Apx A-2 Images of a small yellow laser during focus session. By comparing image on the top with the image on the bottom, it is obvious that the focus is becoming worse.**



**Figure\_Apx A-3 Flow chart for implementing the thread for aiding**

## Appendix B List of Publications

1. **Tong Chen**, Peter Yuen, Kan Hong, "Wavelength Selection for Hypersectral Imaging Tissue Oxygen Saturation: for the remote sensing of human emotions", *IEEE Transaction on Affective Computing* (Submitted).
2. **Tong Chen**, PWT Yuen, K Hong, Ibrahim, A Tsitiridis, U Soori, J Jackman, D James, M, Richardson, "Assessment of tissue blood perfusion in-vitro using hyperspectral and thermal imaging techniques", *5<sup>th</sup> International Conference on Bioinformatics and Biomedical Engineering*, Wuhan, 2011.
3. **Tong Chen**, Peter Yuen, Kan Hong, Aristeidis Tsitiridis, Firmin Kam, James Jackman, David James, Mark Richardson, William Oxford, Jonathan Piper, Francis Thomas & Stafford Lightman, "Remote sensing of stress using Electro-optics imaging technique". *Proceedings of the SPIE*, 7486, pp. 0601-12, 2009.
4. Kan Hong, Peter Yuen, **Tong Chen**, Aristeidis Tsitiridis, Firmin Kam, Mark Richardson, David James, William Oxford, Jonathan Piper, Francis Thomas, Stafford Lightman, "Detection and classification of stress using thermal imaging technique", *Proceedings of the SPIE*, 7486, pp. 0101-09, 2009.
5. Aristeidis Tsitiridis, Peter Yuen, Kan Hong, **Tong Chen**, Firmin Kam, James Jackman, David James & Mark Richardson, "A biological cortex like target recognition and tracking in cluttered Background", *Proceedings of the SPIE*, 7486, pp. 0G01-0G12, 2009
6. Peter Yuen, Izzati Ibrahim, Kan Hong, **Tong Chen**, Aristeidis Tsitiridis, Firmin Kam, James Jackman, David James & Mark Richardson, "Classification Enhancements in Hyperspectral Remote Sensing Using Atmospheric Correction Preprocessing Technique", *The Technical Defence S&T Bulletin (Buletin Teknikal S&T Pertahanan)*, pp.91-99. 2009.
7. Peter Yuen, **Tong Chen**, Kan Hong, Aristeidis Tsitiridis, F Kam, James Jackman, David James, Mark Richardson, L Williams, William Oxford, Jonathan Piper, Francis Thomas & Stafford Lightman, "Remote detection of stress using

Hyperspectral imaging technique”, *proceeding of the 3rd International Conference on Crime Detection and Prevention ICDP-09*,2009

8. Peter Yuen, Kan Hong, **Tong Chen**, Aristeidis Tsitiridis, Firmin Kam, James Jackman, David James, Mark Richardson, L Williams, William Oxford, Jonathan Piper, Francis Thomas & Stafford Lightman, “Emotional & physical stress detection and classification using thermal imaging technique”, *proceeding of the 3<sup>rd</sup> International Conference on Crime Detection and Prevention ICDP-09*, 2009

9. Peter Yuen, Aristeidis Tsitiridis, Kan Hong, **Tong Chen**, Firmin Kam, James Jackman, David B. James & Mark A. Richardson, “A cortex like neuromorphic target recognition & tracking in cluttered background”, *Proceeding of the 3<sup>rd</sup> International Conference on Crime Detection and Prevention ICDP-09*, 2009

10. Aristeidis Tsitiridis, Peter Yuen, Kan Hong, **Tong Chen**, Izzati Ibrahim, James Jackman, David James and Mark Richardson, “An improved cortex-like neuromorphic system for target recognitions”, *Proceedings of SPIE 7838*, 78380Q, 2010

11. Izzati Ibrahim, Peter Yuen, Aristeidis Tsitiridis, Kan Hong, **Tong Chen**, James Jackman, David James and Mark Richardson, "Illumination independent object recognitions in hyperspectral imaging", *Proc. SPIE 7838*, 78380O, 2010.